



City Research Online

City, University of London Institutional Repository

Citation: Vidakovic, M. (2017). Optical Fibre Sensors applied to condition and structural monitoring for the marine and rail transport sectors. (Unpublished Doctoral thesis, City, University of London)

This is the accepted version of the paper.

This version of the publication may differ from the final published version.

Permanent repository link: <https://openaccess.city.ac.uk/id/eprint/19664/>

Link to published version:

Copyright: City Research Online aims to make research outputs of City, University of London available to a wider audience. Copyright and Moral Rights remain with the author(s) and/or copyright holders. URLs from City Research Online may be freely distributed and linked to.

Reuse: Copies of full items can be used for personal research or study, educational, or not-for-profit purposes without prior permission or charge. Provided that the authors, title and full bibliographic details are credited, a hyperlink and/or URL is given for the original metadata page and the content is not changed in any way.



Optical Fibre Sensors applied to condition and structural monitoring for the marine and rail transport sectors

Submitted by

Miodrag Vidakovic

Thesis submitted for the degree of Doctor of Philosophy

Supervised by

Professor Tong Sun

Professor Kenneth T.V. Grattan

City, University of London

School of Mathematics, Computer Science and Engineering

EC1V 0HB, London, UK

December 2017

Table of Contents

Table of Contents	i
List of Figures	iv
List of Tables	ix
Acknowledgements	x
Declaration	xi
Abstract	xii
Glossary of Symbols and Abbreviations	xiv
1 Introduction	
1.1 Introduction	1
1.2 Aims and Objectives	2
1.3 Structure of the thesis	3
1.4 Summary	5
2 Non-Destructive methods for structural health monitoring: an overview	
2.1 Introduction	6
2.2 Key parameters that determine the structural health condition	6
2.3 Conventional non-destructive (NDT) testing	7
2.3.1 Acoustic Emission Testing	7
2.3.1.1 Guided Wave Testing	10
2.3.1.2 Ultrasonic Testing	11
2.3.2 Imaging Techniques	13
2.3.2.1 Ultrasonic guided wave imaging	13
2.3.2.2 Ultrasonic infrared thermal wave imaging	14
2.3.2.3 Laser based imaging	15
2.3.2.4 Electromagnetic – thermal imaging	20
2.3.2.5 Visual inspection	21
2.3.2.6 Magnetic particle inspection	22
2.3.3 Liquid penetrant testing	22
2.3.4 Eddy Current testing	23
2.4 Optical fibre based non-destructive testing (NDT) methods	24
2.4.1 Introduction	24
2.4.2 Distributed optical fibre sensors	25

Table of Contents

2.4.2.1	Rayleigh backscattering systems	26
2.4.2.2	Raman Scattering	29
2.4.2.3	Brillouin Scattering	31
2.4.3	Optical fibre interferometers	32
2.5	Summary	35
3 Fibre Bragg Grating Based Sensors		
3.1	Introduction	36
3.2	Background	36
3.3	FBG inscription methods	38
3.4	Classification of Fibre Bragg grating sensors	44
3.5	Properties of Fibre Bragg Gratings	46
3.5.1	Reflectivity of a Uniform Fibre Bragg grating	46
3.5.2	Strain and Temperature sensitivities of FBGs	47
3.6	FBG multiplexing schemes	48
3.6.1	Time division multiplexing (TDM)	48
3.6.2	Wavelength division multiplexing (WDM)	49
3.6.3	Frequency division multiplexing (FDM)	50
3.6.4	Spatial division multiplexing (SDM)	53
3.7	Applications of FBG sensors as an important NDT technique	54
3.7.1	Strain and loading monitoring	54
3.7.2	Corrosion monitoring	58
3.7.3	Vibration and acceleration measurement	62
3.7.4	Acoustic wave measurement	65
3.8	Summary	69
4 FBG-based Cascaded Acoustic Sensors for Marine Structural Condition Monitoring		
4.1	Introduction	70
4.2	Principle of operation	71
4.2.1	Edge Filter Detection Method	71
4.2.2	Power Detection Method	72
4.3	Sensors manufacturing process	73
4.4	FBG-based acoustic sensor design and sensor characterization	75
4.5	Experimental results	77

Table of Contents

4.5.1 Glass plate tests	77
4.5.2 Metal plate tests for cavitation monitoring	80
4.6 Summary	83
5 Fibre Bragg Grating-based Acoustic Sensor Array for Improved Condition Monitoring of Marine Lifting Surfaces	
5.1 Introduction	84
5.2 Theoretical background of acoustic source localization	85
5.3 Experimental setup	86
5.4 Experimental results	89
5.4.1 Impact point in the middle of lifting surface	89
5.4.2 Impact point between sensors locations S_0 and S_1	92
5.5 Discussion of the results obtained	94
5.6 Conclusions	97
6 Fibre Bragg Grating-based sensors system for condition monitoring of electrified railway pantograph	
6.1 Introduction	98
6.2 Need and Techniques for remote pantograph monitoring	99
6.3 FBG-based pantograph condition monitoring system	103
6.4 Temperature compensated contact force measurement	104
6.5 Summary	108
7 Conclusions and future work	
7.1 Conclusions of the work carried out	109
7.2 Future work – potential wider applications of the technologies developed	111
7.3 References	113
List of Publications	127

List of Figures

- Figure 2.1 Most commonly analysed parameters of a typical acoustic emission waveform [9].
- Figure 2.2 Guided wave testing equipment with transducer array around large pipe and signal interrogation unit connected with cables [17].
- Figure 2.3 Asymmetric and Symmetric Lamb waves behaviour in solid media [20].
- Figure 2.4 Schematic diagram of electromagnetic acoustic transducer [25]
- Figure 2.5 Crack detection using sonic-IR imaging technique [42].
- Figure 2.6 Experimental photoacoustic imaging setup [50].
- Figure 2.7 Experimental setup of laser ultrasonic method [25].
- Figure 2.8 Typical holographic experimental setup [52].
- Figure 2.9 ESPI out of plane displacement measurement setup [52].
- Figure 2.10 Shearographic laboratory experimental setup [52].
- Figure 2.11 Experimental setup with the inductor controlled by moving equipment [57].
- Figure 2.12 Rayleigh scattering of a light pulse in an optical fibre a) local inhomogeneities present in the optical fibre b) interaction of the light with the inhomogeneities causing Rayleigh backscattering [82]
- Figure 2.13 The basic arrangement of an Optical Time Domain Reflectometer (OTDR) [78]
- Figure 2.14 ULTIMA Distributed Temperature Sensor developed by Silixa [104]
- Figure 2.15 Rayleigh, Brillouin and Raman scattering for distributed optical fibre sensing systems [105]
- Figure 2.16 Intrinsic optical fibre interferometers a) Mach-Zehnder; b) Faby-Perot; c) Michelson; d) Sagnac; and e) ring resonator [10].
- Figure 2.17 Schematic illustration of EPPI transducer [6].
- Figure 3.1 Illustration of a fibre Bragg grating [126].
- Figure 3.2 Schematic diagram of amplitude splitting interferometer reported by Meltz at al [129] demonstrating side written FBG.
- Figure 3.3 Schematic diagram of Lloyd interferometer [130].

List of figures

- Figure 3.4 Schematic of prism based wavefront splitting interferometer [130].
- Figure 3.5 Schematic illustration of phase mask technique for FBG manufacturing process [130].
- Figure 3.6 Schematic diagram of femtosecond-IR laser FBG writing technique [134].
- Figure 3.7 Experimental set-up for FBG fabrication using femtosecond 264 nm pulses [140].
- Figure 3.8 Functional modulus of the novel FBG manufacturing technique [142].
- Figure 3.9 Femtosecond FBG writing approach using point by point method [146].
- Figure 3.10 Schematic of TDM multiplexing [154]
- Figure 3.11 Architecture of FBG based strain system [155].
- Figure 3.12 Schematic diagram of combination of FSI and WDM [156].
- Figure 3.13 Schematic diagram of FMCW multiplexed FBG sensor array in parallel topology [157].
- Figure 3.14 IOFDR measurement setup for a quasi – distributed temperature measurement using FBG sensors [158].
- Figure 3.15 FBG sensors as part of FOSS [159].
- Figure 3.16 Schematic diagram of SDM scheme [160].
- Figure 3.17 Schematic illustration of a sensor protection system using CFRP material (a) FBG installation inside rod (b) CFRP tube with integrated FBGs [161].
- Figure 3.18 Schematic representation of the optical based strain transducer to be embedded into concrete [162].
- Figure 3.19 Fibre Bragg grating weldable strain sensor [163].
- Figure 3.20 Unloaded swept plate instrumented with 300 FBG sensors, where the sensor locations are represented by white circles [164].
- Figure 3.21 Schematic drawing of instrumented FRCM strengthened beam with embedded FBGs [165].
- Figure 3.22 Schematic representing geometry, loading scheme and sensor layout on both beams [166].

List of figures

- Figure 3.23 Schematic diagram of packaging procedure of concrete corrosion FBG sensor [169].
- Figure 3.24 Corrosion monitoring FBG sensors layout [169].
- Figure 3.25 Layout of FBG sensors embedded in steel plates [170].
- Figure 3.26 Schematic diagram of FBG hoop – strain sensor for corrosion detection on oil and gas pipes [171].
- Figure 3.27 FBG sensor protection using PDMS layer [172].
- Figure 3.28 Schematic structure of proposed accelerometer and instrumentation of the pipe for oil and gas industry [180].
- Figure 3.29 Schematic structure FBG accelerometer based on double diaphragms reported by Liu *et al* [181].
- Figure 3.30 Schematic structure of TCF-FBG accelerometer [178].
- Figure 3.31 Schematic illustration of the FBG sensors employed in the experiment [184].
- Figure 3.32 Ultrasonic responses of FBG sensors with different grating length [186].
- Figure 3.33 Schematic illustration of the excitation positions [189].
- Figure 3.34 Waveforms detected in three different AE experiments a) surface pencil-lead break, b) side pencil-lead break, and c) steel ball drop [189].
- Figure 4.1 Edge filter detection method using a SLD light source, coupled with a) linear edge filter, b) matched FBG, c) WDM coupler and d) demultiplexer [192].
- Figure 4.2 Power detection methods, a) broadband power detection, b) narrowband source with reflected component, c) narrowband source with transmitted component [192].
- Figure 4.3 Basic configuration of FBG manufacturing setup at City, University of London
- Figure 4.4 Phase mask setup for FBG manufacturing process at City, University of London
- Figure 4.5 The experimental setup: the FBG-based cascaded acoustic sensor system, with a co-located PZT acoustic sensor for cross-comparison
- Figure 4.6 The spectrum of the C-Band light source used for this experiment
- Figure 4.7 Spectral slope of the optical filter used in combination with FBG₁ optical sensor
- Figure 4.8 Time waveforms detected by both FBG₁ and PZT based acoustic sensor when

List of figures

- glass plate was excited using a steel ball
- Figure 4.9 Cross – comparison of waveforms detected by both the PZT and multi-point FBGs
- Figure 4.10 Schematic of the setup for the acoustic tests of the steel plate instrumented with both FBG and PZT acoustic sensors
- Figure 4.11 Steel plate instrumented with PZT and FBG acoustic sensors (placed underneath) showing the cavitation erosion occurred in the middle of the plate
- Figure 4.12 Acoustic signals acquired by the co-located FBG-based and PZT acoustic sensors when the metal plate is subject to the excitation of the sonotrode at a frequency of 19.5 kHz
- Figure 4.13 Frequency response of a FBG-based acoustic sensor and a PZT acoustic sensor illustrating the close match (in this case with a standard sonotrode frequency of 19.5 kHz)
- Figure 5.1 Emission signals from Source P can be detected by an arbitrary 3-sensor array at different locations with different arrival times
- Figure 5.2 Design of the marine lifting surface under investigation with a) upper surface where sensors are to be installed, b) inner surface with the shaft
- Figure 5.3 Overall distribution of positions (dark dots) where the impact was applied during the tests. FBG-based acoustic sensors and PZT sensors locations are marked S0, S1, S2 and S3
- Figure 5.4 Cavitation tests of the half-rudder instrumented with both FBG and PZT acoustic sensors
- Figure 5.5 Acoustic signals acquired by both FBG-based acoustic sensor and co-located conventional PZT sensor indicating similar time of arrival (excitation point 10 (16cm, 7cm))
- Figure 5.6 Acoustic signals acquired by the optical based acoustic sensors at all four sensor locations of the half-rudder when rudder was subject to excitation of the sonotrode at Point 10
- Figure 5.7 Frequency response of FBG-based acoustic sensors and PZT acoustic sensors indicating a close match of standard sonotrode frequency of 26 kHz when excited at Point 10
- Figure 5.8 Acoustic signals acquired by both FBG-based acoustic sensor and co-located conventional PZT sensor indicating similar time of arrival (excitation point 9 (16cm, 0cm))
- Figure 5.9 Acoustic signals acquired by the optical based acoustic sensors at all four sensor locations of the marine lifting surface when it was subject to excitation of the sonotrode at Point 9

List of figures

- Figure 5.10 Frequency response of FBG-based acoustic sensors and co-located PZT acoustic sensors indicating capture of standard sonotrode frequency when excited at Point 9
- Figure 5.11 Calculated acoustic emission source locations based on the data from both FBG-based acoustic sensor (represented by ‘x’) and PZT based acoustic sensor (represented by ‘x’)
- Figure 6.1 Pantograph designed and manufactured at Brecknell Willis
- Figure 6.2 FBG sensor positioning and instrumentation methods [207].
- Figure 6.3 FBG force sensor with additional FBG for temperature compensation [209].
- Figure 6.4 Demonstration of an FBG array used for pantograph instrumentation and interrogation setup
- Figure 6.5 Pantograph connected to DC current supply with current change from 0 to 1500A and then from 1550A to 0A, when contact force is zero
- Figure 6.6 Temperature change recorded by the central thermocouple and current value applied to the pantograph during the experimental tests
- Figure 6.7 Wavelength shifts recorded from FBGs 4, 5 and 6 in the central package recorded during the experimental tests
- Figure 6.8 Contact force measured by FBG packages before and after temperature compensation algorithm
- Figure 6.9 Test train trials in collaboration with the Rail Alliance
- Figure 6.10 Contact force measured by developed FBG-sensor system while train was moving
- Figure 6.11 Contact location measured while train is running

List of Tables

Table 2.1	The most commonly monitored parameters [6]
Table 3.1	Comparison between PZT and FBG ultrasonic sensors [178].
Table 5.1	Cross Comparison between FBG and PZT Detected Source Coordinates (x, y)
Table 5.2	Deviations measured using both FBG-based and PZT-based sensors (x, y)

Acknowledgements

First and foremost I would like to express my sincerest gratitude to my supervisors, Professor Tong Sun and Professor Kenneth Grattan for their knowledge, invaluable guidance, encouragement and support throughout this work. There is no words that could express my appreciation to both of them. I have been fortunate to have such great people to be my supervisors at the same time.

I wish to thank Professor Sanowar Khan, Professor Zeljen Trpovski and Professor Vojin Senk for their encouragement to pursue postgraduate studies abroad.

Special thanks is given to my fellow research colleagues; in particular, Dr Fei Xiong for her patience and guidance at the very early stage of my Ph.D studies; Dr Colum McCague for all his support during initial experimental work and always great conversations; Dr Matthias Fabian for sharing his experiences, enormous technical support and more importantly for being a great friend. I would also like to thank Matthias for all cheerful chat, and great laughs that we had together over after work beverages. I wish to extend my gratitude to Dr Ye Chen and Dr Martin Ams for all their suggestions and ideas.

I would also like to express my gratitude to my cousins Milica and Jelena who supported my initial application to study abroad and helped me to complete all necessary documents to make it happen. In addition to it, I would like to say thank you to my first tutor and a great friend, Jovan Ilic, who guided me through high school journey and encouraged me to play basketball. Thanks to him I have realised the importance of being involved in sport for the career development and development of strong personality. In addition to it, I would like to say thank you to Ivana, Miro, Ivona, Hayley and the other City and basketball friends for all the support.

Finally, I would like to extend my warmest gratitude to my family. I would like to start with my uncle Nenad who was always supportive. Special thanks go to my parents and my brother for their support throughout every part of my life. They have been a constant source of incalculable support and encouragement and for that I can't thank them enough.

Declaration

Declaration

This thesis is written to meet the requirements for the degree of Doctorate of Philosophy. It is entirely my own work and has not been submitted to any other university or higher institution. Where the work of other people has been used, it has been fully referenced and acknowledged.

Signed:

Miodrag Vidakovic

Abstract

This thesis reports the development of a suite of FBG-based optical fibre sensors for non-destructive testing (NDT) and illustrating their potential for several specific industrial applications in the marine and railway sectors. These arose from work driven by the needs of project collaborators from these industries and are intended to be illustrative of the wider potential applications that optical fibre sensors have for measurements in different industrial sectors. The research has involved the development of new sensor system designs to meet these needs, building as they do upon a comprehensive review of NDT technologies and solutions, discussed in some detail.

In this research for the marine sector, a single FBG-based acoustic sensor was specifically developed and evaluated and compared with the performance of conventional sensors. To do so, a metal plate to which the sensors were fixed was excited with a sonotrode, at a resonant frequency of 19.5 kHz. The signal reflecting that acoustic excitation was captured by the FBG sensors designed and implemented and their performance has been shown to be comparable with that from conventional, industry-standard piezoelectric transducers (PZTs). Preliminary work undertaken for the sponsors then lead to the further development of an acoustic sensor array comprising of 3 FBGs, which was subsequently validated against co-located PZTs which all were installed on a glass plate and excited in an industry-standard way, through the acoustic signal from a 0.2 g steel ball dropped onto the plate. When signals were analysed and compared, the positive comparative performance outcomes from the sensors used enabled further the design and implementation of instrumentation for a marine lifting surface using a different array, designed comprising 4 FBG-based acoustic sensors. Extensive tests on the smart marine lifting surface created were undertaken under water with a sonotrode set at 26 kHz as an excitation source. Based on the arrival time of acoustic signals captured by each grating and the use of triangulation method, the location of the excitation source could thus be determined, to meet the needs of the industrial sponsor and show good agreement with the outputs of conventional sensor systems.

In parallel with the above, a further new industrial application of FBG-based sensor arrays was developed for a major player in the field, for the first time successfully instrumenting a railway current-collecting pantograph to allow reliable, remote *in situ* monitoring of key parameters: the contact force and contact location of the pantograph against the catenary. The optical fibre sensor approach has been shown to be an excellent means of measurement whose performance

Abstract

can be extrapolated to situations where the train is driven at high speeds up to 125 mph and powered from a high voltage line at 25 kV, in this design taking full advantages of the immunity of the optical fibre sensors to electromagnetic interference. In this research, key technical performance challenges were addressed and successfully overcome, including the temperature compensation needed for ‘all-weather’ performance, due to the intrinsic cross-sensitivity problems of using a FBG-based design being fully addressed. This ensures the accurate measurement of the contact force/location between the pantograph and the catenary under all weathers.

The research concludes by considering future directions for the work in these and other industry sectors.

Glossary of symbols and abbreviations

AE	Acoustic Emission
AOM	Acousto-optic Modulator
AWG	Arrayed Waveguide Grating
BNS	Broadband Noise Source
BFS	Brillouin Frequency Shift
CCM	Concrete Corrosion Monitoring
CDM	Coherence Domain Multiplexing
CFRP	Carbon Fibre Reinforced Polymer
CZC	Current Zero Crossing
CW	Continuous Wave
dB	Decibel
DAS	Distributed Acoustic Sensing
DOFS	Distributed Optical Fibre Sensors
DTS	Distributed Temperature Sensing
DWDM	Dense Wavelength Division Multiplexing
GODC	Germanium Oxygen Deficient Centres
EM-T	Electromagnetic Thermal
EM-A	Electromagnetic Acoustic
EMAT	Electromagnetic Acoustic Transduced
EMI	Electromagnetic Interference
EPPI	Extinsic Fabry – Perot Interferometer
ESPI	Electronic Speckle Pattern Interferometry
FE	Finite Element
FBG	Fibre Bragg Grating

Glossary of symbols and abbreviations

FDM	Frequency Division Multiplexing
FFT	Fast Fourier Transform
FMCW	Frequency Modulated Continuous Wave
FOSS	Fiber Optic Sensing System
FP	Fabry-Perot
FPI	Fabry Perot Interferometer
FPR	Fibre Reinforced Polymers
FRCM	Fibre Reinforced Cementitious Matrix
FSI	Frequency Shifted Interferometry
FWHM	Full Width Half Maximum
HVOF	High Velocity Oxygen Fuel
IFFT	Inverse Fourier Transform
IOFDR	Incoherent Optical Frequency Domain Reflectometry
IR	Infrared
LED	Light Emitting Diode
LPG	Long Period grating
LUS	Laser Ultrasonics
MI	Michelson Interferometer
MMF	Multimode Fibre
MZM	Mach - Zehnder Modulator
MZI	Mach - Zehnder Interferometer
NA	Numerical Aperture
NASA	National Aeronautics and Space Administration
NDE	Non-Destructive Evaluation
NDT	Non-Destructive Testing
NIR	Near-Infrared

Glossary of symbols and abbreviations

OA	Optoacoustic
OFS	Optical Fibre Sensors
OLE	Overhead Line Equipment
OSA	Optical Spectrum analyser
OTDR	Optical Time Domain Reflectometry
OFDR	Optical Frequency Domain Reflectometry
PA	Photoacoustic
PBO	Polyparaphenylene Benzobisoxazole
PCF	Photonic Crystal Fibre
PDMS	Polydimethyl Siloxane
PDS	Photothermal Beam Deflection
PEC	Pulsed Eddy Current
PMF	Polarisation Maintaining Fibre
POTDR	Polarisation-Optical Time Domain Reflectometry
PM	Phase Modulator
PT	Photothermal
PTR	Photothermal Radiometry
SDM	Spatial Division Multiplexing
SG	Strain Gauge
SHM	Structural Health Monitoring
SI	Sagnac Interferometer
SLD	Superluminescent Diode
SMF	Single Mode Fibre
SRS	Stimulated Raman Scattering
SAW	Surface Acoustic Waves
TCF	Thin Core Fibre

Glossary of symbols and abbreviations

TEC	Thermoelectric Coolers
TDM	Time Division Multiplexing
TOF	Tunable Optical Filter
UV	Ultraviolet
VCO	Voltage Controller Oscillator
VNA	Vector Network Analyser
WDM	Wavelength Division Multiplexing
Φ -OTDR	Phase sensitive Optical Time Domain Reflectometry
Ge ²⁺	Germanium Dichloride
Λ	Grating Period
Ge/B	Germanium/Boron
H ₂	Hydrogen
Ge	Germanium
mol%	Molar Fraction
μm	Micro – metre
cm	Centi – metre
mm	Milli – metre
nm	Nano – metre
KrF	Krypton Fluoride
fs	Femtosecond
kHz	Kilohertz
MHz	Megahertz
Hz	Hertz
λ_B	Bragg Wavelength
n_{eff}	Effective Refractive Index
n_0	Average Refractive Index of Fibre Core
Δn	Amplitude of Induced Refractive Index Change
$R(l, \lambda)$	Reflectivity of Bragg Grating

Glossary of symbols and abbreviations

l	Grating Length
n	Refractive Index
n_{co}	Core Refractive Index
n_{cl}	Cladding Refractive Index
a	Fibre Radius
Δ	Variation of Particular Parameter
R_i	Reflection of i^{th} grating
L	Path Difference
k	Wavenumber
Ar^+	Argon
Ti	Titanium
mV	Milivolt
$\mu\epsilon$	Micro Strain
s	Seconds
ms	Milli-seconds
c	Speed of Light

Chapter 1

Introduction

1.1 Introduction

Industry faces on-going challenges to make new and better measurements and regularly looks to innovative or enhanced technologies to solve such measurement problems. Non-destructive testing (NDT) methods are particularly important as they, by definition, do not damage the workpiece or system on which they are used. They have been applied (in the form in which we understand the term today) for the first time to important industrial applications with the major industrial expansion seen from the second half of the 19th century, thereby showing the advantages of measurements that are non-invasive. Since that time work has continued and a considerable amount of effort has been expended on the development of new NDT technologies [1].

Acoustic emission detection represents one such and highly important NDT technology. In its ‘unscientific’ form we use it regularly when we diagnose a fault with an appliance or vehicle from an unusual sound that it makes. It was first understood by pottery makers who were able to identify cracks in the clay pots when cooled quickly, by listening to the sound they generate and acoustic emission has continued to be used to identify structurally defective pots. In the railway industry ‘wheel tapping’ to determine a fault in a locomotive wheel caused by a change in the note emitted when struck by a hammer has been used since the dawn of the industry. It was however not until 1950 that systematic research on AE-based NDT methods was undertaken by Josef Kaiser (and reported in his Ph.D thesis), becoming known as ‘Kaiser-Effect’ [2]. Since then, rapid developments in the field have been seen: pounding concrete surfaces with a hammer or a simple piece of metal and listening to the acoustic emission and critically its differences in response under different circumstances has now been replaced by ultrasonic sensors which take the frequencies used beyond the audible, coupling the outputs to advanced imaging techniques, as well as more recently, optical fibre based techniques [3].

In parallel with the above there has been a rapid development of optical fibre sensors, benefitting from the success of the optical telecommunications industry, due to their unique

advantages over their electrical counterparts. They are small, light-weight and immune to electromagnetic interference (EMI) and in essence inert to chemical contamination. Fibre Bragg grating (FBGs)-based sensors can be configured either as a point or (quasi-) distributed sensors, using various multiplexing schemes [3]. This has provided a sound basis for them being widely explored and exploited in various large scale structural condition monitoring applications. Research has also been undertaken to develop FBG-based sensors for monitoring acoustic emissions using various techniques and this research builds on that.

The focus of this research has been to address two major sensor challenges, identified by different industries and tackled using advanced optical fibre sensor techniques. The first of these came from the marine industry where for many years cavitation-based erosion has posed a key technical challenge through the degradation of performance of a variety of marine structures [4]. A series of phenomena is considered to be the cause of the complex nature of cavitation erosion, which does cause multi-million dollar damage to marine structures across the world and reduces vessel fuel efficiency. Effects such as bubble collapse and rebound, micro-jet formation and clouds of collapsing micro bubbles and cavitation vortices can cause the build-up of erosion mechanisms [4]. Therefore, there is a clear need in order to understand this better (and thus prevent it for the future) for cavitation signature monitoring and the better localisation of its source. The second, different but equally important key challenge identified by industry and tackled in this work has arisen in the railway industry where currently there is no commercially available product which is available to monitor the condition of the high speed railway pantographs and control their movement. Challenges arise in the design and implementation of such systems due to the high voltage working condition (25 kV), to avoid extreme train operation scenarios, such as are caused by loss of power due to dewirement, to occur. Train operators face penalties which can run to hundreds of thousands of pounds daily from delays due to such effects.

1.2 Aims and Objectives

In light of the discussions above and the context of the problems introduced by the two industries, the main aim of the work in this thesis has been the design, development and evaluation of a series of FBG-based optical fibre sensors to address specifically the challenges brought to the author's attention from the marine and railway sectors. These challenges are timely and of major financial consequence to the operators of the infrastructure involved, emphasizing the urgency to develop new solutions. To address these, a programme of work

was undertaken responding to the timescales presented and thus the measurable objectives of this thesis are summarized as follows:

- To conduct a comprehensive literature review of the existing NDT technologies, including using optical fibre sensor techniques that have been widely reported by a number of researchers worldwide
- To conduct a comprehensive review of fibre Bragg grating-based sensors and their applications
- Informed by the outcomes of the above, to use innovative methods in the design, characterization and evaluation of FBG-based acoustic sensor systems which can be tailored to be suitable for the demands of the marine environment and thus suitable for the applications above
- The FBG-based acoustic sensor system was developed to be suitable for acoustic emission measurement on a marine lifting surface called ‘half-rudder’ in order to detect signatures of cavitation phenomena which could lead to severe damages of these surfaces
- Again building on the outcomes of the literature review, to address the problem of a better, instrumented, railway pantograph through the design, development and evaluation of a FBG-sensor based system which is able to measure contact force/location of a railway pantograph against the overhead wire under all weathers
- To report the results to the industrial sponsors in a timely and professional way
- Following identification of new Intellectual Property and agreement on its use, to report the outcomes in both peer reviewed literature and at the international conferences

1.3 Structure of the thesis

This thesis is structured such that it comprises seven chapters describing the work carried out in order to achieve the aims and objectives discussed in the section above.

Chapter 1 begins with a brief introduction, highlighting the importance of non-destructive testing (NDT) and one of the key NDT technologies that has been widely explored: acoustic emission detection. This is followed by the introduction to Fibre Bragg Grating-based sensing techniques and their advantages over its electrical counterparts for the broad range of structural health monitoring (SHM) applications. This research has been focused on addressing two specifically identified industrial challenges from contacts in UK industry, with the aims and

objectives of the specific studies and this of the thesis overall being highlighted. This is followed by this outline of the structure of the thesis.

Chapter 2 focuses on a comprehensive review of existing sensing technologies that have been widely reported and used for non-destructive testing of a variety of concrete/metallic structures. Non-optical fibre techniques considered include acoustic emission techniques (ultrasonic testing and guided wave testing), imaging techniques (acoustic, thermal, laser and magnetic imaging techniques), liquid penetrant testing and Eddy current methods. They are explained in detail, coupled with corresponding and illustrative applications. Optical fibre sensors techniques include Fibre Bragg Grating-based technique which are detailed in Chapter 3, including distributed optical fibre techniques (Rayleigh backscattering, Raman scattering and Brillouin scattering techniques) and optical fibre interferometers (Mach-Zehnder, Fabry-Parot, Michelson, Sagnac and ring resonator) which are outlined with their respective applications to inform the design of sensor systems used in this work.

Chapter 3 provides a comprehensive review of the fibre Bragg grating sensing technology, including their fundamental sensing principle, their fabrication techniques and multiplexing schemes that have been reported. This is followed by a summary of their wide SHM applications via measurement of strain/loading, corrosion, vibration and acoustic waves leading to a consideration of how specific of these techniques can be adapted for this work.

Chapter 4 starts with the discussion of the basic principle of FBG sensors for dynamic acoustic pressure measurement as well as an experimental investigation of the FBG sensor system developed at City, University of London. Two different experimental arrangements were evaluated respectively using glass and metal plates to consider their differences. The research undertaken has shown that the performance of FBG-based sensor system evaluated was in good agreement with that of the industry-standard PZT-based sensors for acoustic monitoring, giving confidence in the use of the technique. The positive results obtained have led to further extensive tests on a marine lifting surface (rudder) using a similar but enhanced sensor layout.

Chapter 5 reports research carried out on a multipoint measurement system using an array of FBGs-based acoustic sensors. Based on the acoustic signals received by both the optical and their collocated PZT sensors, the aim was that the acoustic source location could thus be determined using the triangulation method with the measurement error determined to be within the sub-centimetre range.

Chapter 6 reports the work done on the second industry-driven project and demonstrates a novel sensor system design through integration of FBG sensor packages into a railway current collector for its remote condition monitoring which is becoming critical for the train operation at high speeds and under all weathers. The focus of the work has been on force measurement, corrected for extraneous effects (such as temperature) both due to the cross-sensitivity of a FBG and the wide operating temperatures.

Chapter 7 concludes the work carried out with the results obtained from this research, summarizing the main achievements made in relation to the aims and objectives given in Chapter 1. Future work is also included, based on the knowledge gained and limitations shown during the course of the research.

A list of reference to the topical literature is included at the end, as is a list of the publications by the author arising from this work.

1.4 Summary

In this chapter, a brief introduction and motivation of the work in this thesis has been made, followed by aims and objectives proposed and outlining the structure of the thesis.

Chapter 2

Non-destructive methods for structural health monitoring: an overview

2.1 Introduction

Since the very first approach of non-destructive testing (NDT) was applied in industry at the end of 19th century, a considerable amount of effort has been expended on the development of NDT techniques for a wide range of applications [1]; benefitting from their key advantages over traditional methods that require sampling from the structure under test – and of course which is destructive or damaging to a greater or lesser extent. NDT methods in the 21st century have become more sophisticated since the days of pounding concrete surfaces with a hammer or simply tapping a piece of metal and listening to the audible differences in the response between a flawed and a satisfactory workpiece. The development and evolution of different methods throughout the years has gone from the simple rebound hammer to more sophisticated methods such as ultrasonics and optical fibre based techniques, as well as advanced imaging approaches [3].

With the rapid development and inevitable aging of infrastructure, it is important to monitor its structural health, thus to ensure its integrity by detecting the onset of damage, for example fatigue cracks and corrosion in various critical structures, such as marine structures, off-shore oil and gas production facilities, rails and aircraft. This chapter reviews the major development of NDT technologies, including both sensing principles and their typical applications, with a main focus on the development of optical fibre based NDT methods and their applications in various industries to identify the key ‘gaps’ in the field which are addressed in subsequent chapters.

2.2 Key parameters that determine the structural health condition

With the wide developments and key technological advances in the last century, extensive infrastructure has formed the backbone of a modern society and has made a significant societal,

ecological, economic and environmental impact. Therefore, it is important to provide an optimum design and quality of its construction, ensuring that it is durable and safe for use by both specialists and the public-at-large. However, during its whole lifetime, a structure can be subjected to many different changes, both internally and externally, such as environmental degradation, the effects of poor design, overloading and possible unexpected events like earthquakes or impacts, as well as the usual 'wear-and-tear'. These structural deterioration factors determine eventually the effective working life of a typical structure [5].

Given the variety of structures available, the associated Structural Health Monitoring (SHM) with each can be performed using different modes: i.e. in the short term (typically up to few days), medium term (from few days to few weeks), long term (up to few years) or indeed some structures can be monitored over their whole lifespan. In order to identify the most appropriate parameters to be measured for a particular structure, the type and the purpose of a structure, expected loads, construction materials, environmental conditions and expected degradation phenomena are critical to be considered. In general terms, these parameters can be classified into three main categories, classified as *chemical*, *mechanical* and *physical*. The most frequently monitored parameters are given in Table 2.1.

Table 2.1. The most commonly monitored parameters [6] for structures

Parameter Type	Key Parameters
<i>Chemical</i>	<i>Chloride penetration, sulphate penetration, pH value, carbonation, oxidation of rebars/steel</i>
<i>Mechanical</i>	<i>Strain, deformation, displacement, cracks opening, stress, load</i>
<i>Physical</i>	<i>Temperature, humidity, pore pressure (for concrete)</i>

2.3 Conventional non-destructive testing (NDT) methods

In this subsection a general review of the major development of conventional non-destructive methods to date is provided, explaining the principles behind the major NDT methods, the main parameters being measured and the applications where the techniques are widely used.

2.3.1 Acoustic Emission Testing

Acoustic emission (AE) testing methods are based on the fact that solid materials emit either sonic or ultrasonic waves when they are mechanically or thermally excited, to the point where

deformation or a fracture occurs. Acoustic emission is defined as the propagation of elastic waves due to the release of localised internal energy, such as micro-fractures in elastic materials [7]. The most common sources of AE events include those following a structural deformation process, such as plastic deformation, crack expansion and other kinds of material degradation [8].

In order to analyse the AE signals detected, it is necessary to create a better understanding of the parameters that need to be considered and the type of the information that they carry. The most common AE parameters (and how they are measured) are illustrated in Fig. 2.1 – this approach is so-called parametric analysis.

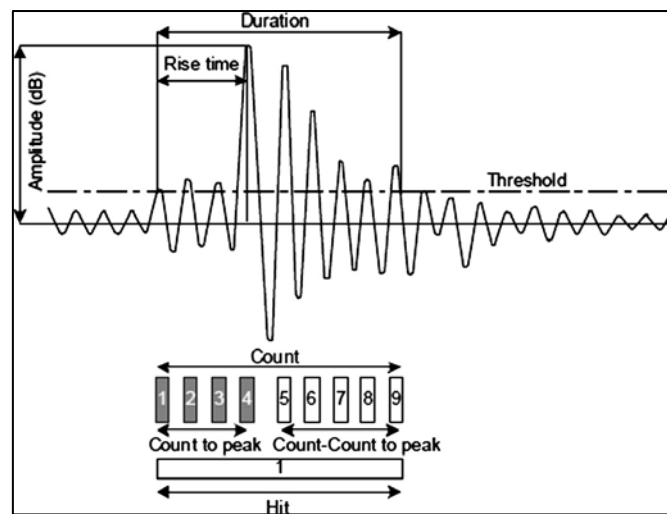


Figure 2.1 Most commonly analysed parameters of a typical acoustic emission waveform [9]

These signal characteristic parameters are used to evaluate the grade of a particular damage and identify the nature of damage. The signal *rise time* defines the time from the first threshold crossing to the maximum amplitude of the acoustic emission; in other words, it refers to the time interval from the generation of the AE to its maximum amplitude. The rise time is related to the propagation of the wave between the source of acoustic emission and the sensor and is used for the qualification of acoustic emission signals [9]. *Amplitude* is defined as the greatest measured value in a waveform and is typically measured in decibels (dB). It is a very important parameter as it directly determines the detectability of the signal and indicates the intensity of the source. For example in concrete structures, it is directly related to the scale of the structural damage [9]. The *duration* of the acoustic signal provides the information about the energy of the emission source and is defined as the time difference between the first and last threshold crossings. The triggering value of the AE system to record the waves is called the *threshold*, which influences the measurement of the rise time and the duration of the AE signal.

The most common situations that generate AE events are given below [10]:

- *Materials degradation* such as defect growth, cracks, plastic deformation, various fractures, corrosion and disbanding coatings.
- *Reversible processes* such as crystallographic phase transformations, melting or solidification, thermoelastic effects, friction between surfaces, etc.
- *Fabrication processes* such as welding noise, rolling, machining, drilling, mixing, grinding, etc.
- *Leaks and flows*: single or two phase fluids flows, particle flow, leaks, gas evolution, boiling, etc.

Elastic waves can also be generated by actuators. This is the case in ultrasonic based non-destructive testing where typically piezoelectric transducers are used for the generation of signals.

In order to provide a successful measurement framework using AE sensors it is necessary to select appropriate AE sensors that suit the specific application(s). Considering the working principle where AE sensors convert the mechanical energy carried by the elastic wave into an electrical signal, the sensor is more precisely termed a transducer – that is a device which operates through an energy conversion process. The most widely used transducers are piezoelectric in nature and there are two main types used for AE testing, i.e. *resonance sensors* and *broadband sensors*, depending on the application [11].

Resonance sensors are designed to ensure the most efficient energy conversion from electrical to mechanical when the piezoelectric ceramic material changes dimensions cyclically, at the resonance frequency of an AC electric field. These resonant sensors are sensitive to a small range of frequencies, near the resonance frequency. This type of sensor is used for the detection of velocity or acceleration, due to their high sensitivity to the surface motions. Low resonance sensors with the resonant frequency less than 60 kHz can be used for concrete structural condition monitoring because high frequency components are quickly attenuated by inhomogeneity of concrete structures. The most appropriate resonant frequency for metals is around 300 kHz and for fibre reinforced polymers (FRP) 150 kHz [12].

Broadband piezoelectric sensors can record the range of frequency components of the wave with the same sensitivity. Therefore, they are widely used for the detection of response to displacement, when the surface motion is required to be characterised. Compared to the resonance sensors, these sensors typically are of lower sensitivity [11].

Regarding the acoustic emission techniques, the two most commonly used methods are based on guided wave testing and ultrasonic testing. These two methods and their applications are explained in more detail in this subsection.

2.3.1.1 Guided Wave Testing

Guided wave testing has recently attracted various industrial applications and has been used mainly for monitoring of the pipes, pipelines and rails [13]. Guided waves propagate in two possible modes, symmetric (S_n) and antisymmetric (A_n) and they propagate by interaction with the boundaries of the structure [14-16]. Guided ultrasonic waves (GUWs) have the ability to travel relatively long distances, which is why the technique is most commonly used for the inspection of long structures.

A typical illustration is where the transducer is used on one location of the pipe, where it excites the pipe by transmitting the waves along it. When defects (or indeed any other geometric change) are present on the surface, part of the energy of the wave is reflected. The reflected waves are detected by the transducer device and the time of arrival is measured and used for the distance calculation of the defect. The transducer is usually in the form of an array, enabling it to be used to determine the circumferential location of the defect. A typical experimental setup is shown in the Fig. 2.2.

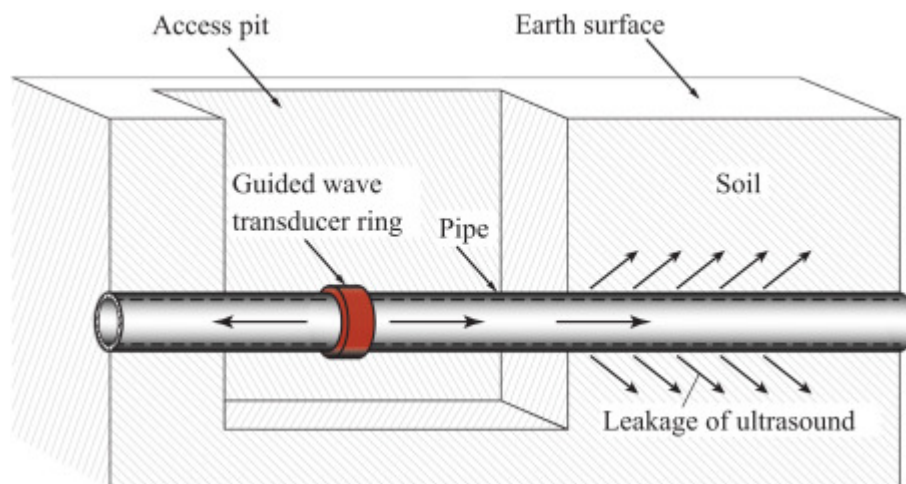


Figure 2.2 Guided wave testing equipment with transducer array around large pipe and signal interrogation unit connected with cables [17].

It has also been reported that two or more parallel arrays could be instrumented on the pipeline in order to provide the information needed in many cases about the direction of propagation and thus inspections can be made upstream *or* downstream from the transducer [13].

Most experiments conducted using this approach have investigated idealised discontinuities which have been successfully detected using this method. The results have shown that the

amplitude of the reflected signal is proportional to the reduction of the cross-sectional area at the location of the discontinuity; therefore the signal amplitude received indicates the severity of the damage. The technique can also be used for corrosion detection, when a flexural wave, which deforms the structure transversely when it propagates, can be detected and used to distinguish the presence of the discontinuity [18].

Often underwater measurements are needed and there a similar approach could be applied, with the technique being based on the inspection of Lamb waves. Lamb waves are defined as elastic perturbations that most commonly occur in solids that have free boundaries where the perturbations are a result of the combination of displacement in both the direction of wave propagation and perpendicular to the plane of plate [19]. The speed of the Lamb waves depends not only on the material properties but on the excitation frequency, and they can appear in two modes, symmetric and asymmetric, as illustrated in the Fig. 2.3 [20].

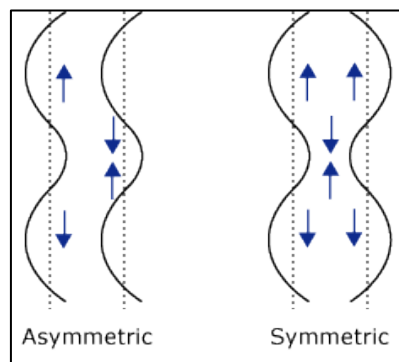


Figure 2.3 Asymmetric and Symmetric Lamb waves behaviour in solid media [20]

Billy *et al* [21] proposed two inspection schemes used for immersed structures in water. One uses the transducer in the pulse-echo mode, where the transducer is both sending and receiving the sound. Another scheme uses the transducer positioned at the opposite side of the plate and the backward transmitted ultrasonic signals were recorded. Lamb waves have also been successfully used for monitoring of rough surfaces [22].

2.3.1.2 Ultrasonic Testing

Ultrasonic testing (UT) is a non-destructive technique based on the detection of propagating ultrasonic waves in the object or material under examinations. The most common ultrasonic applications are based on very short ultrasonic pulse-waves with central frequencies ranging from 0.1 to 50 MHz. These short pulses are transmitted into materials with the main purpose of detecting internal flaws or characterising a particular material. This technique is often performed on steel and other metals, but it can also be used on concrete, wood and composites.

Around the middle-late part of the last century, as new ultrasonic testing method, electromagnetic-acoustic (EM-A) techniques have emerged and were effectively applied to non-destructive testing [23]. EM-A mainly refers to the electromagnetic acoustic transducers (EMATs) technique where they have used non-contact ultrasonic transmitting and receiving devices for non-destructive inspection and material characterization. They generate and detect ultrasonic waves via electromagnetic coupling between the transducers and the samples under test [24]. A schematic diagram of a typical EMAT system is shown in Fig. 2.4, consisting as it does of a magnet, coil and a specimen with the coil and magnet usually being regarded as the EMAT probe.

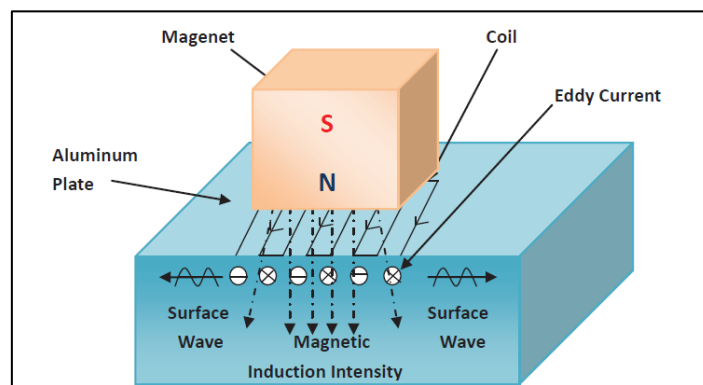


Figure 2.4 Schematic diagram of electromagnetic acoustic transducer [25].

The advantage of using this technique is that various different ultrasound waves can be used in this approach, including surface waves, plane waves and bulk waves, etc. [26]. Finkel and Godinez have demonstrated the abilities of the EM induced defect stimulation to detect small cracks in thin-walled aluminium structures [27]. A method reported in that paper is based on the electromagnetic modulation of the ultrasonic signal and the method has shown the increased detection ability of small fatigue cracks.

EMATs based sensors have also been successfully implemented in railway structure monitoring. It has been reported that they have been used for a rail flow detection application in which EMATs were used to generate a surface wave at the frequency of MHz range [28]. In subsequent work, a different research group has developed a rail flow detection system based on multi-channel electromagnetic acoustic transducers [29].

2.3.2 Imaging techniques

In this subsection, the main focus is on reviewing the basic principles of imaging techniques used in NDT and their main applications. Six different methods are discussed, with for each a number of different approaches often taken.

2.3.2.1 Ultrasonic guided wave imaging

Ultrasonic guided wave based imaging techniques have been considered as some of the most promising techniques for SHM, used widely in the aviation and transportation industries. Two of the most sophisticated guided wave methods are those which take advantage of a sound theoretical understanding of guided waves and numerical analysis – thus *tomography* and *phased array* [30] methods are very important. The analysis below gives the theoretical underpinning of these two techniques, followed by illustrations of the applications where they have been used to date in key areas.

a) *Tomographic measurement*

In order to conduct a tomographic SHM, a sparse array of guided wave sensors should be installed on the structure being monitored. Once an array is installed, the baseline data are collected from all the sensors in transmission. Guided wave data are reacquired at predetermined time intervals and the presence of defects is deduced from tomograms reconstructed using the guided wave parameters. The comparison of the guided wave features and baseline data feeds the tomographic image reconstruction algorithm and it generates the tomograms, showing the defect growth. The most commonly used features are the signal amplitude, wave velocity and mode conversion [20]. The concept of guided wave tomography initially started with the exploitation of the computational tomographic (CT) technique, which is used in X-ray imaging [31]. Combining CT algorithms with guided wave features, tomographs have been generated to reveal the structural integrity of metal plates [32], corrosion detection in aging aircraft [33], large area aircraft [34], impact detection on large areas of aircraft [35] and many more related uses. Apart from aircraft, the technique has been successfully applied to the inspection of pipelines, composites and welds [36 - 37]. One of the biggest challenges for this technique is the need for temperature compensation and a solution to suppress the effects of temperature during the experimental measurements.

b) *Phased array approach*

In the *phased array* approach, the array of sensors is installed in a compact format and only one accessible position is needed for the phased array to inspect and monitor a large structure by electronically and synthetically steering guided wave beams to all directions [30]. The phased array approach has been widely reported and used for plate structures [38], for aircraft panels [39], and steel plates, used in a wide variety of industries [40].

Several technical challenges can be seen when using guided wave techniques, for example unwanted wave modes, guided wave dispersion and complex wave behaviours in wave guides are associated with material anisotropy. To address these issues, one approach is to use an omni-directional guided wave transducer [38] which has uniform modal selectivity and directionality in any direction. When combined with different algorithms, this method has shown a significant advantage over the phased array approach. Another approach [40] is to achieve accurate measurement through the development of small transducers which have demonstrated reasonably good angular resolutions with an external excitation signal >160 kHz.

2.3.2.2 Ultrasonic Infrared Thermal Wave Imaging

Ultrasonic infrared imaging is based on the combination of ultrasonic vibration excitation and infrared imaging technology. This approach is typically used for detection of the cracks and disband/delamination on a variety of different materials and structures. The technique is not based on a heat excitation source, but sonic excitation. The principle of crack detection using sonic-IR is illustrated in Fig. 2.5, where a short burst of high power acoustic energy is launched by an ultrasonic source. Any defect present on the structure will cause the vibrations and crack interface to 'rub', which will result in an increase in the local temperature. An IR camera is then used to capture the thermal wave reflections from the sample for further study. This technique shows significant advances over earlier techniques, such as liquid penetrant testing and eddy current measurements [41] (discussed later in Chapter 2).

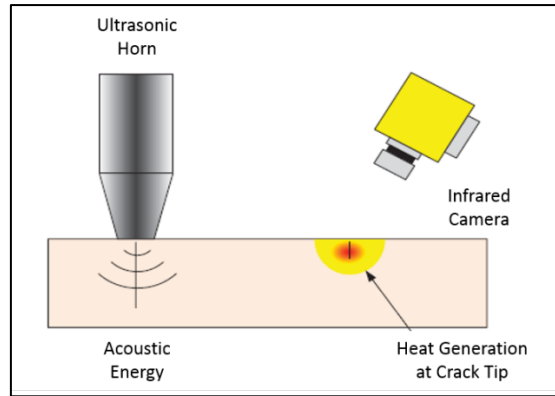


Figure 2.5 Crack detection using sonic-IR imaging technique [42].

The sonic-IR technique is capable of detecting cracks that have appeared on the millisecond time scale, where the cracks were visible in real time in the raw images taken. The inventors of the technique have shown that technology is capable of detecting fatigue cracks as small as around 20 micrometres in the metal samples [43]. For example, Xu *et al.* have examined a steel plate with fatigue crack and a juncture of carbon fibre composite that has been used in a space probe. This measurement approach has also proven to be attractive for the aviation industry [44].

2.3.2.3 Laser based imaging

i) Photothermal methods

Since the discovery of optical-to-thermal conversion, photo-thermal techniques have become an important tool for the study of this phenomena in various fields [45]. The launch of incident light in a sample causes heating due to the absorption of the light and subsequent conversion into thermal energy – thus resulting in various photothermal effects. Based on these effects, photothermal radiometry (PTR), photothermal beam deflection (PDS) and photothermal displacement methods have been developed and exploited in this field.

The PTR technique is based on using an intensity modulated laser-generated thermal wave, which causes changes in the amplitude and phase of the PTR signal. Due to its precision, the technique is used for micro crack diagnosis for automotive parts, for example. A camera and lock in amplifier are typically used to record the temperature changes of the detected signal that is recorded [46].

PDS is based on a mirage effect where absorption of the light causes a periodic heating and thermal gradient in the medium that causes bending of the light beam due to the changed

refractive index. The technique is mainly used for the semiconductors and polymer materials tests, the details of which have been reported by Cheng *et al* [47].

Laser-spot thermography was initially developed for detection of surface breaking cracks in metal components. Due to the presence of a crack in the material, the thermal impedance due to the restricted conduction is increased and as a result the surface temperature changes which can then be captured and interpreted [48]. The same authors carried out an experiment on using the samples with different cracks to compare the detectability of fatigue cracks by thermostatic inspection and laser-spot thermography. Another research group has developed two independent systems based on using a continuous wave (CW) laser and a pulsed laser beam for crack detection by laser spot thermography. Experimental results obtained demonstrated that cracks in the range of $\sim 1\mu\text{m}$ could be identified, with experiments being conducted on stainless steel and titanium plates [49].

ii) Photoacoustic Imaging

Photoacoustic (PA) imaging (also known as optoacoustic (OA) imaging), is based on the PA effect which was first reported by Alexander Graham Bell in 1880s, when he observed the audible sound created by illuminating a beam of sunlight onto a rubber sheet.

Zakrzewski *et al.* [50] have conducted nonlinear imaging of cracks by combining common PA imaging with additional acoustic loading. In this technique, acoustic signals at two different frequencies were launched into the sample, one excited by piezo-electrical transducer and the other by photo-acoustic excitation with an intensity modulated laser, as illustrated in Fig. 2.6.

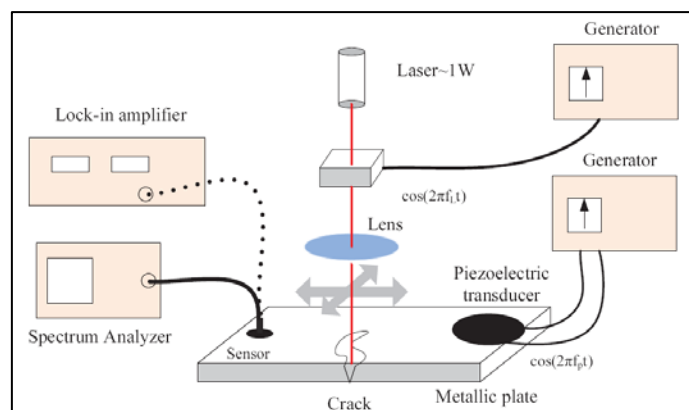


Figure 2.6 Experimental photoacoustic imaging setup [50].

A further technique that is based on the PA imaging, is termed laser ultrasonics (LUS). LUS is a remote, non-contact technique used for material characterisation, relying on the effect of irradiation of a short pulsed laser on the sample that also generates the compression, shear and

surface waves on the range of materials [25]. Fig. 2.7 shows an experimental setup of a laser ultrasonics approach.

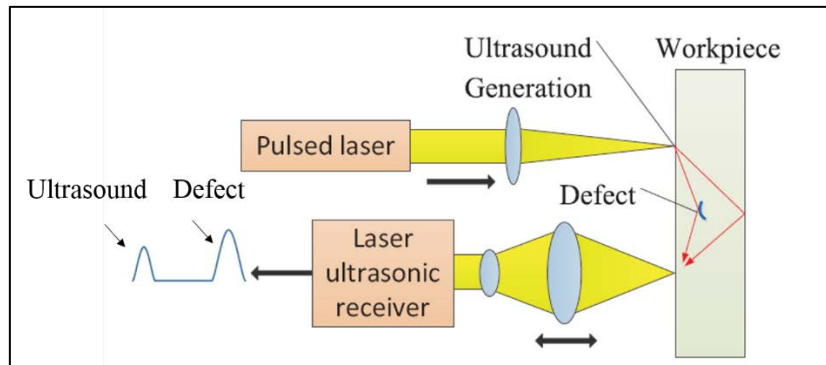


Figure 2.7 Experimental setup of laser ultrasonic method [25].

LUS has been reported with considerable success in the detection of voids in tendon ducts by impact echo diagnosis imagery, operating over the frequency range from 1-60 kHz. The same authors have used the technology for the characterisation of cover concrete in structures, using surface waves (SW) over the frequency range, 50-200 kHz [51].

iii) Holographic interferometry

Holography is based on the capturing and reconstruction of a light wave emanating from an object, where the wave front contains both amplitude and phase information, i.e. the intensity and spatial information of the image. Holographic interferometry captures a second image of the illuminated object in the same recording medium after the object has been disturbed by either mechanical or thermal means. The two different wavefronts that result interfere with each other and the fringes form an interference pattern (essentially a contour map of the deformation of the surface of the object) [52]. A typical holographic monitoring setup is shown in Fig. 2.8.

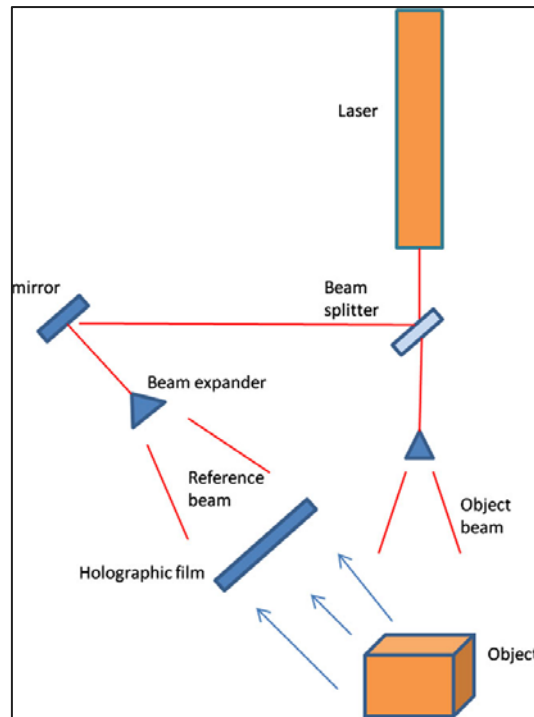


Figure 2.8 Typical holographic experimental setup [52]

This technique has been applied to a wide variety of problems related to the detection of the defects such as cracks, strains, corrosion, vibration analysis, etc. Stability considerations have often limited holographic interferometry to laboratory applications and only a few examples have been reported in 'in-the-field' industrial applications. These exceptions have mainly been based on the use of very robust, expensive and bulky optical systems, involving pulsed laser technology. The technique is limited to the use of only surface cracks. Recently developed high power fibre laser sources offer real potential for the future of this technique.

iv) Electronic Speckle Pattern Interferometry (ESPI)

Speckle is seen as a grainy appearance on a diffuse surface that is being illuminated by a source of monochromatic light [52]. A schematic diagram of the working principle of the ESPI technique is given in Fig. 2.9. The coherent light (from a suitable laser source) is scattered due to the roughness of the surface, where the scattered beam is then compared with a reference beam and in that way the information about phase is obtained (very much like holographic interferometry). Recent technological advances and the ability to use high resolution CCD cameras have facilitated the shift from holography to its counterpart ESPI. Holographic film processing and subsequent viewing of the images has been replaced by image acquisition using the camera and storing the image digitally, subsequently being used in the analysis and processing of the image stored. The technique is capable of measuring the deformation of the component under study – however it has been mainly applied in the laboratory rather than in

industrial applications ‘in the field’ – thus objects that need to be tested can be brought to the laboratory for examination under a controlled environment. Similarly to the holographic technique, this technique is limited to the surface cracks detection.

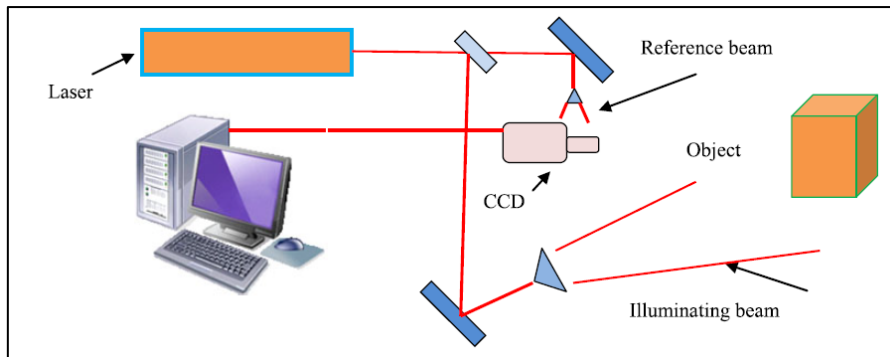


Figure 2.9 ESPI out of plane displacement measurement setup [52].

There has been a limited number of reports discussing the use of this technology outside the laboratory environment, with the technique used widely on aluminium plates for stress measurement. While successful experimental tests have been reported, the setup is very expensive and still requires operation in a controlled environment to provide the necessary stability [53].

v) Digital Shearography

This technique is based on using the speckle pattern, which has been created as a result of monochromatic light illumination of the surface of the object under test. The presence of defects is revealed by the fringe pattern created, depicting the gradient of surface displacement on the test piece. The fringe pattern is generated when either mechanical, thermal or any other stress is applied to the object. The images created are then recorded and subtracted from the images captured before stress was applied. A typical laboratory setup is shown in Fig. 2.10.

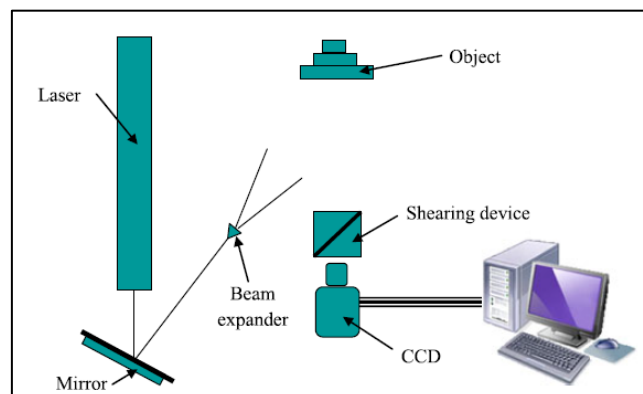


Figure 2.10 Shearographic laboratory experimental setup [52].

Digital shearography requires the image shearing device placed in front of the camera as illustrated in Fig 2.10 where two laterally displaced images are focused by the camera to the convenience of the operator in a horizontal, vertical or any other plane by the simple rotation of a shearing device.

2.3.2.4 Electromagnetic-Thermal imaging

Electromagnetic-thermal (EM-T) non-destructive inspection of structures combines electromagnetic illumination of the work-piece, and the heating of the material by induction and imaging by transient infrared thermography [54]. A coil creates a time-varying magnetic field which induces Eddy currents in the conduction material under inspection. In this way a temperature gradient is created within the material and the basic idea behind this principle is to exploit the property of current flow and heat transfer. In the structure without defects, the eddy currents circulate around the centre of the heated region and heat power is proportional to the square of the current density at that point and create the temperature gradients mainly along the radial direction. When a crack is present, it modifies the current flow as well as the temperature distribution. By employing infrared thermography, it is possible to visualise the temperature distribution and inspect the surface. Thermographic images can be evaluated to detect the major defects such as larger cracks.

Another method based on stimulated thermography employs pulsed eddy current (PEC), where short pulses of current (typically less than 1 s) are injected in to the samples with high intensity and images are acquired using an infrared camera. The technique has been reported for steel materials test as well as detecting defects and cracks in composites [55].

Kumar *et al.* have reported, the so called tone burst eddy current thermography (TBET), which is based on surface heating with the use of tone burst AC pulses [56]. Noethen *et al.* have carried out the thermo – inductive measurements of ferritic and austenitic steels where the metal test parts move through an inductor controlled by moving equipment and it is demonstrated in Fig. 2.11.

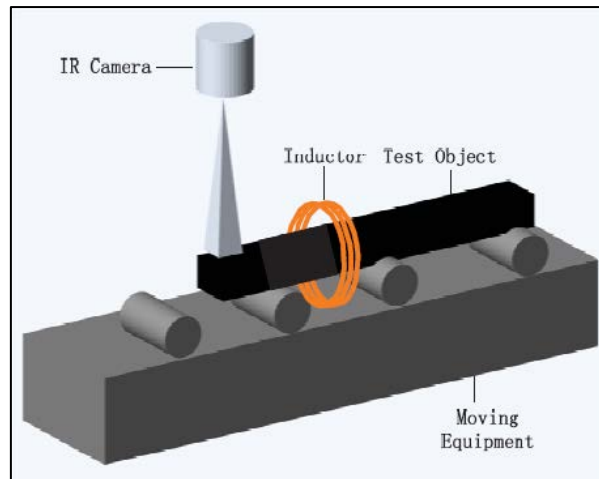


Figure 2.11 Experimental setup with the inductor controlled by moving equipment [57].

The EM-T technique has also been successfully used in the condition monitoring of different components of automotive and aeronautic industries. The main focus in those industries has been on crack detection on carbon fibre reinforced polymer (CFRP) materials [58]. The technique is used for the surface cracks on the sample. The same research group have built the PECT-stimulated thermography system at NUAU in Nanjing and have used it for the detection of three common defects in CFRP composites – cracks, impact damage and delamination [47]. The most common factors for the discrepancy are light intensity, lack of specialised knowledge, improper training of inspectors, etc.

2.3.2.5 Visual inspection

Visual inspection has been primarily used for bridge inspection in civil engineering. A detailed visual inspection of a structure is first completed and most of the decisions related to the structure maintenance are based on the assessments from visual inspectors. The visual inspections are usually scheduled for every two years. The study reported has clearly demonstrated the limitations of the technique, as large discrepancy in the results have been observed when the same structure has been inspected by different people [59]. In order to solve this issue, visual information should be collected automatically following standardized procedures. The system is so called remote access of image acquisition that has been proposed by several researchers.

Jahanshahi *et al.* have developed a visual monitoring system based on several cameras that mounted on the bridge to collect images [60]. Using the collected images, the scenes of the bridge are periodically constructed to evaluate the evolution of cracks or corrosion. Another approach that has been used is called robotic image acquisition system that has been reported

by Lee *et al* [61]. A robotic arm equipped with cameras scans the bridge and provides the images that are processed later. This system is very similar to the underbridge inspection vehicle where the bucket is replaced with the cameras [62]. The California Department of Transportation have developed a wired aerial robotic platform for close inspection of bridges or other highway structures. The vehicle is capable of vertical take-off and landing, translation to horizontal movement and orienting a video camera. It is controlled entirely by operating personnel on the ground.

More and more autonomous visual inspection is used and have been widely developed and used for civil, mechanical and aerospace structures. The work has been reported by several groups [62-63].

2.3.2.6 Magnetic Particle Inspection

Magnetic particle inspection is used to detect the cracks that are very close to the surface of a structure. The method reported by Ho *et al.* is based on the magnetic field applied through the surface of the specimen weld with the permanent magnet or electromagnet held against the metal [64]. The magnetised component is sprayed with the magnetic ink made of fine magnetic dust suspended in a thin oil. Considering the presence of cracks on the surface, a change in relative permeability occurs and a consequent change in the flux density is observed. This change of flux density attracts magnetic particles into the crack. Finally, an image of the prepared surface is captured and any cracks have been detected by an edge detection operator reported by Gonzalez *et al* [65].

The technique can only be used for the detection of the close to surface cracks and the main limitation is that it can only be used for the inspection of ferromagnetic materials. It means that stainless steel or aluminium both used as important materials in various industries could not be tested using this approach. Another drawback of the technology is that surface preparation is required for testing and possible demagnetization is needed following the inspection. In addition, inspection of a very large part requires a large current.

2.3.3 Liquid Penetrant Testing

Liquid penetration testing, called dye penetrant inspection, is used for finding discontinuities that are open to the surface of solid, essentially nonporous material [1]. Liquid penetrants that are used seep into various types of surface openings of micrometre scale. Therefore the process is well suited to detect all types of surface cracks, laps, shrinkage areas, laminations and similar

discontinuities. The equipment used is very simple and the staff does not require a specialised training, which is the advantage of the techniques.

In the liquid penetrant tests, the surface of the sample must be clean and completely dried before inspection. Liquid penetrant is then applied over the surface and beyond the area under inspection. The penetrant is then left on the area for some time to allow penetration into flaws. After that, the penetrant is uniformly removed, usually with water or particular solvents. Subsequently the developer which provides the necessary information for the visual inspection is applied. The surface is visually examined for indications of penetrant bleed back from surface openings. The visible penetrant inspection must be performed in a good white light illumination conditions. In the case that a fluorescent penetrant is present, the inspection is performed in a darkened area which causes the penetrant to emit visible light when illuminated by UV light source. It is very important to select the right developer for the surface under examination. For example for the smooth surfaces wet developer performs better than dry developer [1].

Gola has reported the use of this technique for tests on the metal structures and detections of the cracks on the surface [66]. The test still require the personnel to do the visual inspection, which is a limitation of the technique.

The main limitation of liquid penetrant inspections is that it can detect only imperfections that are open to the surface. Some other methods are needed for the detection of subsurface defects and discontinuities. The other limitation is that this technique cannot be used for the porous materials as the penetrant would enter the pores and register that as a defect.

2.3.4 Eddy Current testing

Eddy current inspection methods are based on the principles of electromagnetic induction and are used to identify the physical or structural condition of ferro-magnetic and non-ferromagnetic metal structures. In civil engineering, the technique is used for the detection of cracks, voids, and seams in structures [1]. The inspected parts or samples are placed within or very close to an electrical coil with alternating current. The alternating current, called the exciting current, causes the flow of eddy current in the sample under the test as a result of electromagnetic induction. The flow of eddy current depends on the electrical characteristics of the part, the presence or absence of discontinuities and the total electromagnetic field within the part. The condition of the part can be monitored by observing the effect of the resulting

field on the electrical characteristics of the exciting coil (impedance, induced voltage and induced current).

Kogonetal *et al* have inspected the effect of the carbon content on both electrical and magnetic properties of thermally treated carbon steels [67]. EC method has been successfully used for decarbonation depth detection during the treatment of various steels and it has been reported by Mercier *et al* [68]. Microstructural changes during the aging process of steel have also been tested using this method and reported by Rajkumar *et al* [69].

One of the great advantages of Eddy-Current technique is the capability to be used for subsurface cracks detection on ferro-magnetic materials. However, it has its limitations such as applicability to different materials and number of applications where ferro-magnetic materials are not used. In addition to it, this technique wouldn't be suitable for my work due to the environment in which the marine surfaces operate.

2.4 Optical fibre based non-destructive testing (NDT) methods

The sensing technologies reviewed in the previous subsections of this chapter have demonstrated several limitations, which could be overcome with use of optical fibre based sensors. The focus of this subsection is on optical fibre sensor principles for non – destructive measurement in various industrial applications. A very brief introduction and classification of optical fibre sensors is provided, with the main focus on optical fibre sensors for industrial applications.

2.4.1 Introduction

Optical fibre sensors have certain advantages over their electrical counterparts such as immunity to electromagnetic interference (EMI), lightweight, small size, and ease of implementing multiplexed or distributed sensors [70]. At the early stage of development, the initial applications for optical fibre sensors were harsh environments where conventional sensors were not well suited. Nowadays, optical fibre sensors are found in quite many applications for the measurement of various parameters such as temperature, strain, pH, humidity, pressure, vibration, acceleration, gas sensing and many more [6]. With the development of in-fibre Bragg gratings, interferometers, novel fibre types and nano technology, new applications areas have been opened where optical fibre sensors can be applied. There are a number of reviews on the subject where optical fibre sensors are used for various applications [70 - 75].

The classification rules for optical fibre sensors differs from one author to another. For example, according to Jackson *et al* [76], the sensors could be classified as coherent and incoherent. Other reviews used the classification based on the different measurands [77]. In addition, the simplest classification of optical fibre sensors is into *intrinsic* and *extrinsic* [71]. In the case of intrinsic sensors, light is being modulated whilst still being guided in the fibre. On the other hand, extrinsic sensors are based on the principle when light is transmitted by the fibre but modulated in a separate zone before being relaunched into the same or a different fibre for transmission.

The classification of optical fibre sensors proposed by Grattan and Sun [71], where classification is made according to the spatial distribution and OFS is as follows:

- 1) *Point sensor* – the measurement is taken at a discrete point.
- 2) *Quasi – distributed* - the measurement are made at pre-determined points along the single optical channel.
- 3) *Distributed* – the measurement can be made along the length of the fibre itself and they are designed in a way so they can discriminate in the spatial mode.

The categorisation of the OFS based on the spatial resolution is provided in more detail which is the main focus of this subsection. Particular attention is paid for NDE applications using these types of sensors.

Point FBG-based optical fibre sensors as well as quasi-distributed FBG-based optical fibre sensors are reviewed in the following chapter. The following subsection is focused on recent advances made in distributed sensing and reported by a number of research groups and commercial enterprises.

2.4.2 Distributed optical fibre sensors

Distributed optical fibre sensors (DOFS) offer an advantage over point sensors for global strain measurements. The number of sensing points covered by distributed sensing enables mapping of strain distributions in two or even three dimensions. The measurements made using this technique can be successfully used to reveal the global behaviour of a structure [78]. DOFS technology is based on either bonding fibres to the surface of a structure or embedding them inside the material or in case of distributed temperature sensing they could be just free of bonding or fixing to any surface. When an electromagnetic wave is launched into an optical fibre, the wave interacts with constituent atoms and molecules and the electric field induces a

time dependent polarisation dipole. This induced dipole generates a second electromagnetic wave and this is called light scattering. Depending on the type of the medium and whether the medium is homogenous or inhomogeneous, forward or backward scattering will be present respectively. Considering the inhomogeneous nature of the optical fibre and variations in the density and compositions, some photons will return to the light source and these produce the backscattering effect [79].

For distributed optical fibre sensing, it is essential to consider the required sensing range, the spatial resolution to be achieved as well as the measurement resolution/accuracy of the target measurand(s) using a single interrogator. Extending the sensing range using DOFS is challenging due to the attenuation of the fibre and power limit of a light source being used. Regarding the attenuation, it is reported that there is an exponential decay of intensity with the distance in optical fibres. Increasing the power of the light source can extend the sensing range, however, it does have limitations. Wang *et al* reported that with increasing the pump power [80], the nonlinear effect will occur to severely degrade the system performance.

When strain and temperature changes are transferred to the optical fibre, the scattered signal within the fibre is modulated by these physical parameters. The variation of this modulated signal is measured and distributed fibres sensing is achieved in that way [6]. In DOFS, scattering can be defined as the interaction between the light and an optical medium and there are three different scattering processes that can occur, namely: Rayleigh, Raman and Brillouin scattering [81].

2.4.2.1 Rayleigh backscattering systems

Rayleigh scattering is a result of the interaction of light within the fibre with inhomogeneities that are much smaller than the wavelength of light, as shown in figure 2.12a [82]. These inhomogeneities are mostly impurities in the glass and dopants that originate from the typical fibre manufacturing processes [83]. Each of these scattering sites is seen as an independent source with a random amplitude and phase, but at the wavelength of the incident light. Some energy is being trapped in the fibre and being transmitted back to the source as shown in figure 2.12b.

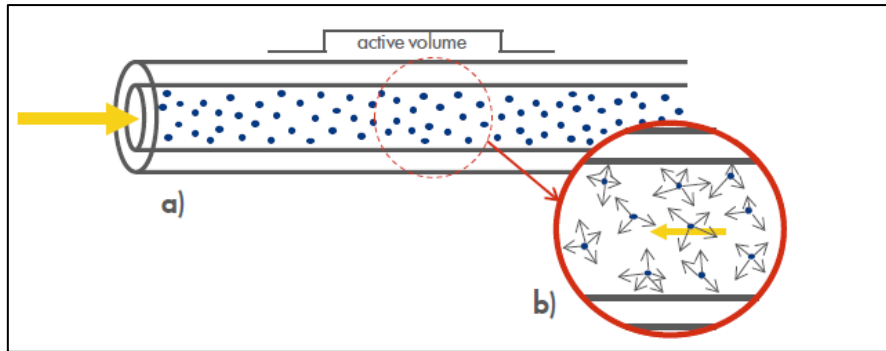


Figure 2.12 Rayleigh scattering of a light pulse in an optical fibre a) local inhomogeneities present in the optical fibre b) interaction of the light with the inhomogeneities causing Rayleigh backscattering

[82]

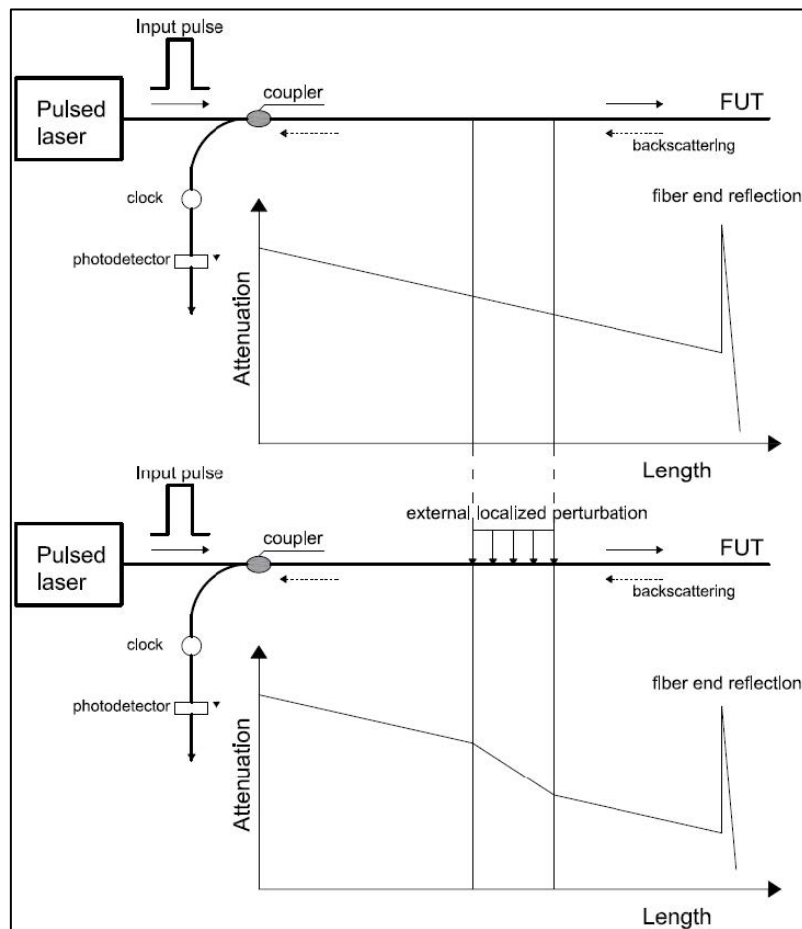


Figure 2.13 The basic arrangement of an Optical Time Domain Reflectometer (OTDR) [78]

The schematic diagram of the functional OTDR is shown in Fig. 2.13. A laser is used to launch short optical pulses into the fibre. The pulse is attenuated via several mechanisms while traveling through fibre. One of the mechanisms is Rayleigh scattering which is guided by the fibre back to the launching end and detected by the receiver.

In order to provide high spatial resolution with OTDR, a very narrow pulse is needed. The shorter pulse increases the noise levels making detection of small variations of strain and

temperature almost impossible. In that way, a DOFS technique with millimetre scale spatial resolution and based on Rayleigh scattering has been developed and called OFDR. This technique is also known as an Optical Backscattered Reflectometry (OBR) [84]. OFDR is based on the measurement of interference fringes of the Rayleigh scattered light from a tuneable laser source and a static reference fibre in frequency domain. The amplitude and phase in the frequency domain are converted to the time/spatial domain using the inverse Fourier transform (IFT) [85].

Hoult *et al* have conducted a series of axial tension tests on steel plates using OBR DOFS with nylon coated and polyimide coated fibers, where they observed the slippage between nylon coating and inner core which affected the accuracy of measurement [86]. This technology has also been used for strain measurement on reinforced concrete with fibre optic being installed in the grooves of the rebars [87]. Reinforced concrete beam of rectangular cross section was subject to four – point bending through Rayleigh-based DOFS where the location cracks were detected before the visual inspection [88]. Gifford *et al.* performed tests in order to evaluate the applicability of Rayleigh scattering for temperature sensing [89]. The metal rod was resistively heated up to 600 °C and then was a subject to a thermal gradient by dropping water on localised spot on the rod. Rayleigh backscattering has also been reported where localised heating was measured with millimetre spatial resolution for the nuclear industry [90].

Several researchers have implemented an OBR monitoring system based on Rayleigh scattering on the slab of the highway viaduct and achieved the millimetre spatial resolution for load testing [91 - 92].

Casas *et al.* have reported the monitoring of a cooling tower in Spain using OBR system [93]. After two main cracks appeared on the structure, DOFS has been implemented in order to monitor the structure behaviour before and after crack was repaired with the main goal to increase the life time of those important structures.

Regarding the dynamic capabilities, the first reported Rayleigh scattering based OTDR vibration sensor was achieved by polarisation based OTDR with 5kHz event detection and spatial resolution of 10 m [94]. Later, OTDR based on the coherent detection of the phase has been reported with the spatial resolution of 0.5 m over 1 km sensing length [95]. Rayleigh based OFDR has also been used for distributed dynamic measurement and reported by the same authors [95].

Rayleigh back scattering has also been successfully used and widely reported for acoustic emission detection. Lomonosov *et al* have reported the use of the technique for the surface cracks sizing [96]. In this case surface acoustic waves (SAW) have been used for the investigation of surface cracks. The reflections of short SAW pulses from the crack edges possess the time delays which depend on the crack depth.

One of the recent advances made in OTDR is so called phase sensitive optical time domain reflectometry (Φ -OTDR) reported by Wang *et al* [80]. In this technique, highly coherent pulses are used as the probe light and detection of the coherent intensity of the Rayleigh backscattered pulses is achieved. The technique has been proven to be much more sensitive than conventional OTDR and is well suited for underground deployments, such as masked intrusion detection or pipeline monitoring. It is also been reported that, phase demodulation rather than intensity is widely used for the so called, Distributed Acoustic Sensing (DAS) [97].

Wang *et al* have reported that a combination of distributed amplification and coherent detection can extend the sensing distance as well as enhancing the sensitivity. Their technique, so called, ultra-long Φ -OTDR can achieve high sensitivity detection over 131.5 km fibre length with a spatial resolution of 8 m [80].

One of the most recent commercially available distributed temperature and sensor systems is presented by Luna technologies, where the spatial resolution of 10 μm can be achieved when 70 m distance is monitored. However, this system is not suitable for my work due to the cost of the system and the dynamic range that needs to be achieved.

2.4.2.2 Raman Scattering

The Raman Effect is a scattering effect of light where light scattering occurs as a consequence of fluctuations in the optical fibre medium. Raman scattering can occur in two distinguished forms: Spontaneous Raman Scattering and Stimulated Raman scattering (SRS). In the spontaneous form, scattering occurs when the incident field interacts with vibrational modes, mainly excited by thermal effects of the molecules constituting the medium. As a result of this interaction, there is optical phonon as well as down shifted and up shifted photons. The frequency of the phonon is related to the normal vibrational modes of the molecules of the medium and in that way by analysis of the light, the information about medium can be retrieved [98]. Stimulated Raman scattering (SRS) takes place when some Stokes photons have previously been generated by spontaneous Raman scattering and somehow forced to remain in the material or when deliberately injecting Stokes photons together with original light.

The Raman distributed temperature sensor was pioneered in mid-1980s by Dakin *et al* [99] and soon after developed into a commercial instrument by several companies. The same authors explained the working principle of Distributed Anti-Stokes Raman Thermometer (DART) [100]. A pulsed laser of 3W of optical power in 15ns pulses was launched into a sensing fibre, yielding spontaneous Raman scattering, and as a result anti – Stokes and Stokes photons are generated along the fibre. A fraction of the scattered photons is propagated back towards source where they are detected by a fast photodetector. In order to improve the sensitivity and range of the method, the laser pulse width was adjusted to be 200 ps in which a semiconductor gain-switched laser was launched into a multimode graded-index fibre [101-102]. A concrete slab has been instrumented with Raman-, Brillouin- and Rayleigh-based DOFS in order to obtain strain measurements. Raman scattering has been used for temperature compensation, while Rayleigh scattering provided more promising results than BOTDR in terms of spatial resolution [103].

Distributed temperature sensing has been very well developed and commercialised by several companies with great success on numerous industrial applications.

The Distributed Temperature Sensing (DTS) system (marketed by Lios) has been successfully used for fire detection in road and rail tunnels, in oil & gas industry as well as the other sectors. The Optical Frequency Domain Reflection (OFDR) method has been used to provide information on the local characteristics by monitoring the backscattered signal as a function of frequency prior to Fourier transformation, providing a higher signal-to-noise ratio compared to the use of an Optical Time Domain Reflection (OTDR) method. This approach provides distributed temperature measurement with a spatial resolution of 0.25 m along the optical fibre with a monitoring range up to 10 km per channel with a measurement range from – 180°C to +1000°C and temperature resolution of 1°C. The OTDR-based system (marketed by Silixa) enables temperature measurement from – 40 °C to 65 °C with a spatial resolution of around 12.5 cm and temperature resolution as low as 0.01 °C.

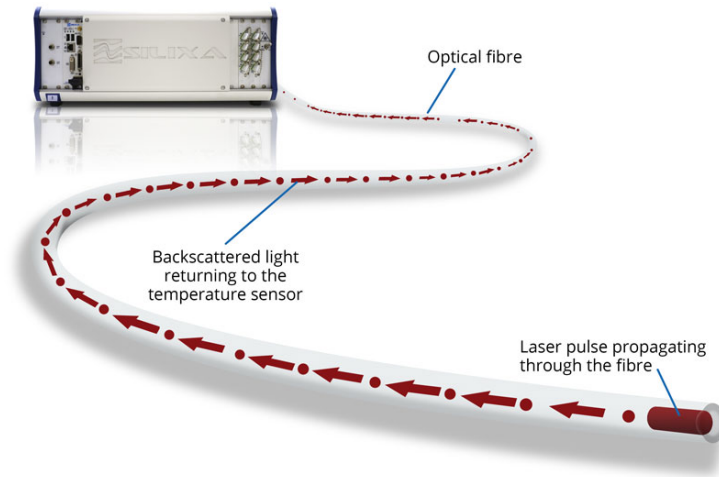


Figure 2.14 ULTIMA Distributed Temperature Sensor developed by Silixa [104]

2.4.2.3 Brillouin Scattering

Brillouin scattering occurs as a result of acoustic vibrations stimulated in the optical fibre. Those vibrations within the fibre produce a counter propagating wave which is called the Brillouin scattering wave. This backscattered light has a characteristic frequency shift, called the Brillouin Frequency shift (BFS) which is a function of local temperature and mechanical stress [105]. For standard single mode fibres using a wavelength around 1550 nm the near – room temperature sensitivity is around 1 MHz per °C. In order to obtain the necessary information related to the fibre’s surrounding temperature and strain distributions, an appropriate interrogation technique has to be selected. One of them was initially introduced to enhance the range of OTDR and is called Brillouin optical time domain reflectometry (BOTDR) [106]. The other configuration is based on stimulated scattering and is called Brillouin optical time domain analysis (BOTDA). This technique uses two counter propagating lasers and is reported in more detail by Bao *et al* [107].

BOTDR and BOTDA-based distributed optical fibre sensing systems have been extensively used for slopes testing in geotechnical structures and are widely reported [108] [109]. Oil and gas industry have been one of the early adopters of distributed optical fibre sensing. Glisic and Yao have conducted a large scale test on a pipeline with the main goal to provide real-time monitoring of pipelines that were subject to permanent ground movements induced by earthquakes. The technique used is based on stimulated Brillouin scattering [110]. Distributed fibre optic sensors based on stimulated Brillouin scattering have also been used for the instrumentation of bridges for the cracks detection which required continuous monitoring of these structures [5], [111] and [112].

In order to evaluate the structural fatigue that results from seismic activities and material deterioration, the dynamic strain has been monitored using Brillouin based distributed sensing [113]. Bao *et al.* have demonstrated the field application of impact wave detection on a concrete deck excited by the passing of a car at a frequency up to 300Hz [94]. All three scattering effects most likely used in silica optical fibers are shown in Fig. 2.15 considering that the wavelength of the launched light is 1550 nm.

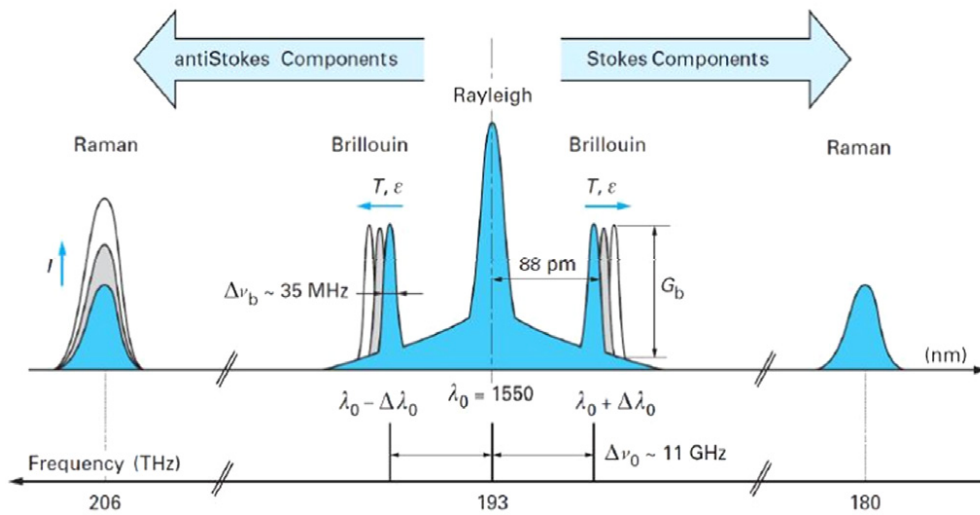


Figure 2.15 Rayleigh, Brillouin and Raman scattering for distributed optical fibre sensing systems [105].

One of the main disadvantages of BOTDA/BOTDR is that cost is really high and the spatial resolution is sacrificed when large distances are considered. These techniques are not suitable for my project mainly due to the cost of the system. The most well known commercial enterprise with most advanced BOTDA and BOTDR solutions is OZ optics.

2.4.4 Optical fibre interferometers

Interferometric techniques have been used for displacement measurement for many decades. They can provide very high sensitivity when the technique is used in an appropriate way for the measurement of a particular physical parameter. Different interferometric configurations have been reported for acoustic and ultrasonic sensing and this subsection is focused on the review of these techniques. Figure 2.16 shows the intrinsic optical fibre interferometers applied as non-destructive testing methods.

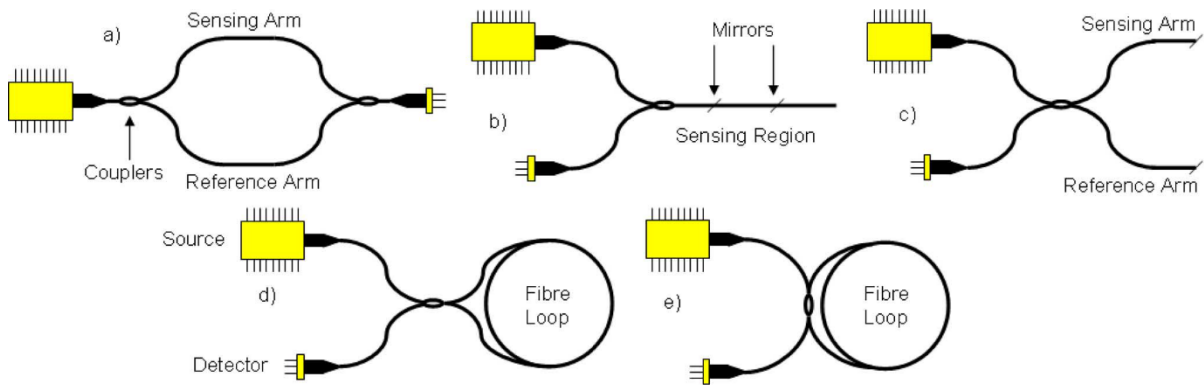


Figure 2.16 Intrinsic optical fibre interferometers a) Mach-Zehnder; b) Fabry-Perot; c) Michelson; d) Sagnac; and e) ring resonator [10].

Figure 2.16a, shows a Mach-Zehnder interferometer (MZI), where the incident light is split into two arms and then recombined by using another fibre coupler. The recombined light has the interference component created by the optical path difference between these two arms. For sensing applications the reference arm is kept isolated from any external variations [114].

Regarding the applications, MZI based techniques have been used for ultrasonic wave detection in the frequency range from 40 – 400 kHz. The technique has been used for the detection of ultrasonic waves under water. Cole *et al.* have tested the directivity of measurements from -30° to 30° , showing very strong directional dependence [115]. The main limitation of this technique is that it is mainly used in the laboratory environment.

Another interferometric approach, demonstrated in Fig. 2.16b, is called Fabry-Perot interferometer (FPI), which is generally composed of two parallel reflecting surfaces separated by a certain distance. In this type of sensor, interference occurs due to multiple superpositions of both reflected and transmitted beams at two parallel surfaces [116].

One of the very widely reported approaches is called the Extrinsic Fabry – Perot Interferometer (EPPI) and is constituted by a capillary silica tube containing two optical fibres facing each other with the short gap in between. The schematic diagram of EPPI transducer used for both chemical and physical point transducers is shown in Fig. 2.17.

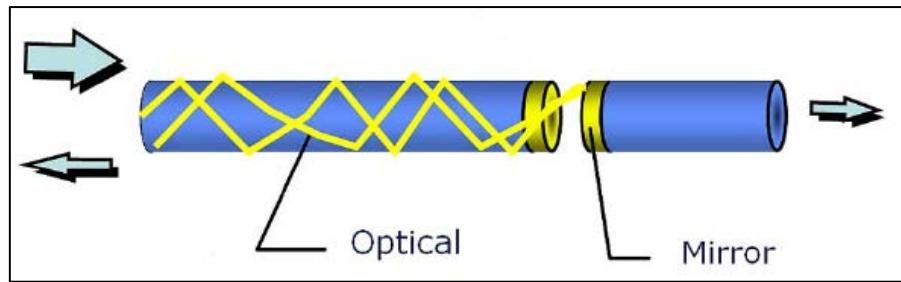


Figure 2.17 Schematic illustration of EPPI transducer [6]

When light is launched into one of the fibres, due to the reflection of the incoming light on the glass to air and on the air to glass interface, a back reflected signal is obtained. The interference can be demodulated using coherent or low coherence techniques to reconstruct the changes in the fibre spacing [117]. This sensor design was widely reported and used for long term, high precision strain measurement of a very small deformations on a mechanical diaphragm [118]. It has been reported that EPPI fabricated interferometric sensor could also be used for acoustic field measurements over the bandwidth of 2.5 MHz [119].

The intrinsic FPI includes reflecting components inside the fibre itself. There are a wide range of methods used to form a cavity, such as micro matching [120], use of two FBGs [121], chemical etching [122] and thin film deposition [123].

The Michelson interferometer layout is shown in figure 2.16c. The Michelson interferometer causes interference by splitting a beam of light into two parts. Each part is made to travel a different path and brought back together where they interfere according to their length difference. It is essential to adjust the fibre length difference between the reference arm and the sensing arm of a Michelson interferometer (MI) within the coherence length of the light source [124].

The configurations of a Sagnac interferometer (SI) and a ring resonator are shown respectively in figures 2.16d and 2.16e. In the Sagnac interferometer configuration, the light from an optical source is injected through a beam splitter such that it traverses in two directions around a loop. If that loop is rotated, the light propagating in the same direction as the rotation has to 'chase' the beam splitter while the light in the opposing the rotation finds the beam splitter advancing towards it. As a consequence of that, the two directions within the rotating loop will have slightly different optical paths and this difference is detected using optical interferometry. The Sagnac interferometer therefore detects rotation. Measuring the rotation is an essential part of virtually all navigation systems and many surveying systems. Wang *et al* have reported the use of an EDFA-based fibre ring laser and Sagnac interferometer for the acoustic sensing of particle

discharge in power transformers. In their case SI was used to eliminate the intensity noise and enhance the SNR in the system where they achieve a high-frequency response bandwidth of 300 kHz. The SI used consists of two individual, identical SI, both sharing a fibre coil as the sensor and using two relevant, low – coherent probe lights with identical optical power [125]. Similarly to SI, optical fibre ring resonators have been widely used in gyroscopes. The fibre optic ring resonator is a high accuracy inertial rotation sensor based on the Sagnac effect.

The majority of the optical fibre interferometric approaches have been confined to use in the laboratory environment where conditions are well controlled and under these conditions the technique can deliver the required performance. In that case, most of the samples that need to be tested require to be brought to the laboratory where tests have been completed.

2.5 Summary

This chapter provides a comprehensive review of existing sensing technologies that have been widely reported and used for the non-destructive testing of a variety of concrete/metallic structures. This chapter was divided into two main subsections, i.e. optical fibre and non-optical fibre techniques. Non-optical fibre techniques include acoustic emission techniques (ultrasonic testing and guided wave testing), imaging techniques (acoustic, thermal, laser and magnetic imaging techniques), liquid penetrant testing and Eddy current method. Optical fibre techniques include distributed optical fibre techniques (Rayleigh backscattering, Raman scattering and Brillouin scattering techniques) and optical fibre interferometers (Mach-Zehnder, Fabry-Parot, Michelson, Sagnac and ring resonator).

Chapter 3

Fibre Bragg Grating Based Sensors

3.1 Introduction

This chapter begins with the introduction of fibre Bragg gratings which have been recognized as an important fibre structure widely used both in telecommunications and in sensing. The main properties of FBGs are discussed including their classification and inscription techniques. The focus of this chapter is a comprehensive review of FBG based optical sensors used either as point or quasi-distributed measurement devices for non-destructive structural condition monitoring.

3.2 Background

A fibre Bragg grating (FBG) is an in-fibre device formed by periodic refractive index modulation through the exposure of the optical fibre core to the created mainly by UV interference pattern [126]. The device created as a result of this process behaves as a wavelength selective filter which is sensitive to both strain and temperature. A typical fibre Bragg grating is illustrated in Fig. 3.1, where a narrow-band spectrum is reflected and centred at a wavelength termed the *Bragg wavelength*, λ_B , when it is illuminated by broadband light.

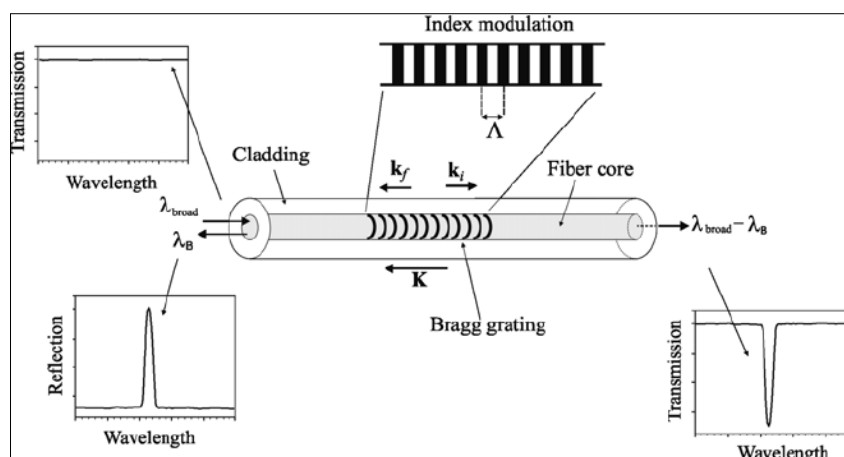


Figure 3.1 Illustration of a fibre Bragg grating [126].

The photosensitivity of such a fibre was first discovered at the Communication Research Centre (CRC), Ottawa, Canada in 1978 [127] when the first FBG was observed. These initial devices

were of limited practical use as they were limited to the operation at the writing wavelength. Some years later, Meltz *et al* discovered that strong changes in refractive index could be induced using wavelengths in the region 240-250 nm [128]. These wavelengths are related to the photon energies that match an absorption peak associated with material defects due to germanium doping in the silica fibre. This discovery allowed greater flexibility in making refractive index gratings in optical fibre. The phenomenon of photosensitivity in optical fibres was originally associated with germanium dopant. Doping silica with germanium provides an additional set of possible defects in the material that are widely considered to be responsible for the photosensitivity observed in germanosilicates. It is generally accepted in the literature that formation of particular point defects associated with germanium play a crucial role in photosensitive response. Increasing the germanium content is known to increase the concentration of the related germanium oxygen deficiency centres (GODCs). Two such defects that play a significant roles are the Ge^{2+} defect with an absorption at 241 nm and the neutral oxygen vacancy with an absorption at 245 nm.

Considering the other dopants that could be used, germanium is not the only solution. Raising the germanium dopant levels leads to a higher photosensitivity. However, if dopant levels are too high, the refractive index will be higher than desired and optical loss will be increased as well as mechanical strength decreased. To avoid these undesirable effects, additional co-dopants have been discovered and used. For example, by adding boron into silica lowers the refractive index and enhances the photosensitivity [129]. There are a variety of other co-dopants that have been reported and successfully used to enhance the photosensitivity and at the same time control the refractive index change such as, tin, nitrogen, europium and cerium [130]. However, none of these co-dopants can enhance the response to the same level as that of a single dopant as germanium.

A commonly used method to improve the photosensitivity without dramatically changing the properties of glass is called hydrogen loading [131]. In this process, high pressures have been used to diffuse hydrogen into the silicate matrix when in the preform state. Exposure of the loaded glass to UV allows permanent index changes to be induced in planar waveguides. Such loading procedures have demonstrated the effectiveness at enhancing photosensitivity in both germanium doped and germanium free fibers, and have the advantage that hydrogen in the unexposed glass will diffuse out, leaving the glass as it was prior to loading.

3.3 FBG Inscription methods

The FBG inscription techniques used to date can be generally divided into two main groups, namely *internal* and *external*. The internal writing technique was reported by the pioneers of photosensitivity of optical fibres and the formation of Hill-grating [127] which is discussed in the previous sub section. The range of the external writing techniques have been proposed by various researchers, such as interferometric techniques [128], point by point [132] and phase mask methods [133]. The FBG sensors used for this work are manufactured using a phase mask method, and hence this method will be explained in more detail. Regarding the methods based on point by point FBG manufacturing and interferometric approach, the short description and the associated references will be provided.

a) Interferometric techniques

The two techniques that belong to the interferometric approach and reported in literature are *Amplitude splitting* and *Wavefront splitting* interferometric approaches. The amplitude splitting interferometer that consists of a beam splitter and set of mirrors is shown in the Fig. 3.2. and reported by Meltz *et al* [128]. A UV laser beam is divided and subsequently recombined to generate a two-beam interference pattern which was imprinted onto the core of the photosensitive optical fibre to create a permanent refractive index modulation which is necessary for the Bragg grating formation.

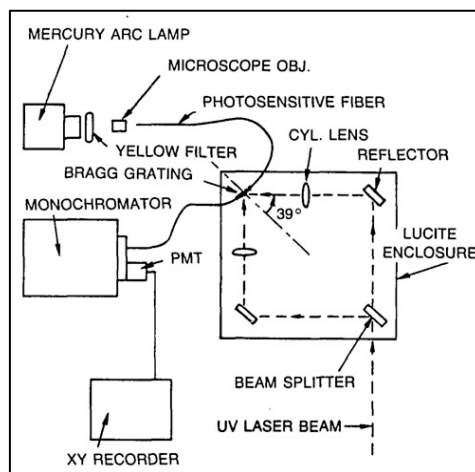


Figure 3.2 Schematic diagram of amplitude splitting interferometer reported by Meltz *et al* [128] demonstrating side written FBG.

This fabrication setup is quite sensitive to mechanical vibrations and it requires a precise alignment of the optical components. Two types of interferometers have been used as wavefront interferometric methods for FBG manufacturing. The first approach is based on the

so called Lloyd mirror. In this configuration the mirror is positioned orthogonally in relation to the fibre and the incident beam is centred at the position where the mirror and fibre intersects. With this positioning of the mirror, half of the incident beam passing through the mirror is guided directly to the fibre and the other half is reflected from the mirror to the surface. An interference pattern for grating inscription is formed in this way by overlapping of those two beams. The schematic diagram of this technique is shown in Fig. 3.3.

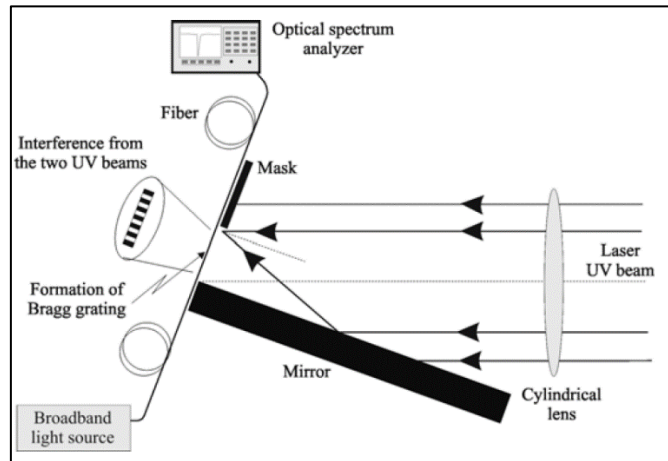


Figure 3.3 Schematic diagram of Lloyd interferometer [130].

The second approach is based on the use of a prism instead of the mirror and in that case the incident laser beam is expanded through refraction at the input face of the prism. One half of the beam is guided directly on the fibre and the other is guided through the total internal reflection to the same point as the direct one. This is how the interference pattern is established and grating inscription achieved and the schematic diagram is shown in Fig. 3.4.

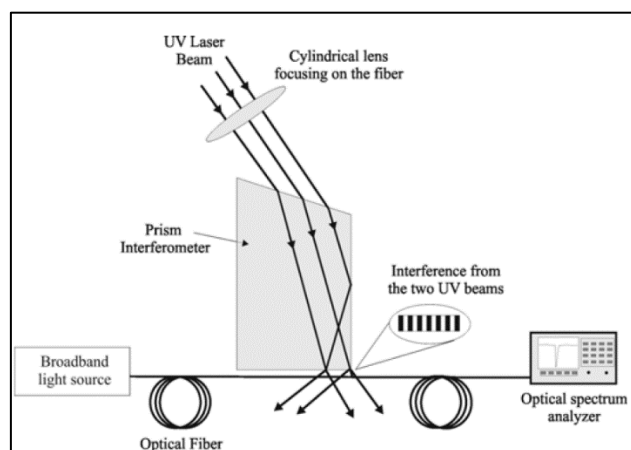


Figure 3.4 Schematic of prism based wavefront splitting interferometer [130].

Considering the need for only one optical component in the system, the wavefront splitting interferometer is less complex than amplitude based interferometers. Also, the shorter distances that beams need to travel, makes this technique more stable than amplitude splitting.

b) Phase Mask technique

This technique is one of the most common methods for inscribing the fibre Bragg gratings in photosensitive fibre. The phase mask technique has been proven as an effective and simple way of fabricating FBGs with much higher tolerance against mechanical vibrations in comparison with interferometric techniques. The high repeatability of this technique is of critical importance to achieve FBG manufacturing in high volumes.

The main element of this technique, used to spatially modulate the UV laser beam is called the phase mask. The phase mask as a diffractive optical element, is a surface – relief grating etched onto a UV transparent silica substrate using photolithography techniques [130]. The profile of the phase mask is chosen such that when UV beam is incident on it, the zero order diffracted beam as shown in Fig. 3.5, is suppressed to less than a few percent – typically less than 3% of the overall transmitted power. Regarding the plus and minus first orders, they are maximised so that they typically contain more than 35% of the transmitted power [130] to ensure the creation of a strong interference pattern created for writing FBGs. The fringe period that corresponds to the period Λ from Eq. 3.1 is half a period of the phase mask. The selection of the phase mask to produce an FBG at a specific wavelength is independent on the wavelength of the UV laser, but the etch depth required to suppress the zero order is a function of wavelength and optical dispersion of the silica substrate used for the phase mask. The schematic of this technique is given in Fig. 3.5.

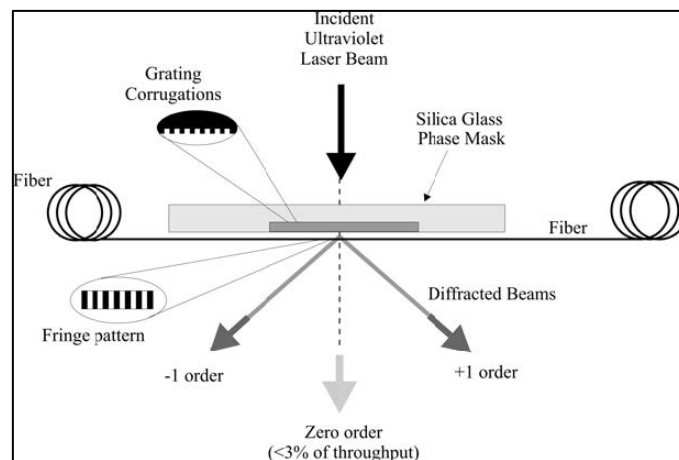


Figure 3.5 Schematic illustration of phase mask technique for FBG manufacturing process [130]

During the manufacturing process, a photosensitive fibre is placed directly behind and in very close proximity to the phase mask and in that case sensitivity to mechanical vibrations and stability problems are minimized. The FBG is manufactured by fibre exposure to the fringe pattern created from the interference of the plus and minus one orders of the transmitted power. The most common used light source for FBG fabrication is Krypton Fluoride (KrF) excimer laser. More details about the setup used for manufacturing process of FBGs used for this research is given in the Chapter 4 where experimental work is reported.

Another technique that has been used for manufacturing FBGs into standard telecommunication fibres (without photosensitivity) is based on the use of femtosecond – IR laser in combination with phase mask. This was first demonstrated in 2003 and reported by Mihailov *at al* [134]. A typical FBG inscription setup using a femtosecond-IR laser is shown in Fig. 3.6, where a laser with 125 fs duration pulses and 800 nm wavelength is used to illuminate various types of fibres by passing the beam through a cylindrical focusing lens and a phase mask.

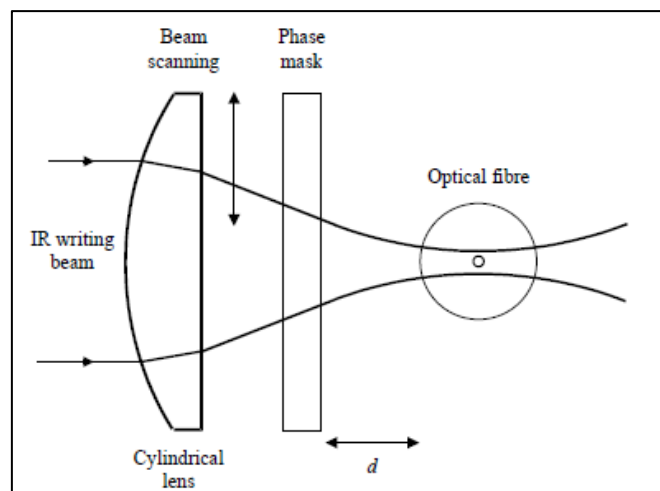


Figure 3.6 Schematic diagram of femtosecond-IR laser FBG writing technique [134].

The phase mask generated a sinusoidal interference resulting in a non-sinusoidal modulation of the refractive index of optical fibre. The diameter of the beam incident on the focusing lens was typically 6.4 mm with pulse energies ranging from 0.2 to 2 mJ/pulse. The distance d in the Fig. 3.6 refers to the distance between phase mask and the nearest edge of the optical fibre.

There are various types of fibres widely reported and successfully used for FBGs manufacturing using this technique, such as borosilicate glass fibres [135], fluoride glass fibres [136], silica and phosphate glass fibres [137], pure silica photonic crystal fibres and tapers [138], sapphire fibers [139], etc.

Inscription of narrow-band fibre Bragg gratings using 264 nm femtosecond laser pulses and phase mask has been reported by Kelleher *et al* [140]. The experimental setup based on the scanning phase mask technique is shown in Fig. 3.7. It is reported that they have used Ge/B codoped H₂ free optical fibre, supplied by Fibercore, Ltd., UK. The fibre itself had a Ge content of about 10 mol% and a core diameter of 7.1 μm . For the grating inscription femtosecond UV laser pulses were used and they were directed by a 22.3 cm fused silica cylindrical lens onto the fibre through a phase mask. The fibre was placed behind the phase mask at a distance of 100 μm .

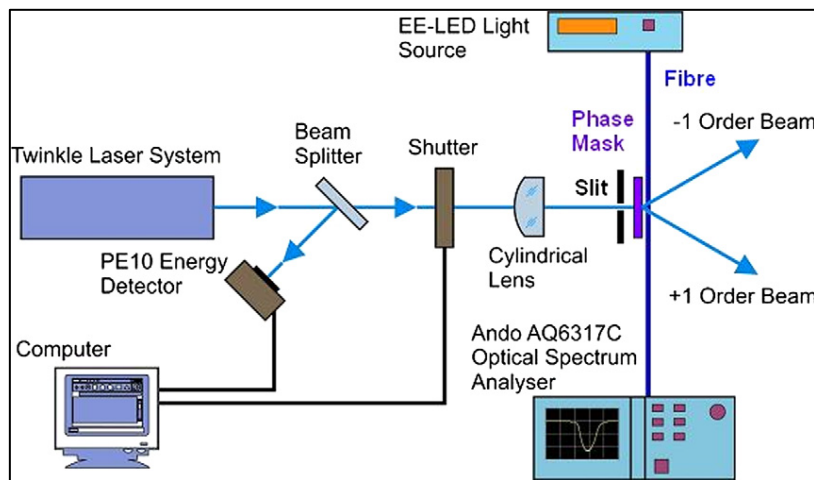


Figure 3.7 Experimental set-up for FBG fabrication using femtosecond 264 nm pulses [140].

In order to provide the movement of the phase mask, a linear positioning stage was used and controlled by the DC motor controller. In order to provide a narrow-band FBG, a 2.3 mm slit was used and placed in front of the phase mask at a distance of 7 mm away from the phase mask. The movement of the phase mask system is in the direction perpendicular to the inscribing laser beam.

Another technique that is based on the use of the phase-mask and UV beam as a light source belongs to the group of polarisation – controlled methods. In this technique, a polarisation beam splitter moves together with a UV beam. Both fibre and a phase mask are stationary during the exposure. The moving splitter introduces a divergence angle between the propagation vectors of the *s* and *p* polarisation of the UV beam. These beams result in a slightly displaced index modulation profile in the fibre core. The phase shift between these profiles depends on the divergence angle, the optical distance from the phase mask to the fibre core and the period of refractive – index modulation [141].

Considering the increased demand for FBG sensors over past decades, as FBGs have found numerous applications in various industrial sectors, there was a need to develop a fabrication system that could offer both flexibility and speed in writing a large variety of grating types. One of the first commercially available lithography methods were reported by Ieuwland *et al* [142]. The manufacturing process reported provides the ability to manufacture large volumes in a very short period of time. The experimental setup is shown in the Fig. 3.8.

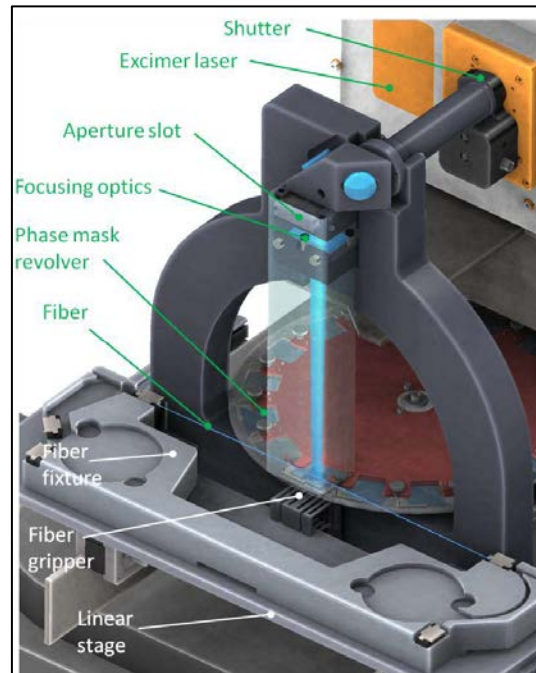


Figure 3.8 Functional modulus of the novel FBG manufacturing technique [142].

In this approach, an excimer laser operating at a wavelength of 193 nm was used with a nominal pulse energy of 5 mJ per pulse and a maximum repetition rate of 500 Hz. Regarding the optical assembly in this technology, high grade fused silica lenses and mirrors were set to efficiently expand, rotate and focus the beam from the laser. The laser beam was conditioned in such a way that it was 10 mm in length and 20 μm in width hits the fibre placed underneath the phase mask. By controlling an aperture slot, FBGs of varying lengths could be manufactured. By using a photonic energy from 193 nm, the refractive index change was reported to be achieved in wide variety of fibres, pure silica fibres [143], rare earth doped fibres [144] and phosphate and fluoride glass fibres [145]. However, an optimal performance was reached using either germanosilicate or hydrogen loaded fibres.

c) Point – by – point FBG manufacturing

This technique is based on the illumination of the fibre core to a highly focused KrF excimer laser beam. By repeated exposure of the optical fibre to the single spot of the focused UV laser

beam, the refractive index modulation profile along the fibre was formed. This technique was pioneered by Malo *et al* and it is reported that pulses of 248 nm laser beam were used to demonstrate the fabrication of a third order FBG with a period of 1.59 μm and grating length of 360 μm [132].

Another approach widely reported and based on the point-by-point FBG writing method is the use of femtosecond lasers. In this technique, periods of the grating are written individually using a low repetition rate femtosecond laser which is spherically focused into the core of an optical fibre using a microscope objective. The period of the grating is given by the ratio of the translation velocity to the laser repetition rate. In this case, there is an opportunity to write gratings for any operating wavelength. The experimental setup reported by Marshall *et al* [146] is shown in the Fig. 3.9.

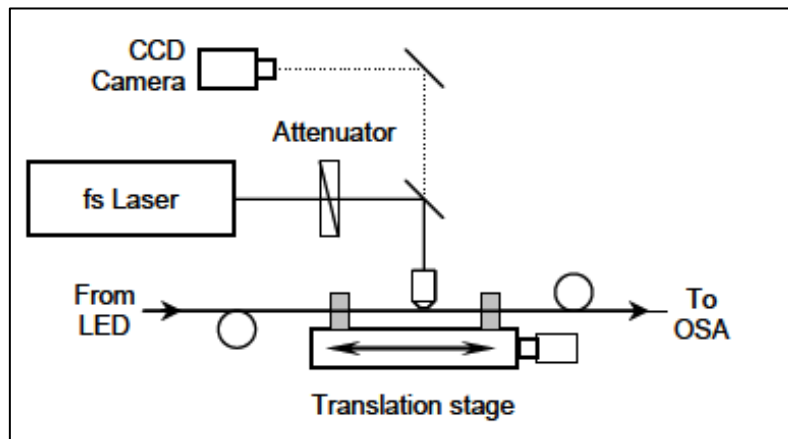


Figure 3.9 Femtosecond FBG writing approach using point by point method [146].

In the experimental setup reported by Marshall *et al*, a pulse laser with an operating wavelength of 800 nm and 120 fs pulses was used at a repetition rate of 1.00 kHz. The output of the laser was attenuated and focused into the core of the optical fibre using an oil-immersion 20 x 0.8 NA apochromatic microscopic objective. The optical fibre, mechanically stripped of its polymer jacket, was mounted on an orthogonal three – axes computer controlled translation stage system. The FBG characteristics were monitored using an edge-emitting LED and optical spectrum analyser (OSA).

3.4 Classification of Fibre Bragg grating sensors

The Fibre Bragg grating sensors discussed in this section are the sensors manufactured on a single mode optical fibre. The same sensors were used for this work. Fibre Bragg gratings can

be classified based on the growth dynamics of the grating during the inscription process, such as type I, type IIA and type II gratings respectively.

a) Type I FBGs

Type I FBGs are the most commonly used FBGs in both telecommunication and sensing applications. This type of FBG can be manufactured in most photosensitive fibers using an Ultraviolet (UV) laser source. The thermal sustainability of Type I FBG is the lowest in comparison with the other types. These types of sensors that are manufactured using highly photosensitive Boron/Germanium fibre can withstand temperatures of up to 400 °C. The thermal stability is strongly related to the fibre composition. Considering Antimony or Tin doped optical fibres, the fibre can withstand temperatures as high as 900 °C [130].

b) Type IIA FBGs

By longer exposure of Type I FBG to the UV light from a laser source, a Type IIA FBG is formed which has similar characteristics such as temperature and strain sensitivity as a Type I FBG. In this process, Type I grating is partially erased before the formation of the Type IIA FBG. In this case the temperature stability is significantly improved and this type of grating has a broader bandwidth. Their superiority in terms of the thermal stability gives them a great advantage to be used in high temperature environments [130].

c) Type II FBGs

This type of FBGs is inscribed on the optical fibre using an intense laser pulse which causes physical damage in the fibre structure and results in a large refractive index change in very small localised regions at the core and cladding boundary. This makes Type II FBGs significantly different in comparison to the two previously described types. The grating manufactured in this way is thermally stable and it does not easily degrade at temperatures as high as 800 °C [130]. Li *et al* [147] have reported the thermal stability of a femtosecond laser pulse – induced type II-IR FBGs up to 1200 °C, showing that grating reflectivity and a resonant wavelength remained unchanged for 20 hours during isothermal measurements. The FBGs written in this way are clearly attractive for any kind of application where high temperatures are experienced. Canning *et al* have reported the use of regenerated fibre Bragg gratings in standard photosensitive boron codoped germanosilicate optical fibre for measurements in high temperature environment [148]. Regenerated FBGs are gratings that have grown through thermal processing at high temperatures of 900 °C after the FBG is written by use of UV light. The authors have proven that this kind of FBG can operate at 1295 °C without evidence of any

decay after a certain period of cycling. In the experiment reported, the optical fibre became brittle while FBG remained intact. Another approach that could be used to create high temperature stable gratings was reported by Warren-Smith *et al* [149], which is known as femtosecond laser ablation on pure silica suspended – core micro structured optical fibres. In this case sufficiently short pulses have been used and multiphoton absorption can lead to ionization of electrons and the physical removal of material. The simple geometry of fibre with three large holes is used and FBGs have been created and tested to survive as high temperatures as 1300 °C. Mihailov has reported that for temperatures above 1200 °C, silica based optical fibres are no longer suitable and the most successful optical fibre used for higher temperature sensing applications is the single crystal sapphire fibre that has a glass transition temperature of approximately 2000 °C [150].

3.5 Properties of Fibre Bragg Gratings

The main aim of this section is to give a brief overview of the main properties of uniform gratings which are used for this particular research. The Bragg resonance condition, reflectivity of uniform FBGs and their strain and temperature sensitivities are explained in this subsection.

3.5.1 Reflectivity of a Uniform Fibre Bragg grating

As illustrated in Figure 3.1, the light launched in the optical fibre is reflected by the series of grating planes. When the Bragg condition is met, the reflected light at each grating plane will be in phase with a back-reflected peak at a centre wavelength is called the Bragg wavelength. The first-order Bragg resonance can be defined as follows:

$$\lambda_B = 2n_{eff}\Lambda \quad (3.1)$$

where, λ_B is Bragg wavelength, n_{eff} is the effective refractive index of the fibre core and Λ is grating period.

The Bragg resonance condition is governed by two principles, i.e. energy and momentum conservation [151]. To achieve the energy conservation, the frequency of incident light should be the same as the frequency of the reflected light. Regarding the momentum conservation, the wavevector of the reflected wave must be equal to the sum of the incident wavevector and the grating wavevector as demonstrated in Fig. 3.1.

Considering the FBG produced by UV interference pattern irradiation the refractive index modulation has a sinusoidal nature and it could be expressed by the following equation [130]:

$$n(z) = n_0 + \Delta n \cos\left(\frac{2\pi z}{\Lambda}\right) \quad (3.2)$$

where, n_0 is the average refractive index of the fibre core, Δn is the amplitude of the induced refractive index change with its typical values ranging from $10^{-3} - 10^{-5}$ and z is the distance along the fibre. The reflectivity (R) of a Bragg grating with a constant amplitude of modulation and period as a function of the grating length (l) wavelength (λ) derived by Lam and Garside [152] is given by the following equation:

$$R(l, \lambda) = \frac{\Omega^2 \sinh^2(sl)}{\Delta k^2 \sinh^2(sl) + s^2 \cosh^2(sl)} \quad (3.3)$$

where, Δk is detuning wavevector which is equal to $k - \pi/\lambda$, k is the propagation constant equal to $2\pi n_0/\lambda$ and $s = (\Omega^2 - \Delta k^2)^{1/2}$ and Ω is the coupling coefficient for sinusoidal variation of the refractive index modulation of the fibre core given by the following expression:

$$\Omega = \frac{\pi \Delta n}{\lambda} \left(1 - \frac{1}{V^2}\right) \quad (3.4)$$

where, $1 - 1/V^2$ is the fraction of the fibre power mode confined in the fibre core and can be estimated using normalised frequency as follows:

$$V = \left(\frac{2\pi}{\lambda}\right) a \sqrt{n_{co}^2 - n_{cl}^2} \quad (3.5)$$

where, a is the radius of the fibre core, n_{co} and n_{cl} are refractive indices of the core and cladding respectively. At the Bragg resonance wavelength, the detuning wavevector, defined in Eq. 3.3 is equal to zero and this results in a simplified expression for the reflectivity and making it only dependent on the amplitude of the induced refractive index change and the length of grating.

$$R(l, \lambda) = \tanh^2(\Omega l) \quad (3.6)$$

3.5.2 Strain and Temperature Sensitivities of FBGs

As defined in Eq. 3.1, the Bragg wavelength of an FBG is determined by the effective refractive index of the fibre core and the period of the grating structure. The influence of these two parameters will induce the change in the Bragg wavelength ($\Delta\lambda_B$) and it can be expressed by the following equation:

$$\Delta\lambda_B = 2n_{eff}\Delta\Lambda + 2\Lambda\Delta n_{eff} \quad (3.7)$$

Regarding the strain effect on the Bragg wavelength it is linked to the two main phenomena:

- 1) The grating period changes due to the physical deformation of the optical fibre
- 2) The effective refractive index changes, which is called the strain – optic effect

Similarly, temperature caused wavelength shift is linked to the thermal expansion of the fibre material and the thermo-optic effect [153]. Therefore when the FBG is subjected to the variation in strain and/or temperature, there is a spectral shift of the grating, confirming its intrinsic strain and temperature sensitivities. The typical strain and temperature sensitivities of a bare FBG, at around 1550nm, are approximately 1.2 pm/ $\mu\epsilon$ and 10 pm/ $^{\circ}\text{C}$.

3.6 FBG multiplexing schemes

One of the main advantages of FBG-based optical fibre sensors is their ease of multiplexing and this makes them superior over their conventional electrical counterparts. Three widely reported multiplexing schemes used over time are wavelength division multiplexing (WDM), time division multiplexing (TDM) and frequency division multiplexing (FDM). The multiplexing schemes mentioned above, can be either used as an individual technique, or a combination of two of them with the main aim to considerably increase the number of multiplexed sensors per optical fibre [154]. In addition to this spatial division multiplexing (SDM) is briefly explained in this section, which is often used in combination with WDM.

3.6.1 Time division multiplexing (TDM)

Time division multiplexing is based on the ability to separate the responses from one sensor to another in time. The basic principle of TDM sensor multiplexing is schematically represented in Fig. 3.10 where a broadband light source is used to interrogate an array of identical FBG sensors separated by a distance that allows the time discrimination of each sensor. When light from the source $F(\lambda)$ passes through identical sensors $S_i(\lambda, \lambda_B)$ the transmitted spectrum $T_i(\lambda)$ is disturbed and consequently the reflected spectrum $g_{i+1}(\lambda, \lambda_B)$, generated by interrogation of the sensor $S_{i+1}(\lambda, \lambda_B)$.

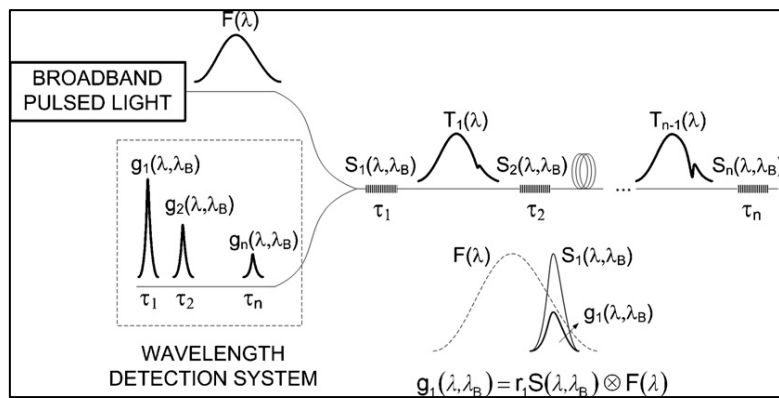


Figure 3.10 Schematic of TDM multiplexing [154].

Carlos *et al* [154] reported that using this approach, the number of sensors in an array is limited by the attenuation of the reflection signals. It is demonstrated that reflection signal of sensor n decreases with the number of sensors, which indicates the limitation of the number of sensors in the system which to some extent could be overcome by increasing the power of the light source or combining a TDM scheme with WDM. Another issue with TDM multiplexing is the necessity to ensure that sensors must be placed sufficiently far apart due to the fact that a pulse returning from the adjacent sensors must be able to be detected separately.

3.6.2 Wavelength division multiplexing (WDM)

Conventional wavelength division multiplexing technique is based on an array of FBGs where each FBG sensor occupies a unique spectral region. The number of sensors within the network is limited by the bandwidth of the light source and the range of measurement that is required for a particular application. For example, if the light source has a bandwidth of 50 nm and each sensor is required to measure strain in the range from $-1500 \mu\epsilon$ to $1500 \mu\epsilon$, the corresponding range of each Bragg wavelength shift is approximately $\pm 1.5\text{nm}$, considering a typical sensitivity of an FBG sensor of $1 \text{ pm}/\mu\epsilon$. In such a sensor system, the maximum number of sensors would be 16. An example of a WDM FBG multiplexing scheme is given by Childs [155] and is shown in Fig. 3.11.

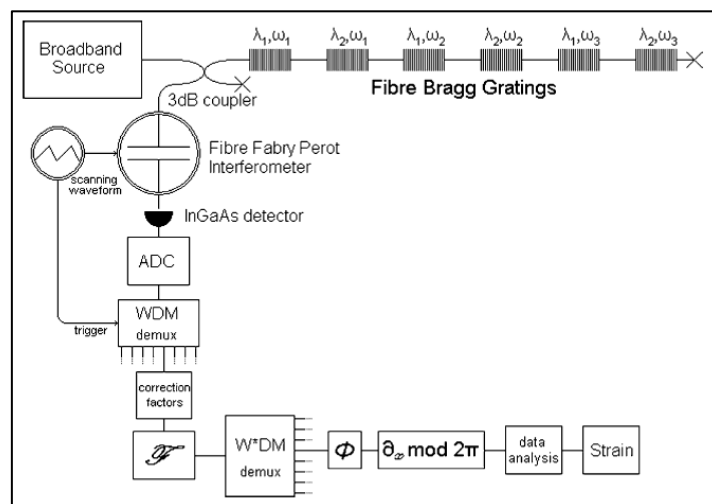


Figure 3.11 Architecture of FBG based strain system [155].

It is noticeable that a WDM scheme on its own demand a broad source bandwidth in order to accommodate a restricted sensor dynamic range. In order to extend the network of FBG sensors, there are various techniques available. The most common approach is to use a combination of WDM and TDM due to the simplicity of implementation [154]. The TDM/WDM topology is able to address a large number of FBG sensors. However, this type of

implementation is limited by the scanning frequency, which limits the response of the system to dynamic signals and transients. Implementing TDM in the system also limits the spacing between FBGs as well.

A recent advance in terms of extending the range of WDM technique was reported by Ou *et al* [156] where WDM was combined with so called frequency shifted interferometry (FSI) which has attracted a considerable attention. FSI is based on use of a continuous wave laser, thus neither a pulsed source nor high-speed detection is required. Furthermore, FSI utilises a differential detection technique to remove the DC component of noise, and consequently it has a high SNR and avoids the need for optical amplifiers. The combination of the WDM with the FSI technique has been reported where an ultra-weak FBG sensor array consisting of 121 WDM-based units, each containing 3 weak FBGs with different wavelength has been investigated. The schematic diagram is shown in Fig. 3.12.

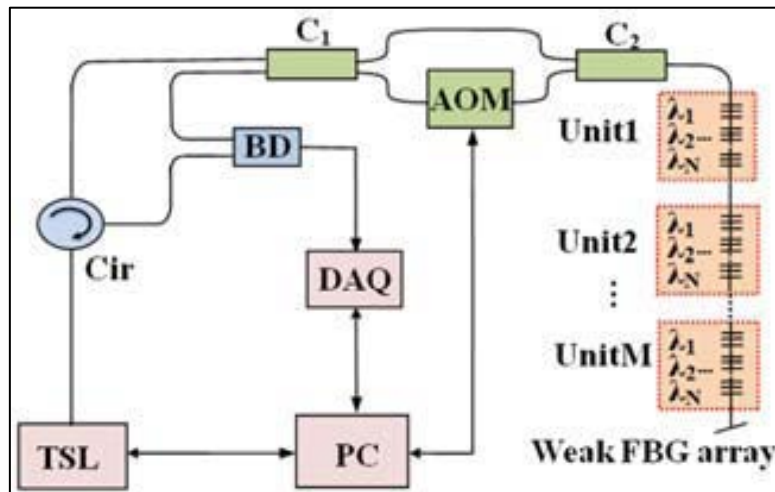


Figure 3.12 Schematic diagram of combination of FSI and WDM [156].

The operation of FSI is equivalent to that of the Sagnac interferometer, which is reported in Chapter 2. The only difference is that, FSI utilises an acousto - optic modulator (AOM) which is shown in Fig. 3.12. As each FBG serves as a reflection site, the interrogation system is essentially a combination of N – by – M sagnac interferometers. This approach can be easily expanded by increasing the number of wavelength channels and in that case there is a clear indication that this could be used as a large-scale sensing network.

3.6.3 Frequency division multiplexing (FDM)

Chen *et al* [157] have reported use FBG multiplexing scheme based on a frequency modulated continuous wave (FMCW) approach. In this case, a triangular frequency sweeping is assured. The difference between the triangular frequency-swept reference waveform and a delayed

version of the reference produces a beat frequency. The beat frequency can be defined as a product of the frequency excursion and the time delay difference between the two waves. The experimental setup and implementation of the FDM scheme based on the FMCW technique is given in Fig. 3.13.

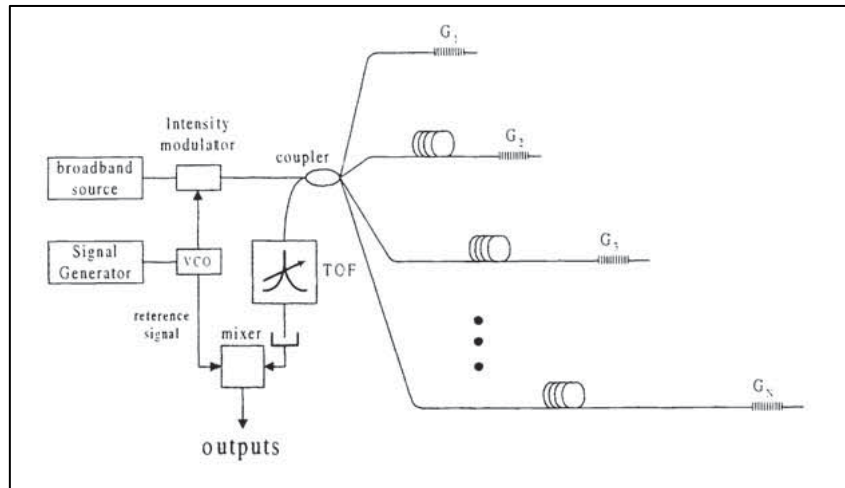


Figure 3.13 Schematic diagram of FMCW multiplexed FBG sensor array in parallel topology [157].

The light from a broadband light source is modulated with the triangular swept frequency carrier generated from a voltage controlled oscillator (VCO) and launched into the FBG sensor array. The reflections from the FBGs are guided back to a tunable optical filter (TOF), then a photo – detector, prior to mixing with reference signal from the VCO subsequently. The system output consists of a number of beat notes and beat frequencies determined by the delay differences between FBG sensor signals and the reference signal. The Bragg wavelength of the individual FBGs can be interrogated by scanning the TOF and recording the control voltage of the TOF that corresponds to the peak of the different frequency components.

Apart from the continuous wave approach, a stepped frequency method with a microwave vector network analyser (VNA) could also be realised. In this case the intensity is modulated with a microwave frequency up to the GHz range and reflected light is directly detected and converted back to the electrical domain for demodulation. The methods using this approach belong to so the called incoherent optical frequency domain reflectometry (IOFDR) to distinguish them from optical time domain reflectometry (OTDR) where a swept laser and interferometric detection is used instead. Werzinger *et al* [158] have demonstrated use of the IOFDR method based on stepped frequency. Using a continuous modulation of the light intensity directly maximizes the signal power received from the fibre. The experimental setup demonstrated by Werzinger *et al* is shown in Fig. 3.14.

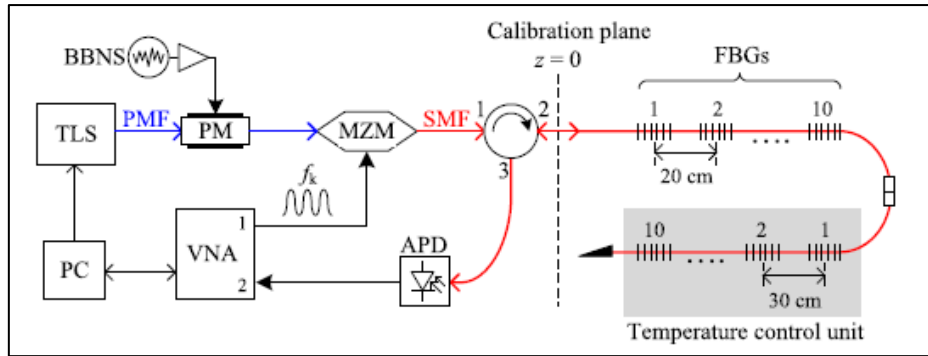


Figure 3.14 IOFDR measurement setup for a quasi – distributed temperature measurement using FBG sensors [158].

The tunable light source indicated in Fig. 3.14 performs a step wavelength scan over the spectral window of the FBGs in steps of 10 pm. A phase modulator (PM) driven by electrical broadband noise source (BBNS) is used to further broaden the laser line width. The laser intensity is modulated with the harmonic frequency stimulus of the VNA with a Mach-Zehnder modulator (MZM). Considering that inputs of the PM and MZM are polarisation dependant, polarisation maintaining fibre (PMF) is used in these sections. Identical FBGs are used and separated by 20 cm, where the first 10 FBGs were settled at room temperature and the second 10 FBGs were embedded in a temperature control unit with thermoelectric coolers (TEC). The light reflected from FBGs is detected by the APD receiver and converted to the electrical domain. The demodulation of the VNA used in this technique is advantageous over TDM as the spatial resolution has been improved to the centimetre range and this setup has the potential to reach more than 50 FBGs at a 30 cm spacing at a rate of 50 s/nm.

Another recent approach, developed by National Aeronautics and Space Administration (NASA) and so called Fiber Optic Sensing System (FOSS) is based on a combination of WDM and OFDR technology. FOSS uses FBG sensors and a combination of OFDR for high spatial resolution and WDM for high acquisition speed, together with an interferometer technique that can simultaneously interrogate thousands of FBG sensors in a single optical fibre. In order to achieve a high spatial resolution and have the ability to interrogate a large number of FBGs in a single fibre, the OFDR method is used. A typical OFDR system interprets a beat frequency between a reference arm and the sensing arm. In this case an interference signal is generated and the phase difference generated by the interferometer is detected by the photodetector. In the case of the FOSS, the same interference effect is applied to FBGs used as strain sensors as shown in Fig. 3.15.

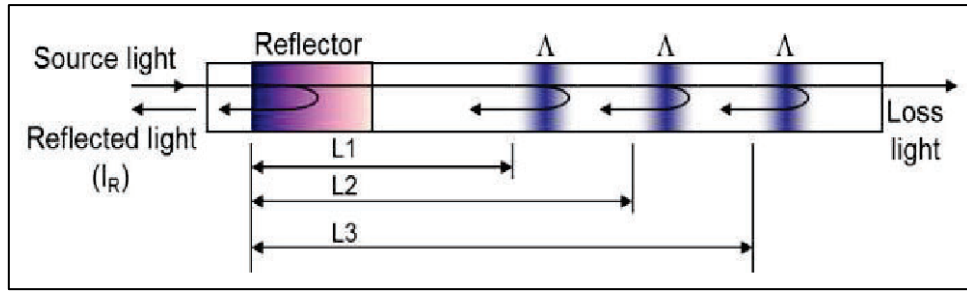


Figure 3.15 FBG sensors as part of FOSS [159].

In this application the distance between each sensor and the reflector can be individually determined first through sampling of the output intensity while continuously sweeping the laser's wavelength. The output signal is a summation of the complete set of gratings located along the fibre length and is given by the following equation:

$$I_R = \sum_i R_i \cos(k2n_0 L_i) \quad (3.8)$$

where, R_i is a reflection spectrum of i^{th} grating, n_0 is effective refractive index, L is the path difference and k is the wavenumber. Each grating is modulated with its unique frequency, determined by the grating's unique position on the optical fibre. Applying a Fourier transform to the intensity information obtained from the wavelength sweep range, this information is mapped from wavelength domain to spatial domain. Considering the linearity of each FBG wavelength shift, each grating wavelength can be determined by taking an inverse FFT (IFFT) from the spatial domain back to the wavelength domain. Chan *et al* have reported the use of FOSS technology where 8 fibres have been used to interrogate 16,000 FBGs in one system [159]. The system is used for flight applications with a maximum sampling rate of 100 Hz.

3.6.4 Spatial division multiplexing (SDM)

The main concept behind spatial division multiplexing is the use of optical switches between different channels, which could include one or several multiplexing schemes combined. Using this methodology, for each time of the measurement, only one channel will be chosen. The schematic diagram of spatial division multiplexing is demonstrated in Fig. 3.16 [160].

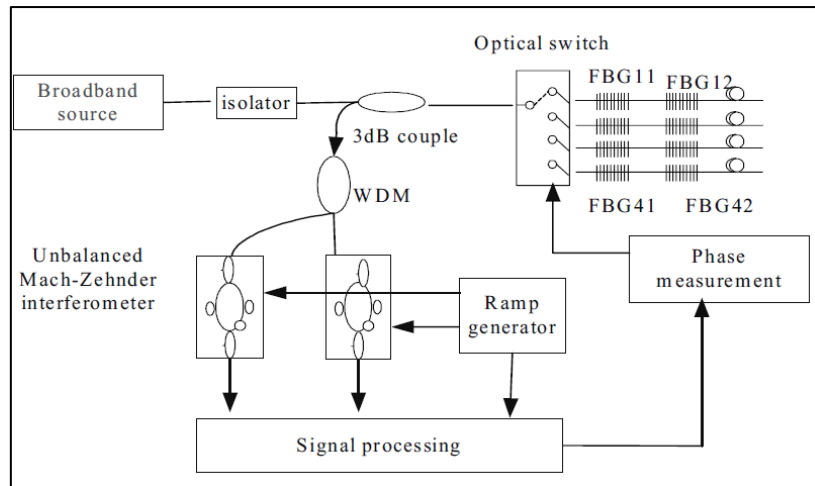


Figure 3.16 Schematic diagram of SDM scheme [160].

The broadband light source enters the optical switch via coupler and the optical switches are used to control the choice of the optical path, using the signal controlling circuit. The major issue with mechanical switches is their limited lifetime.

3.7 Applications of FBG sensors as an important NDT technique

Various research institutions and commercial enterprises have been actively involved in the development of FBG sensors that could be applied as non-destructive testing methods. With the availability of commercial interrogation systems as well as commercial FBG sensors, there is a notable increase of FBG sensing systems applied in various industries such as aerospace, marine, transportation, oil and gas, etc. [6].

There are various factors that can cause structural degradation, such as corrosion, fatigue, overloading, etc. and these factors can lead to the failure of these structures with potential severe consequences. Therefore monitoring the ‘health’ of these structures plays an important role in preventing such catastrophic failures.

Fibre Bragg gratings provide an effective solution by offering the capability for multi-point and multi-parameter measurement for certain structures that are under examination. This subsection is divided into several parts discussing the applications in SHM where FBG sensors have been successfully applied.

3.7.1 Strain and loading monitoring

One of the most important applications of Bragg grating based optical sensors is the measurement of static, quasi-static or dynamic loading on structures. Considering the loading

and the strain measurement using FBG based sensors, one of the main applications is related to the real time monitoring of bridges and other civil structures.

The work reported by Kerrouche *et al* [161] is related to the technique of mounting the sensor system on the bridge in a previously made groove in the concrete surface. In this case carbon fibre reinforcement polymer (CFRP) integrated with FBG arrays is placed inside the groove and then epoxy applied as shown in Figure 3.17 (a). In addition to it, the CFRP tube integrated with FBGs has also been tested as well as shown in Figure 3.17 (b). The instrumentation and measurement were conducted on a 60 – year old bridge in Sweden with positive results having been obtained. Two FBGs have been marked in Fig. 3.17, however the overall number of sensors per rod or tube was 7.

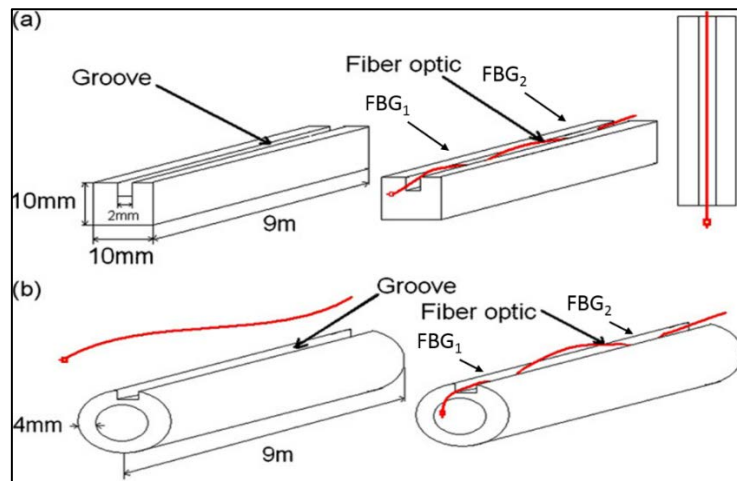


Figure 3.17 Schematic illustration of a sensor protection system using CFRP material (a) FBG installation inside rod (b) CFRP tube with integrated FBGs [161].

Rodrigues *et al* [162] reported the FBG sensors protection and installation during the construction phase of the bridges into which they were embedded. In this case, the developed transducer consists of a steel bar of 16 mm diameter and 1.0 m long with a helicoidal groove on both sides and anchorage at each extremity. Two FBG sensors were aligned along the long axes with the bar and glued diametrically opposite bar fibres at a central position as shown in the Fig. 3.18.

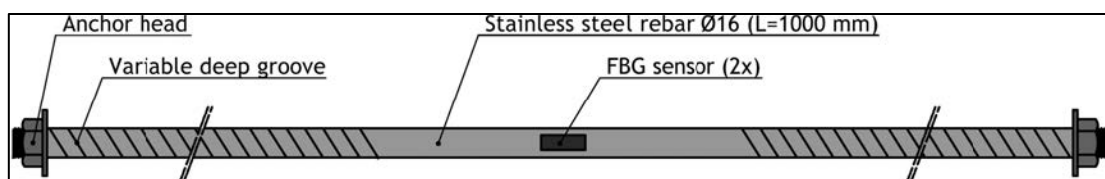


Figure 3.18 Schematic representation of the optical based strain transducer to be embedded into concrete [162].

In this work around 92 sensors have been installed in the Leziria Bridge over Tagus River and provided strain information at the bottom and top slab of the bridge.

The other solution reported is to produce ‘weldable’ FBG sensors. Bosia *et al* [163], reported such a technology as shown in Fig. 3.19 where the sensors were protected by a capillary stainless steel tube glued with thermal curing epoxy. The tube was then laser welded to a thin stainless steel base that was used for direct spot welding to the steel structure.



Figure 3.19 Fibre Bragg grating weldable strain sensor [163].

Such welded sensors have been installed and evaluated on a pedestrian steel bridge over Sao Roque and Botiroes channels in Aveiro, Portugal. Derkevorkian *et al* [164] have instrumented a cantilever swept wing plate with 300 FBG sensors using 3 fibres. The FBG sensors were placed on the top and bottom surface of the plate as shown in the Fig. 3.20.

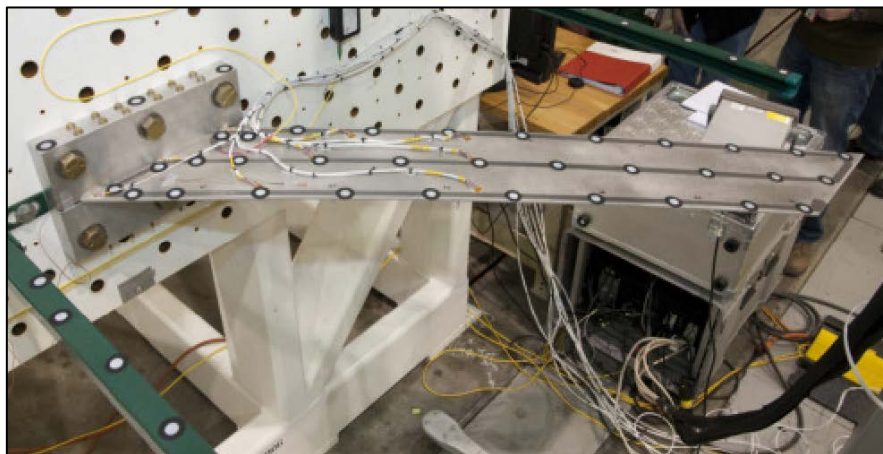


Figure 3.20 Unloaded swept plate instrumented with 300 FBG sensors, where the sensor locations are represented by white circles [164].

The plate was loaded using several cases, only the trailing edge, uniform loading and only on one point at the plate tip. A finite element (FE) model was developed to represent the plate and

various loading conditions considered in this case. In order to estimate deflection shape of the plate, an algorithm was developed based on the use of measured strain data by FBGs. The algorithm relies on the classical beam theory to derive the displacement transfer functions in segments of the structure and more details can be found in [164].

The measurement of strain transfer between reinforcement and concrete is the key factor for forecasting the incipient failure of these strengthened structures since the knowledge of the strain on the surface might not be sufficient in most cases, such as the stress limit in the concrete or approaching the reinforcement limit. Montanini *et al* [165] addressed this problem by evaluating strain sharing in strengthened concrete beams by embedding FBG sensors into both the concrete tensioned surface and into woven fibre reinforcements. In this case the strengthening system consisted of a fiber reinforced cementitious matrix (FRCM) with a polyparaphenylene benzobisoxazole (PBO) bidirectional mesh woven. The PBO fabric was instrumented with two FBG sensors, intended to measure the longitudinal strain and temperature variation, and they are respectively marked as FBG_{ϵ} and FBG_T in Fig. 3.21.

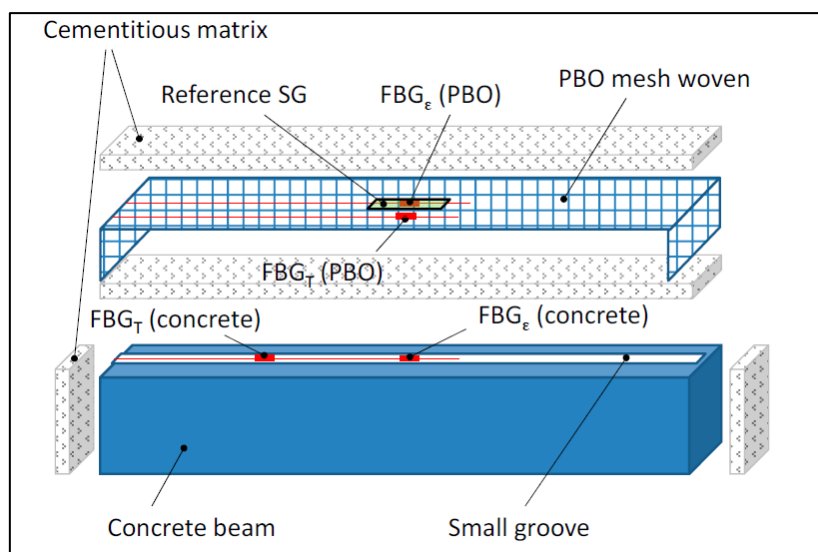


Figure 3.21 Schematic drawing of instrumented FRCM strengthened beam with embedded FBGs [165].

A traditional electrical strain gauge (SG), having a similar length comparable to that of the Bragg gratings was also glued to the textile in order to provide reference data. This gauge was placed on the opposite side of the FBG_{ϵ} .

Sevillano *et al* [166] reported use of FBG sensors for two sets of reinforced beams when the beams were subjected to four-point loading. The geometric dimensions and the reinforcement

layout in the transversal sections, which were common for both beams, are illustrated in Fig. 3.22.

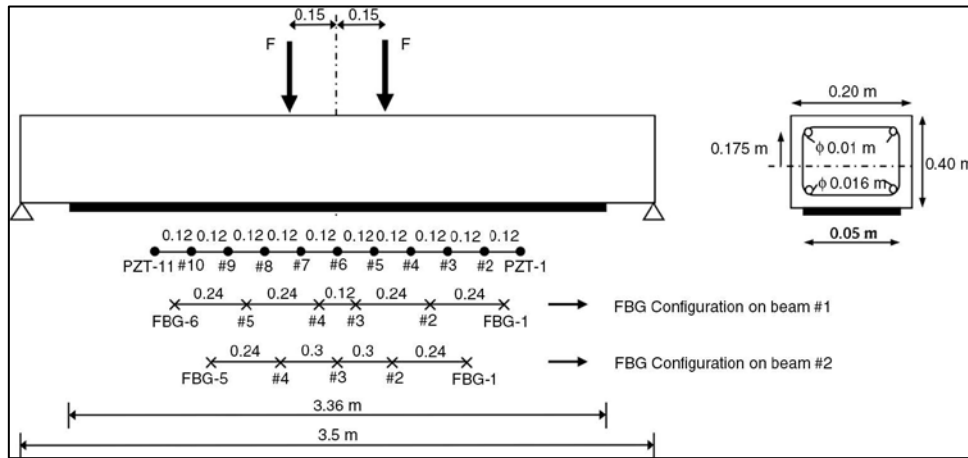


Figure 3.22 Schematic representing geometry, loading scheme and sensor layout on both beams [166].

In each test performed, the beam was subject to a series of increasing quasi-static loading with the purpose of gradually generating cracks into the specimen that are captured using PZT sensors.

Some of the most recent applications and the sensing principles for strain and load monitoring have been summarized in this subsection. A more comprehensive review of stain and load measurement for SHM using FBG sensors is given by Di Sante [167] and Wing *et al* [168].

3.7.2 Corrosion monitoring

One of the main causes of concrete structural degradation is the reinforcement bar corrosion and its estimated cost for repair, maintenance and rehabilitation is around US\$100 billion per year globally [169]. The occurrence and propagation of reinforcement corrosion deteriorate the usability and safety of the various structures. Great examples include bridges that are used in a chloride environment for a long period of time where the volume expansion caused by the corrosion of reinforcement can lead to concrete cracks. Considering these facts, monitoring a reinforcement bar corrosion is important to ensure the safety of reinforced concrete structures.

In order to ensure that the FBG sensor remains functional and intact after being embedded in concrete, Mao *et al* [169] proposed following packaging method shown in the Fig. 3.23. The Bragg grating was encapsulated in epoxy resin in order to prevent breaking of the fibre. The strain concrete corrosion monitoring (CCM) sensors are marked as CCM-FBG (S). The sensor was fixed using a tiny amount of epoxy ensuring accurate structural strain transfer. The

temperature FBG, marked as CCM-FBG (T) was kept in a relaxed strain-decoupled state in a thin tube so the sensor is free from structural strain.

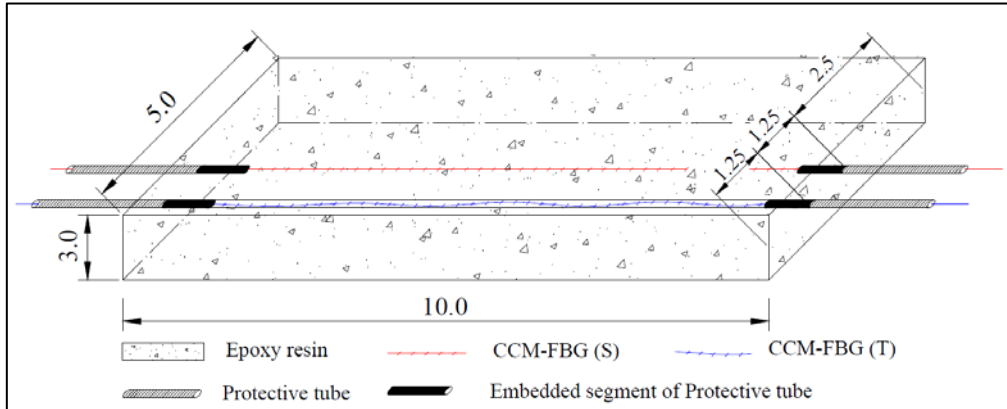


Figure 3.23 Schematic diagram of packaging procedure of concrete corrosion FBG sensor [169].

Corrosion monitoring FBG sensors have been embedded in the concrete structure and corrosion was accelerated using a DC power supply connected to the reinforcement. The schematic diagram of embedded reinforcement with the sensors around its circumference is shown in Fig. 3.24.

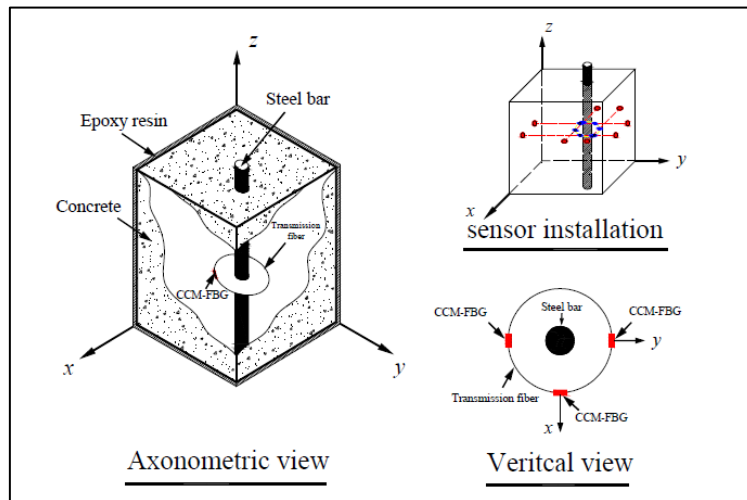


Figure 3.24 Corrosion monitoring FBG sensors layout [169].

Deng *et al* [170] reported a method for corrosion and crack monitoring on thermal sprayed metallic coatings. In order to protect the sensors in this environment, the bare FBG sensor was packaged using steel hypodermic tube and attached to the surface of the steel substrate using adhesives before embedment inside the thermal spraying coatings. The sensors were tested in a very harsh environment generated by using the High Velocity Oxygen Fuel (HVOF) thermal spraying in order to generate high velocity gas resulting from the combustion of a mixture of

oxygen and fuel gas. The sensors embedded on the top parts of steel plates are shown in Fig. 3.25.

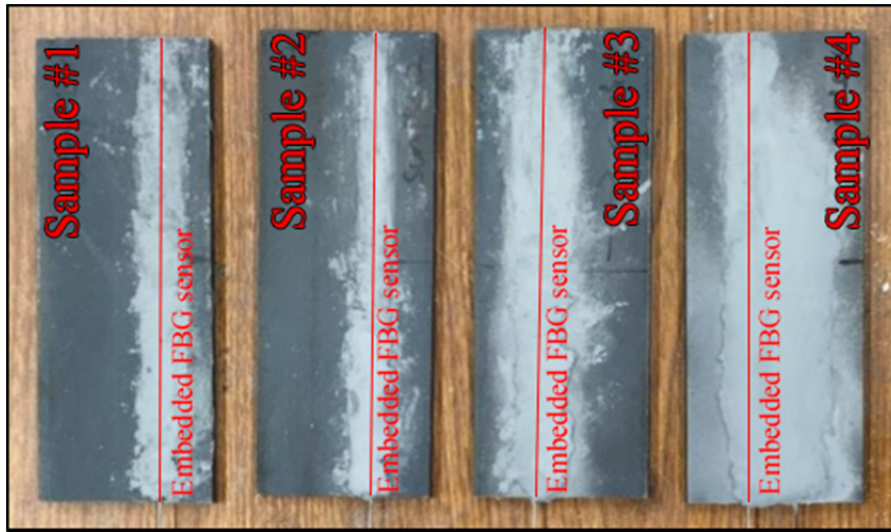


Figure 3.25 Layout of FBG sensors embedded in steel plates [170].

Accelerated corrosion tests based on electrochemical reaction were undertaken with FBGs being able to provide positive responses in terms of measuring corrosion status, corrosion rate of materials and crack propagation.

Ren *et al* [171] reported the use of FBG-based technique for pipeline corrosion detection. Considering the importance of the transportation of oil and gas and the issue that corrosion directly affects the thickness of the pipeline walls, it is necessary to monitor these pipes in real time to avoid disastrous outcomes. In their research, the corrosion is measured around the pipe by using so called ‘hoop-strain’ FBG sensors system. The schematic of the sensor layout is shown in Fig. 3.26.

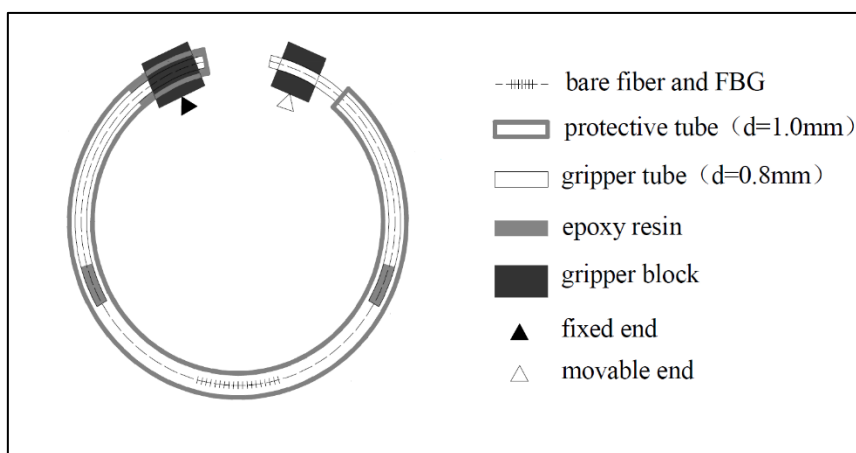


Figure 3.26 Schematic diagram of FBG hoop – strain sensor for corrosion detection on oil and gas pipes [171].

The FBG hoop-sensors reported in this work were mounted on the surface of pipeline models using super glue. In order to provide pressurised conditions to the pipeline models, an air pump was used for the experimental purpose. The internal pressure was measured by commercially available pressure sensors which were located inside the pipe.

Tan *et al* [172] reported another technique of protecting FBG sensors used for early corrosion detection. Two different sets of sensors have been used, one with etched FBG without any coating and another set with etched FBG which was coated by a soft, flexible and transparent PolydimethylSiloxane (PDMS) layer. Both FBGs were embedded on the rebar for corrosion monitoring. The rebars tested were subjected to an increased rate of corrosion in the hot and humid weather of Asia, in particular coastal areas. The following figure shows the protected FBG using PDMS.

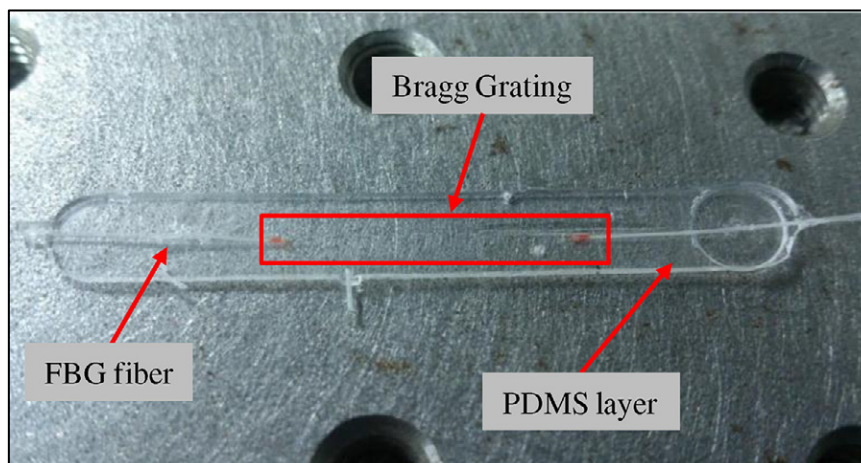


Figure 3.27 FBG sensor protection using PDMS layer [172].

The main idea of using protection is due to the nature of the environment and the risk that the bare FBG sensor could be easily broken. The disadvantage of PDMS coating for this application is related to the absorption of chemicals from the curing concrete which reduces its effectiveness in sensing the corrosion signal.

Concrete expansion and cracking are one of the most significant physical features related to concrete deterioration due to reinforcement corrosion, and thus monitoring these two phenomena is critical in order to evaluate the safe performance of reinforced concrete structures. These two features can be detected using AE techniques using fibre optic sensors. AE is comprised of high frequency elastic waves or stress waves generated when there is a rapid release of energy within certain materials that are experiencing deformation [173]. For example, in concrete structures, when corrosion is formed around steel reinforcement, pressure builds up in the surrounding concrete. When this pressure is high enough to break the interface

bonding, both micro-cracks and crack growth induces stress waves that could be captured by AE sensors installed on the surface of concrete. Apart from the use of FBG sensors and measurement of corrosion-induced strain, there are other techniques reported. Li *et al* [173], have reported a technique that uses AE technique and FBG strain sensors together to monitor progression of reinforcement expansion and concrete cracking due to reinforcement corrosion in concrete structures. Acoustic emission measurement use used to detect corrosion initiation and crack growth, while an FBG is used for measurement of the extent of corrosion and identification of time of cracking. On the other hand, Zhao *et al* have examined the feasibility of the Brillouin optical time domain analysis (BOTDA) distributed sensing technique for steel corrosion detection [174]. Mao *et al* have investigated a combination of BOTDA and FBG sensors for monitoring corrosion expansion cracking [175]. McColuma *et al* have designed and evaluated a novel corrosion sensor based on use of birefringent photonic crystal fibres for pressure/force measurement [176].

More applications and more comprehensive reviews of Bragg grating based techniques used for corrosion measurement can be found in the work reported by various authors [177-179].

3.7.3 Vibration and acceleration measurement

The detection and measurement of vibration and acceleration are crucial parameters for NDE testing in various industries such as, oil and gas, aerospace, marine industry, etc. Recently FBG based vibration sensors, have received more attention than their electrical counterparts [178].

There have been various types of vibration sensors proposed using various configurations in order to restrict sensing to one, two or three direction. Feng *et al* [180] recently reported 1D vibration sensors using a hybrid cantilever beam and pair of FBGs. The sensor were designed for the oil and gas industry and a schematic of the sensor is given in Fig. 3.28.

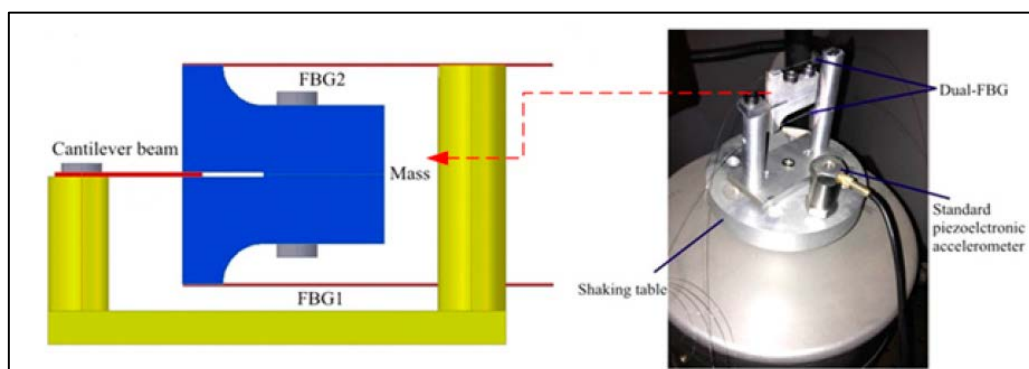


Figure 3.28 Schematic structure of proposed accelerometer and instrumentation of the pipe for oil and gas industry [180].

The elastic rectangular cantilever beam is used as a moving part. The cantilever beam is made of spring steel and it supports a mass block formed by bolting two aluminium blocks back to back. Two FBGs, marked as FBG1 and FBG2 were pre-stressed and mounted on the upper and lower surfaces of the mass block, respectively. By exciting the block and ensuring its movements up and down, compression and stretching of FBG1 and FB2 occurred which is used for vibration measurement. The resonant frequency of the sensor is mainly dependent on the mass of the aluminium blocks and the characteristics of the cantilever beam. Another example of an accelerometer, based on the copper diaphragm structure was reported by Liu *et al* [181] and applied in seismic applications. In this case, a cylindrical mass is sandwiched between two horizontal diaphragms mounted inside a vertical cylindrical shell as demonstrated in the Fig. 3.29.

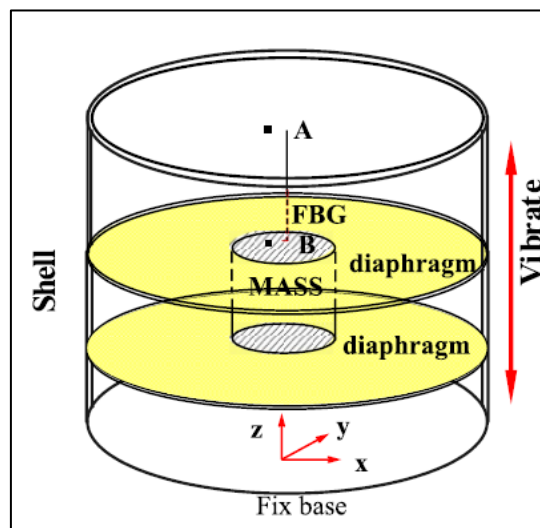


Figure 3.29 Schematic structure FBG accelerometer based on double diaphragms reported by Liu *et al* [181].

An FBG was pre-tensioned and attached to the fixed upper cover plate and the mass block, at points A and B respectively. When the mass moves in the vertical directions along the z axis, the sensitivity and frequency response of this accelerometer design depends on the inertial mass, the ratio of the mass radius to diaphragm radius and Young's modulus of the diaphragms. In the case reported by Liu *et al*, the resonant frequency was above 1200 Hz, due to the dual – diaphragm – shaped structure and large Young's modulus of the diaphragm. Zhang *et al* [182] reported an FBG based vibration sensor with a resonant frequency of 2 kHz consisting of a mass resting on a layer of compliant material supported by a rigid base plate. The material used for the cylinder was a two-component vulcanized silicon rubber which is suitable for seismic

applications and higher temperatures. The experimental results indicated that the sensor shows excellent performance with a flat frequency range from 30 to 300 Hz.

An interesting approach reported by Qiao *et al* [178] is based on writing FBG sensors in the cladding of the short piece of so called ‘thin-core’ fibre (TCF) which was spliced to a standard single – mode fibre (SMF) as shown in the Fig. 3.30.

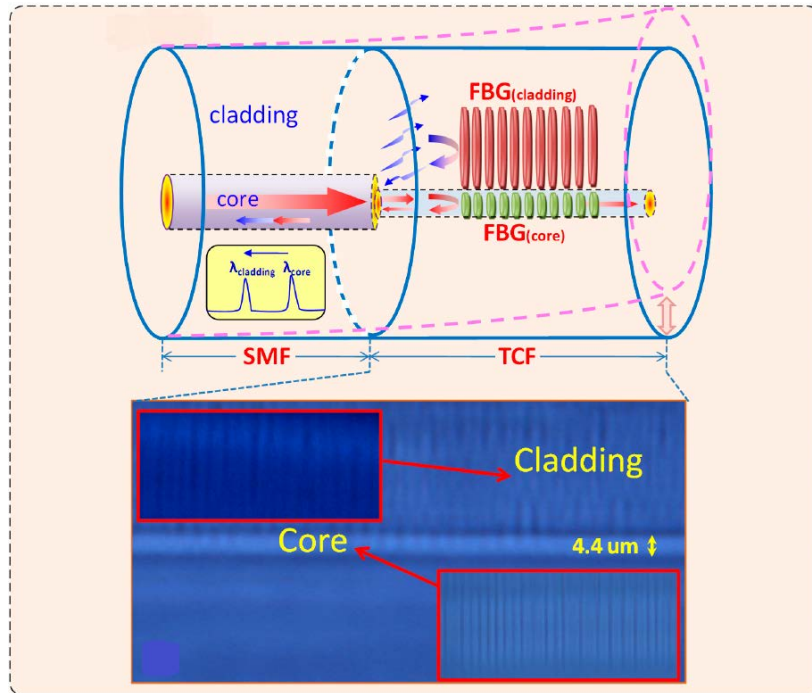


Figure 3.30 Schematic structure of TCF-FBG accelerometer [178].

In this case, a femtosecond laser was used in order to manufacture the FBG in the cladding of a TCF. With this configuration, two resonances in reflection have been achieved which originates from the gratings in the core and the cladding, respectively shown as FBG core and FBG cladding in Fig. 3.30. The cladding Bragg resonance peak was located 8.8 nm away from the core resonance and it strongly reacts to the small fibre bending. This cladding resonance corresponds to the mode coupling from the core of the input SMF to the cladding of the TCF. This mode which is partially attenuated by the splicing point is coupled in the core of SMF and returned to the interrogation unit. This mode in TCF-FBG demonstrated a clear polarisation dependence because of the asymmetrical distribution of the cladding of the FBG along the fibre cross section. The fundamental mode resonances were unaffected by bending and hence could be used for temperature measurement. The disadvantage of this technique is low intensity of the received signal in sensors as well as being easily affected by the surrounding RI since the grating is distributed over the fibre cladding.

A more comprehensive review of FBG based vibration measurement sensors with the broad range of applications as well as principles is given by Qiao *et al* [178].

3.7.4 Acoustic Wave measurement

Acoustic wave detection has attracted the attention of many researchers due to the importance of the topic in various industries, such as aerospace, oil and gas, marine, seismic measurement, etc. Considering the technical challenges that these industries are facing, ultrasonic wave detection became one of the most critical methods for non – destructive testing [183]. Acoustic wave detection has been traditionally performed using current – driven PZTs. However, these transducers, reported in Chapter 2, have some inherent drawbacks which are summarized and cross-compared with optical fibre sensors in Table 3.1.

Table 3.1. Comparison between PZT and FBG ultrasonic sensors [178].

PZT	FBG
Narrow detection bandwidth	Broadband response
Large size	Small size, light weight, flexible
Sensitive to EMI	Immunity to EMI
Poor stability of signal transmission (~ 10m)	Stable long distance transmission
Poor multiplexing	Good multiplexing and multichannel detection
No direction recognition	Vectorial sensing

Considering the types of FBG sensors and various designs, the most common types of FBG sensors used for ultrasound detection are phase shifted (PS) FBG, FBG – FP cavities and uniform FBGs. As the main focus of this work is to develop and evaluate an acoustic emission detection system using uniform, FBG, the techniques covered by this review are focused on that technique.

There are a number of researchers who have experimentally evaluated the difference in sensitivity of FBG sensors which are glued to the structure in a conventional way for strain measurement and the FBGs that are ‘strain-free’ where the fibre has been bonded to the structure and a guided wave is detected by the FBG which is not physically bonded to the structure under investigation. Tsuda *et al* [184] reported the test on an aluminium plate using three FBG sensors bonded in a different way on to the specimen for ultrasound propagation detection. Two different transducers were used to excite the plate with longitudinal and shear

waves. The experiment consisted of testing a so called mobile FBG sensor, where the FBG was glued to an acrylic plate which is bonded to the structure, ‘strain-free’ FBG sensor as well as an FBG bonded in a conventional way, as shown in Fig. 3.31.

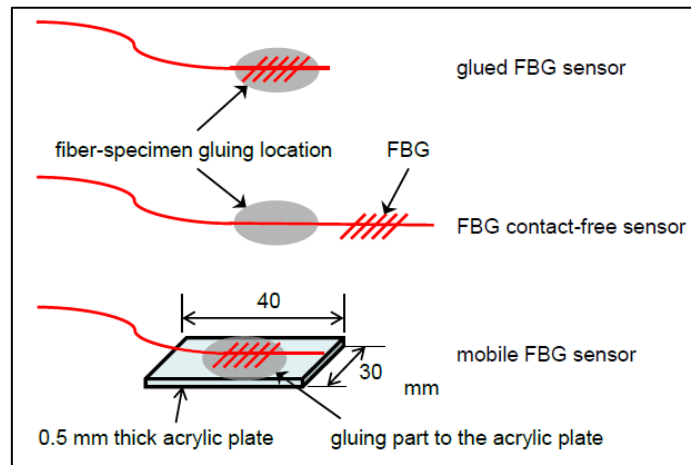


Figure 3.31 Schematic illustration of the FBG sensors employed in the experiment [184].

The outcome of this study proved that ‘strain – free’ sensors have a much larger sensitivity to the acoustic wave detection compared to the two other types of FBGs. However, it also has higher noise levels due to susceptibility to external disturbance. Also, the solution based on a ‘strain – free’ sensor is impractical for real life applications.

Wee *et al* [185] recently demonstrated that a ‘strain – free’ FBG has much higher signal to noise ratio (SNR) in comparison to the conventionally mounted FBG. In their test, an aluminium metal plate was excited using 3 single-burst at 300 kHz for several locations and the FBGs were located at a distance of 254 mm away from the transducer. The main conclusion of this was to establish that ‘strain-free’ sensor has much better SNR comparing to traditionally mounted sensors. However, this technique wouldn’t be suitable for my work due to impracticality of above mentioned method.

Tsuda *et al* [186] evaluated the relationship between the grating length and the ultrasonic detection sensitivity. An analytical study reported that the grating length of the FBG must be shorter than the wavelength of the ultrasound signal in order to detect the signal. If the grating length is longer than the ultrasonic wavelength, the strain within the grating length changes from tensile to compression and is practically insensitive to the ultrasonic wave. The results obtained from 2 different lengths of FBGs, i.e. 1 mm and 12 mm, representing respectively shorter and longer lengths with reference to the ultrasonic wavelength, are shown in Fig. 3.32.

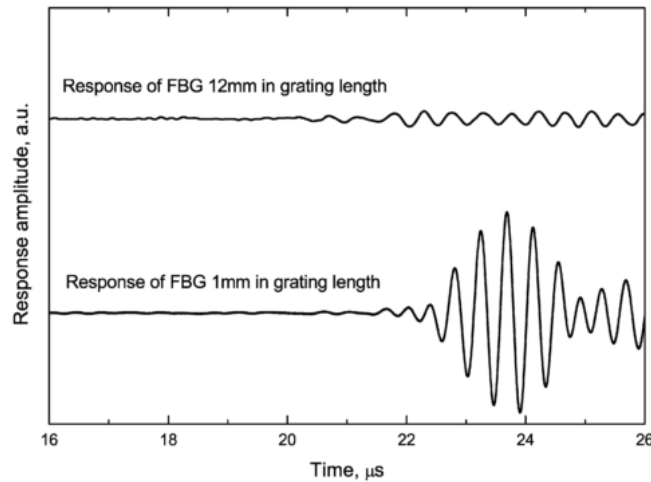


Figure 3.32 Ultrasonic responses of FBG sensors with different grating length [186].

The results obtained have demonstrated that SNR of response detected with 1 mm and 12 mm long FBGs are significantly different. This work could be relevant for my work in terms of improvements of SNR ratio and this could be used as one of the methods for the next stage of testing.

Moccia *et al* [187] reported the use of two different coatings for FBG sensors in order to detect an acoustic wave under water on a metal structure. A polyurethane resin and epoxy adhesive resin were both characterised in the experimental work. Sine wave pulses with duration of 0.5 ms at increasing frequencies in the range from 4 to 30 kHz in steps of 1 kHz, were used to generate an acoustic wave under water. Different thicknesses of coatings have been tested and it is proven that the thicker coating is beneficial for improvement of low-frequency background sensitivity, but detrimental in the high frequency region. In connection with the coating elastic properties, low values of Young's modulus, Poisson's ration and density are desirable for enhancing the sensitivity.

Takeda *et al* [188] reported the detection of acoustic waves using embedded FBG sensors inside a CFRP structure. The sensors were polyimide coated and tailored for Lamb waves detection. In this work, it was verified that the grating length should be shorter than 1/7 of the ultrasonic wavelength. The directional sensitivity of FBG acoustic sensor has been confirmed by changing the location of the PZT in relation to the embedded FBG inside the CFRP structure.

Xia *et al* [189] tested the sensitivity of FBG based acoustic sensors to the side pencil-lead break, surface pencil-lead break and steel ball drops. The position of all the excitation sources and FBG sensor are shown in Fig. 3.33.

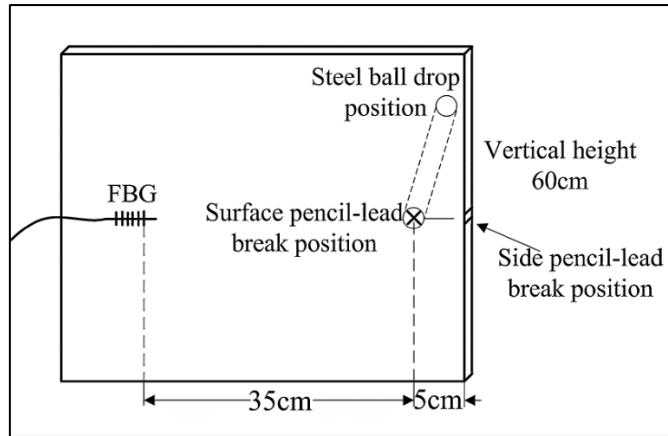
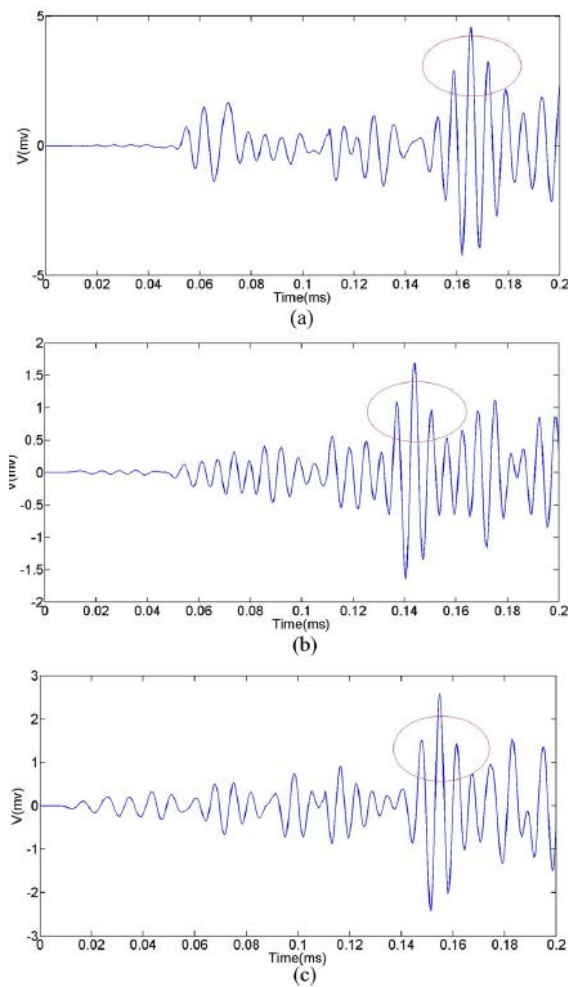


Figure 3.33 Schematic illustration of the excitation positions [189].

The demodulation system used in this case is based on the tuneable laser and the developed system was capable of detecting all three signals from the excitation sources. The results are shown in Fig. 3.34.



3.34 Waveforms detected in three different AE experiments a) surface pencil-lead break, b) side pencil-lead break, and c) steel ball drop [189].

As can be seen in Fig. 3.34, a Gaussian-sine the demodulation signal appears in all three waveforms. The maximum amplitudes of detected signal in the three cases were 4.577 mv, 1.696 mv and 3.517 mv, respectively, which is due to the different excitation amplitudes.

A more comprehensive review on acoustic wave detection using FBG sensors is given by Lin *et al* [190] and Yu *et al* [191] who have done extensive work in the field covering various types of FBG sensors for acoustic emission detection.

3.6 Summary

The chapter commenced with historical and theoretical development of FBGs, followed by their classification and inscription methods which have been widely reported. The discussions were focused on the Type I, uniform FBGs due to their wide applications in SHM. Compared to conventional NDE methods, FBGs offer a unique advantage due to their multiplexing capability and it has been shown that this allows thousands of FBGs to be integrated into a single length of fibre. A comprehensive review of multiplexing schemes and their latest developments were discussed in detail in this chapter. This was followed by a comprehensive review of existing FBG based sensing technologies for non-destructive testing and measurement of strain/loading, corrosion, vibration and acoustic waves.

Chapter 4

FBG-based Cascaded Acoustic Sensors for Marine Structural Condition Monitoring

4.1 Introduction

The main focus of this chapter is to report the work on the development and applications of FBG-based sensor system for acoustic emission detection and to discuss the potential alternatives to conventional PZT sensors, especially where they have shown limitations in use, such as in the marine sector. In marine industry, cavitation erosion has posed a key technical challenge to a variety of marine structures. A series of phenomena is considered to be the cause of cavitation erosion, which cause multi-million dollar damage to marine structures across the world annually. Effects such as bubble collapse and rebound, micro-jet formation and clouds of collapsing micro bubbles and cavitation vortices occur and cause the build-up of damage [4].

A cascaded optical acoustic sensor system based on the optical filter demodulation scheme, has been developed and its performance extensively evaluated. The FBG sensors used in the system, basically behave as FBG sensors for dynamic strain measurement.

The chapter begins with a review of demodulation schemes used and reported by other researchers when it comes to use of FBG sensors for dynamic strain measurement. This is followed by FBG sensors manufacturing process as well as sensors characterisation for this particular research.

The emphasis of the final part of this chapter is to present the experimental results obtained using the developed FBG based acoustic sensors system for both glass plate and metal plate tests conducted under water.

4.2 Principle of operation

The detection of acoustic emission (AE) is analogous to the measurement of dynamic strain, albeit at much higher frequencies. In order to detect very weak yet high frequency signals, two main interrogation methods have been reported [192]. The first is an edge filter detection method, which uses a spectrally-dependent filter to detect the shift in the sensing FBG spectrum, resulting in a change in intensity at the detector. The second is power detection method which is based on the detection of the FBG wavelength shift by using a spectrally-dependent light source. Both methods are explained in more detail in this subsection.

4.2.1 Edge Filter Detection Method

In the edge filter detection method, an FBG is illuminated by a broadband light source with a narrow band reflected optical signal from the FBG passing through an optical filter. The intensity of the optical signal transmitted through the optical filter varies with the acoustic pressure impinging on the FBG sensor. There are a number of filter schemes that have been used in the edge filter detection method and they are briefly explained below.

Figure 4.1 (a) shows the edge filter detection method based on the linear edge absorption filter in which an external filter is employed in the system. The FBG is selected in such a way that the Bragg wavelength is located at the 3dB point of the absorption filter transmittance [193]. The part of the light that is not transmitted to the detector is absorbed by the filter.

Figure 4.1 (b) shows the edge filter detection method using a matched FBG as an optical filter [194]. The matched FBG converts the spectral shift of the FBG into an intensity change. The main drawback of this technique is the difficulty in determining the nature of the strain, whether it is tensile or compressive, due to the symmetric nature of a FBG spectrum. In order to overcome this limitation, the matched FBG can be tuned to have a linear edge with its 3dB point matching with the sensing FBG.

Figure 4.1 (c) shows the edge filter detection method using a Wavelength Division Multiplexing (WDM) coupler [195]. The input light is split between two outputs depending on the wavelength. The spectral response of the WDM coupler is such that linear edge occurs between the wavelength of the first output and the second output. In the operation of the WDM coupler the light which is not transmitted to the output is not absorbed but rather directed to the second output.

Figure 4.1 (d) shows the edge filter detection method using a wavelength de-multiplexer,

allowing for the selection of the outputs based on different wavelength bands.

For all the schemes shown in Figure 4.1, a superluminescent diode (SLD) was used as the broadband light source.

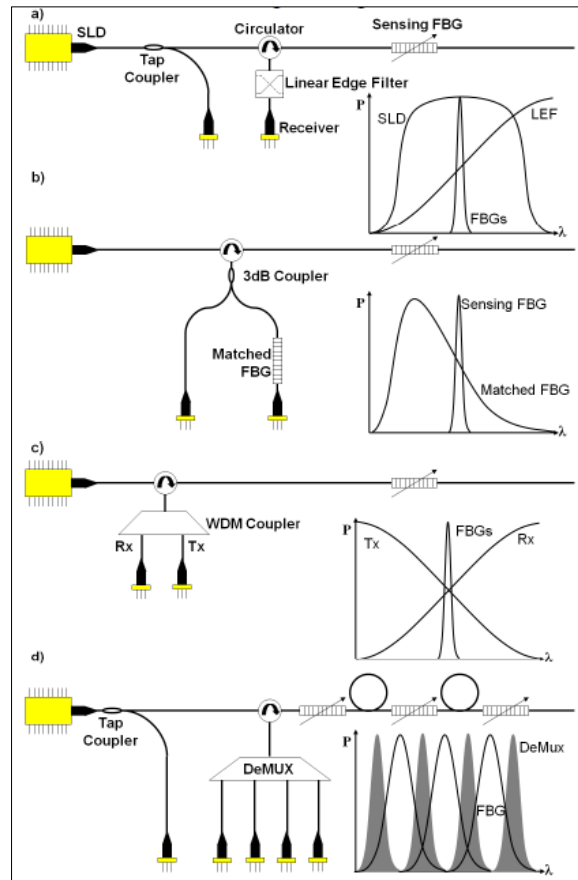


Figure 4.1 Edge filter detection method using a SLD light source, coupled with a) linear edge filter, b) matched FBG, c) WDM coupler and d) demultiplexer [192].

4.2.2 Power Detection Method

In the power detection method, the Bragg wavelength shift is detected using a spectrally-dependent source. In most of the cases, a laser is required and tuned to be centered at a specific wavelength. The power measured is the power of the laser after it has passed through the FBG sensor [192]. The main drawbacks of this technique are high costs and the difficulty in multiplexing. There are two power detection schemes widely reported using a linear edge source and the narrow bandwidth source respectively.

Figure 4.2 (a) shows the power detection method using a linear edge source, with its 3dB point matching with the Bragg wavelength of the manufactured FBG. The wavelength shift of the FBG then results in a direct change in the reflected intensity as it shifts up and down the edge of the source's spectrum [192].

Figure 4.2 (b) shows the power detection method using a narrow-band laser source with its bandwidth being located at the 3dB spectrum of the sensing FBG to detect the reflected power [196]. Figure 4.2 (c) shows the power detection method using a narrow-band laser source with its bandwidth being located at the 3dB spectrum of the sensing FBG to detect the transmitted power [197].

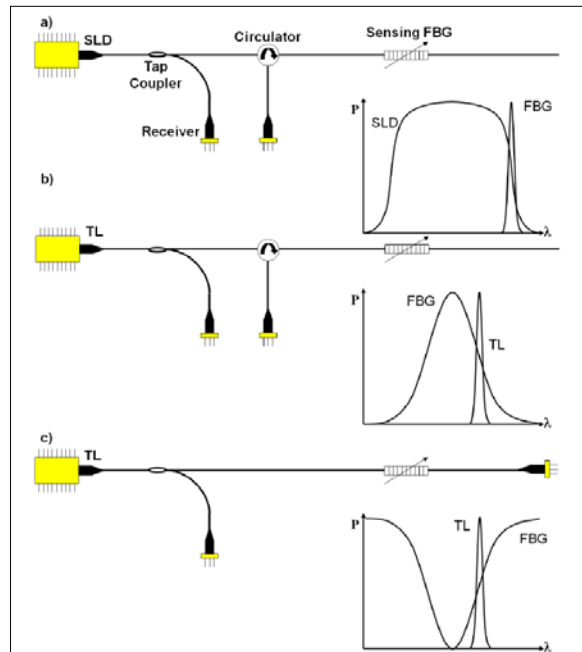


Figure 4.2 Power detection methods, a) broadband power detection, b) narrowband source with reflected component, c) narrowband source with transmitted component [192].

4.3 Sensors manufacturing process

All the FBGs evaluated and discussed in this thesis were manufactured using an excimer laser-based FBG fabrication facility at City, University of London as shown in Figure 4.3. Boron/Germanium co-doped fibers from Fibercore (PS1250/1500) were used as the photosensitive fibres to be imprinted with an interference pattern created by a phase mask after exposure to KrF excimer laser operating at 248 nm.

During the inscription process, the laser source was running at the pulse energy of 10 mJ and a pulse frequency of 100 Hz. Different phase masks were used in order to manufacture FBG sensors with different Bragg wavelengths for ease of multiplexing when wavelength-division-multiplexing method is used. As shown in Figure 4.3, a plano-cylindrical lens with a focal length of 200 mm was placed in front of the laser allowing the laser beam to be focused into a thin line with a width of approximately 0.5 mm and length of around 8 mm. The laser beam was projected to the phase mask to create an interference pattern which was subsequently

Chapter 4: FBG-based Cascaded Acoustic Sensors for Marine Structural Condition Monitoring

imprinted to the photosensitive fibre which was placed close to the phase mask as shown in Figure 4.4 to modulate its core refractive index.

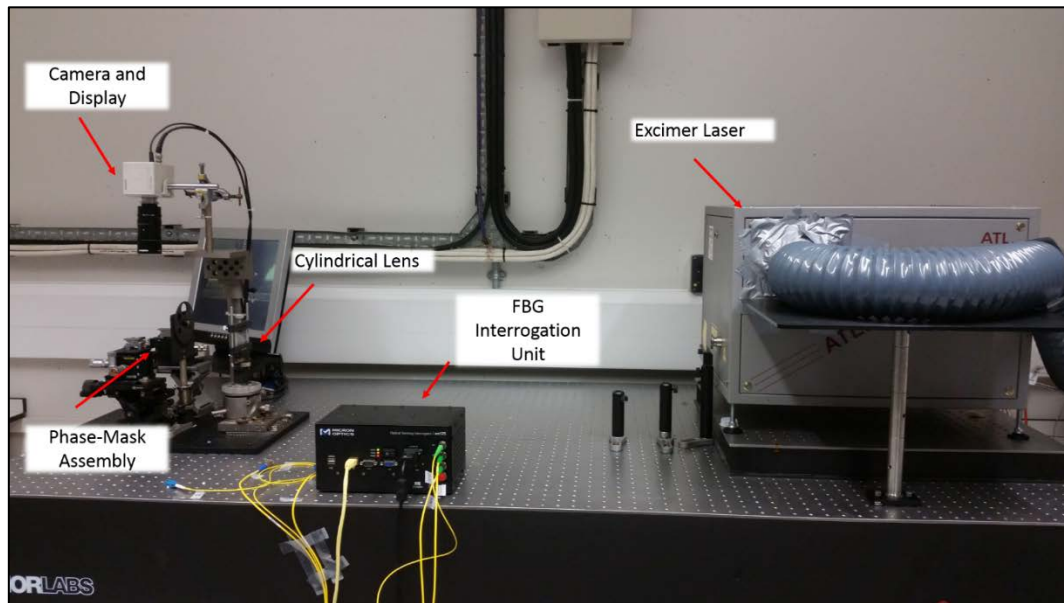


Figure 4.3 Basic configuration of FBG manufacturing setup at City, University of London

In order to monitor closely the manufacturing process and control the reflectivity of the FBG fabricated, it is essential to monitor the FBG by connecting it to an interrogator, sm125, manufactured by Micron Optics using an external fibre.

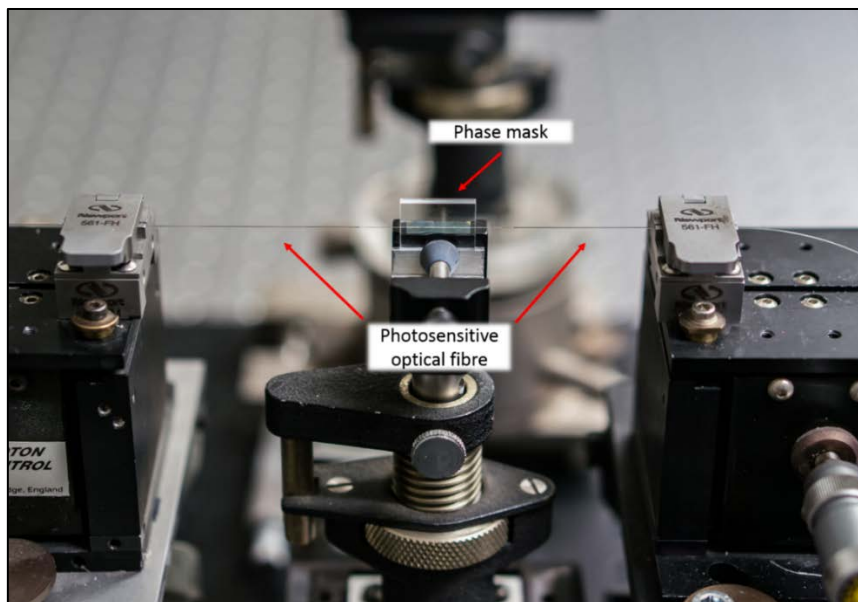


Figure 4.4 Phase mask setup for FBG manufacturing process at City, University of London

4.4 FBG-based acoustic sensor design and sensor characterization

In this research an edge filter detection method was used to capture the FBG signals when the sensors were subjected to acoustic pressure changes. To evaluate the effectiveness of the optical fibre sensors for acoustic detection, a cross-comparison has been made by monitoring acoustic waveforms using both FBG sensors and a PZT device (in terms of both shape and the arrival time). Figure 4.5 shows a layout of a glass plate where an FBG-based sensor array is installed adjacent to a PZT sensor. The acoustic excitation is induced by a ball dropping on to the glass plate at different locations and the acoustic signals received by both types of sensors are cross-compared.

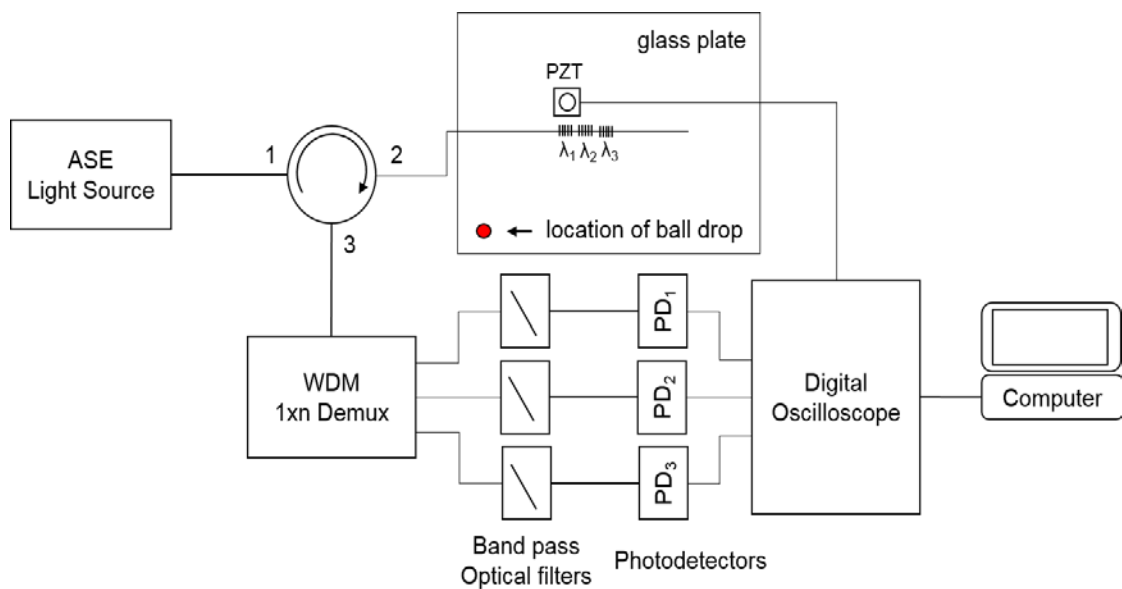


Figure 4.5 The experimental setup: the FBG-based cascaded acoustic sensor system, with a co-located PZT acoustic sensor for cross-comparison

As shown in Figure 4.5, broadband light was emitted from a C-Band ASE light source to port 1 of an optical circulator, with a maximum output of 20.9 dBm. The C-Band light source used in this work offers broad-band light in the region from 1525 nm and 1562 nm and the spectrum is shown in Figure 4.6.

Chapter 4: FBG-based Cascaded Acoustic Sensors for Marine Structural Condition Monitoring



Figure 4.6 The spectrum of the C-Band light source used for this experiment

The signals reflected from the FBGs are transmitted from port 2 to port 3 of the optical circulator. The fibre optic circulator operates in the wavelength range from 1525 nm to 1610 nm and was supplied by Thorlabs. From port 3, the narrow-band signals are transmitted through an optical fibre demultiplexer together with an array of optical filters before entering an array of photodetectors (PDA10CS-EC, Thorlabs) connected to the outputs of the filters each with a bandwidth of 17MHz at 0 dB gain option. The signals detected by the photodiodes were cross-compared with the signal detected by the PZT sensor, placed adjacent to the FBGs on the same glass plate. Prior to the recording of the PZT sensor data, both pre-amplification and signal attenuation modules were included to optimize the signal output.

Figure 4.7 shows a typical spectral profile of a narrowband near infrared (NIR) optical filter which is labelled as BPOF₁ and this optical filter has a full width half maximum (FWHM) of 12 nm and central wavelength of 1548.3 nm.

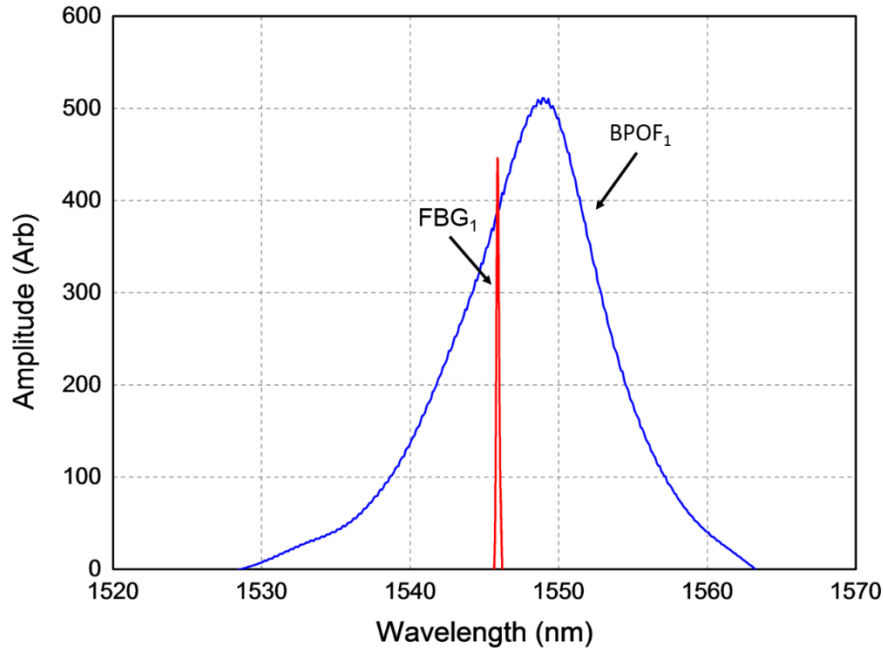


Figure 4.7 Spectral slope of the optical filter used in combination with FBG_1 optical sensor.

The spectral position of the first Fibre Bragg Grating (FBG_1) illustrated in Fig. 4.5 is shown in Fig. 4.7, confirming that the FBG centre wavelength is positioned on the steepest part of slope of the optical filter for achieving the maximum sensitivity. The same approach was used for the specification and design of all the other FBGs and associated optical filters in order to achieve a perfect matching of the sensors with optical filters in the array. The FBG_1 has a central Bragg wavelength of 1545.8 nm and has been manufactured to provide a high reflectivity of about 95%. The typical strain sensitivity of a FBG-based sensor is approximately $1 \text{ pm}/\mu\epsilon$. Thus the design of the sensors shown in Fig. 4.7 allows the measurement range to be approximately 2500 – 2800 $\mu\epsilon$ with a resolution of 8 $\mu\epsilon$.

4.5 Experimental Results

The experimental results obtained from both glass plate and a small metal plate tests are reported in this subsection. In both cases, the signals recorded by FBG-based acoustic sensors were cross-compared to those recorded by PZT conventional sensors in both time domain and frequency domain.

4.5.1 Glass plate tests

As shown in Fig.4.5, dropping a tiny steel ball was used as an excitation source to create a reproducible acoustic signal – the glass plate was resting on 3 ball bearings. In order to analyze

Chapter 4: FBG-based Cascaded Acoustic Sensors for Marine Structural Condition Monitoring

the arrival time and shape of the waveforms in the time domain, the captured waveforms from the 0.3 g ball-drop received from both FBG₁ and a PZT sensor are shown in Fig. 4.8.

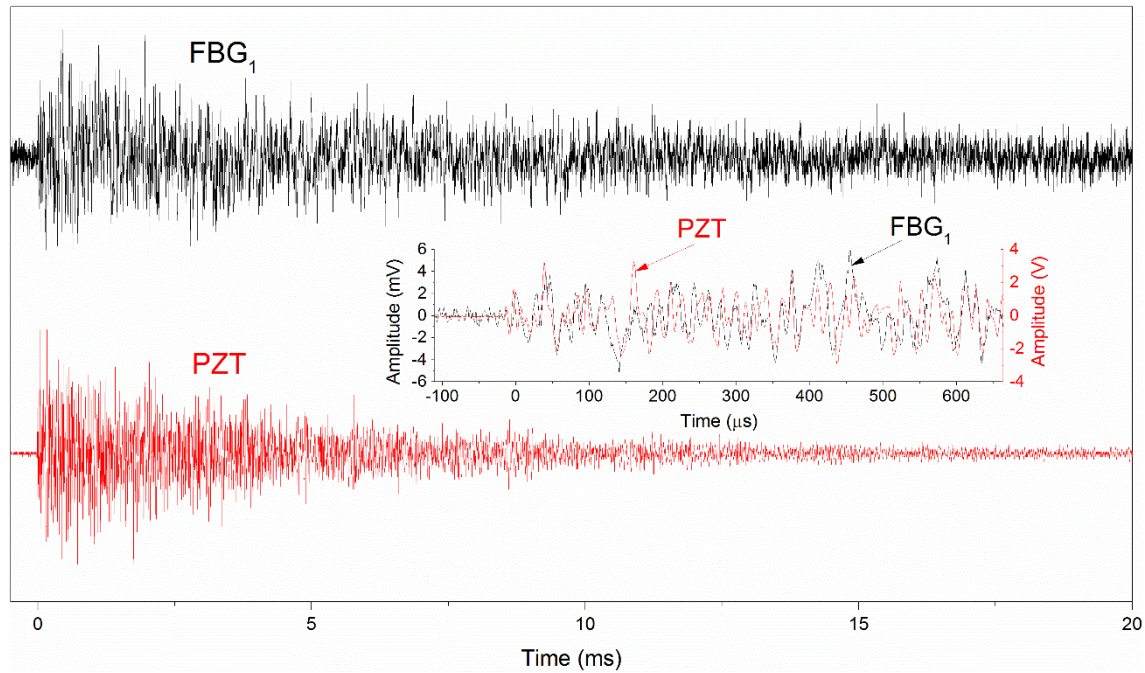


Figure 4.8 Time waveforms detected by both FBG₁ and PZT based acoustic sensor when glass plate was excited using a steel ball.

Comparing the acoustic signals produced, Fig. 4.8 shows the close similarity that exists between the waveforms received from both the PZT and FBG devices. The signal arrival times and waveform shapes are evident (as shown in the inset) – giving confidence that the FBG-based sensor can give signals similar to those seen from the industry-standard PZT sensors. Cyanoacrylate adhesive was used as the bonding agent for the FBG-based sensor to the glass plate was chosen to ensure an appropriate transfer of the acoustic wave whilst achieving the same arrival time of the acoustic signals using both sensors (Fig. 4.8 inset) further underpins this confidence. Considering the full waveform data for both sensors, it is evident that the level of background noise from the FBG sensor is higher than the PZT sensor. This is an effect caused by the interrogation setup used and can be improved further by using a higher-power optical ASE source or through implementation of means of an optical amplification through Erbium Doped Optical fibre.

The signal from the 3 cascaded FBGs (with a physical interval on the glass plate of 10 mm) have also been obtained and cross-compared. It was found that all the FBG sensors responded – showing a similar arrival time and the same waveform shape, when compared to the response of the PZT sensor to FBG₁. The signals received are shown in Fig. 4.9 – it can be seen that the

Chapter 4: FBG-based Cascaded Acoustic Sensors for Marine Structural Condition Monitoring

background noise from the FBG data is higher than that for the PZT sensor. However, the signal to noise ratio (S/N) is satisfactory for a wide variety of acoustic sensing applications, particularly where the pulse arrival time is the most significant parameter (often it is more significant than the waveform shape.)

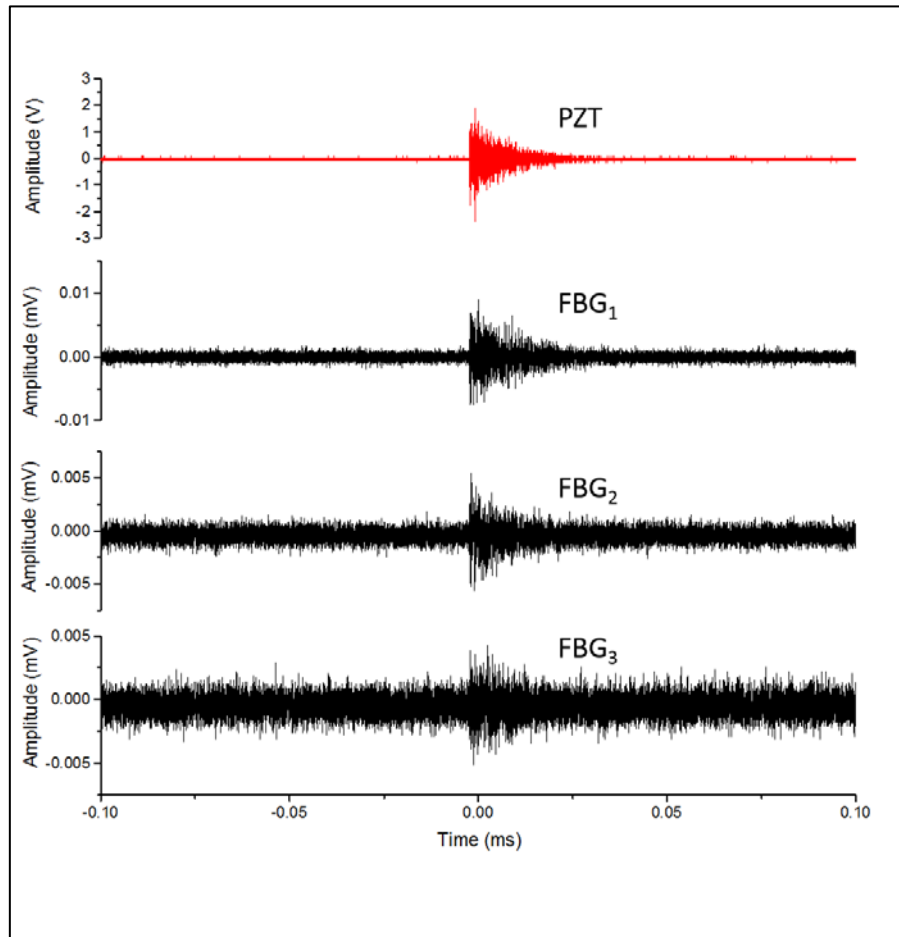


Figure 4.9 Cross – comparison of waveforms detected by both the PZT and multi-point FBGs

It is interesting to note the effect of the location of an FBG (and its corresponding S/N.) – for example, FBG₁ has the highest S/N (as it is closest to the source), whereas FBG₃ has the lowest. It implies that the further the FBG-based sensor is located from the source, lower the S/N is. However, this demonstration has shown that it is possible to detect the very weak acoustic signal generated from the dropping of a very small ball on a glass plate, using a multi-point FBG sensor array. Given the speed of sound in solid glass (4540 m/s) and the time needed for an acoustic signal to propagate from the source to both FBG₁ and the PZT, it is possible to calculate the distance between the source of excitation and the sensors, which is an important parameter in marine structural condition monitoring.

Data collected show that the time for the first acoustic wave to arrive at the location of FBG₁ is 26.43 μ s which compares well to the time measured for the almost co-located PZT, of 27.19

Chapter 4: FBG-based Cascaded Acoustic Sensors for Marine Structural Condition Monitoring

μs . This small time difference in the arrival times arises from their slight spatial mismatch, but shows clearly from the similarity of the data that those two sensors are located very close to each other. It can thus be calculated that the distance from the excitation source to the two sensors is ~ 120 mm. This set of very positive and encouraging results was used for the follow-on metal plate tests.

4.5.2 Metal plate tests for cavitation monitoring

In this subsection, both PZT and FBG acoustic sensors were bonded to a steel plate, DH36 grade, with a dimension of $50 \times 50 \times 5$ mm for the cavitation tests. Fig. 4.10 shows a test-rig set-up for the acoustic tests on a metal plate which was placed in a water tank, with an excitation sonotrode mounted 1 mm above.

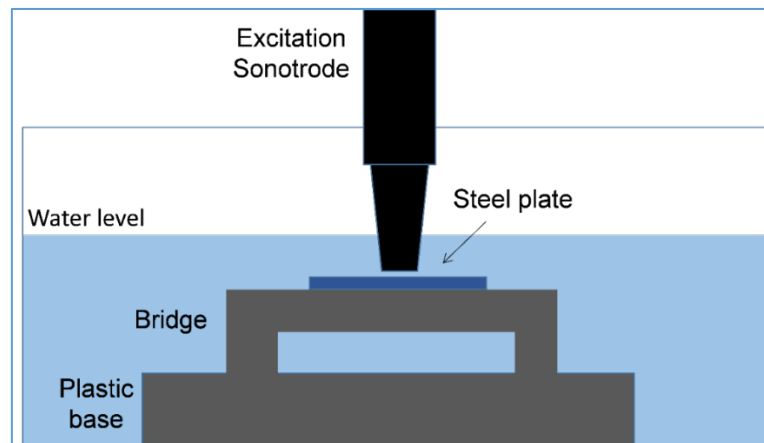


Figure 4.10 Schematic of the setup for the acoustic tests of the steel plate instrumented with both FBG and PZT acoustic sensors.

The plastic bridge placed at the bottom of the water tank was used both to support the steel plate and to adjust the distance between the metal plate and the sonotrode. The plastic bridge with the instrumented sample is shown in some Fig. 4.11 after the tests were completed. In the middle of the steel plate, it is noticeable that cavitation erosion has occurred.

Chapter 4: FBG-based Cascaded Acoustic Sensors for Marine Structural Condition Monitoring

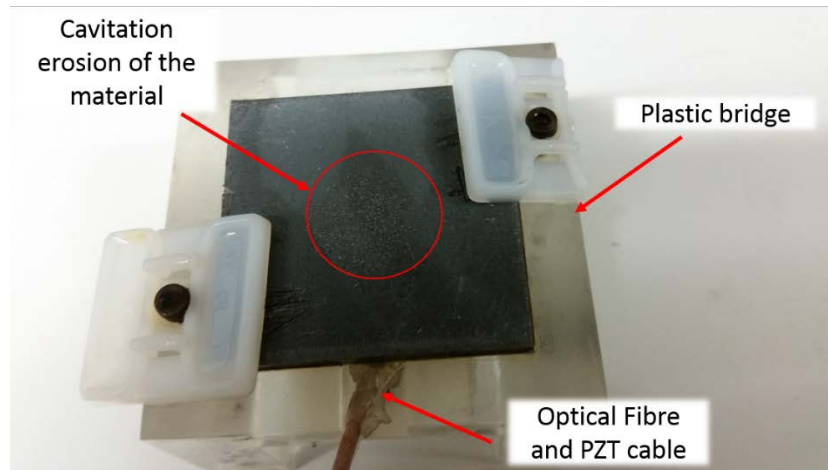


Figure 4.11 Steel plate instrumented with PZT and FBG acoustic sensors (placed underneath) showing the cavitation erosion occurred in the middle of the plate

The sonotrode, which is a Hielsher UIP1000hd ultrasonic transducer has a standard operating frequency of 19.5 kHz. Both the FBG and PZT acoustic sensors were fixed onto the bottom surface of the metal plate using cyanoacrylate adhesive. The waveforms detected by both the PZT and the co-located FBG sensors, when an excitation sonotrode is operated at a standard frequency of 19.5 kHz, are shown in Figure 4.12. This test was repeated several times in order to evaluate the repeatability of the measurements and to ensure that the sensors are reliable and gave a repeatable signal.

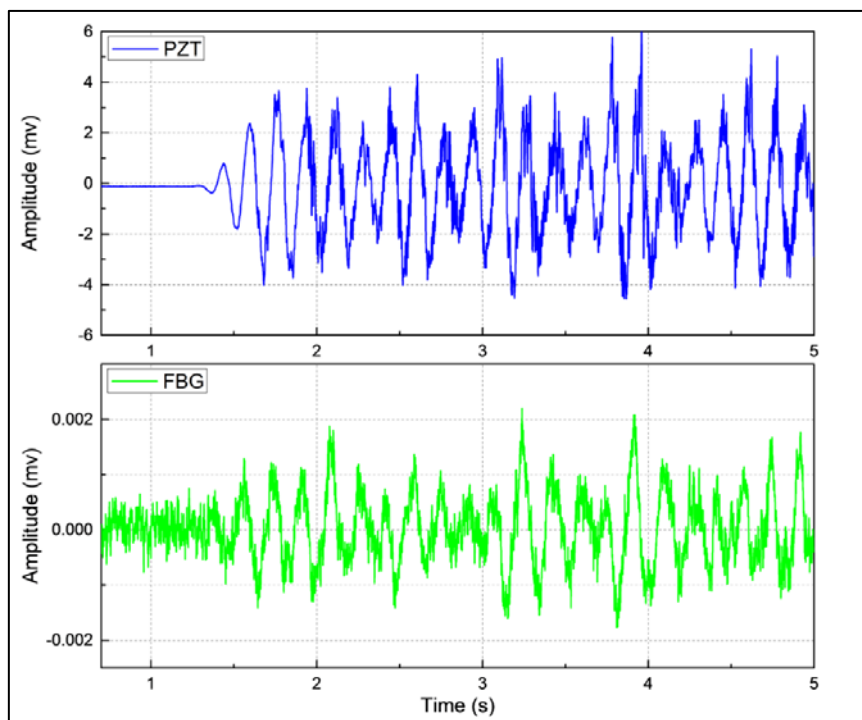


Figure 4.12. Acoustic signals acquired by the co-located FBG-based and PZT acoustic sensors when the metal plate is subject to the excitation of the sonotrode at a frequency of 19.5 kHz

Fig.4.13 shows the frequency-domain data obtained from both types of sensors. A Fast Fourier Transform (FFT) algorithm was used to process the time-domain data captured and the output is shown in Fig. 4.13. It is noticeable that the same frequency component located at 19.5 kHz, the excitation frequency from the sonotrode, has been captured by both sensors. The figure shows that the FBG sensor has some additional second harmonic features (which can readily be filtered out).

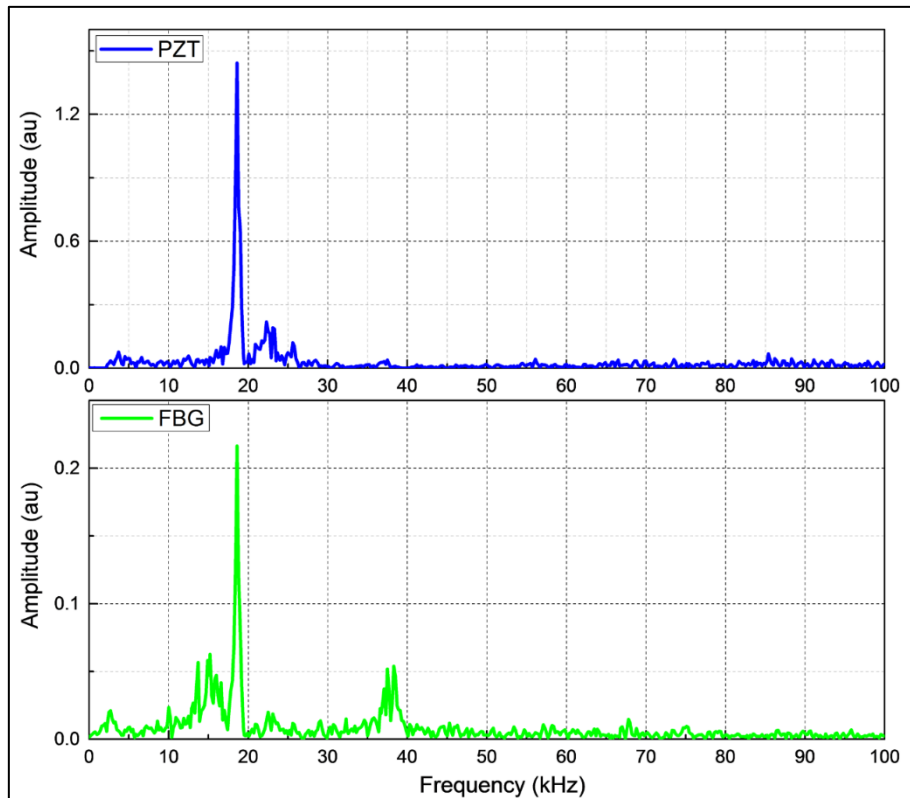


Figure 4.13 Frequency response of a FBG-based acoustic sensor and a PZT acoustic sensor illustrating the close match (in this case with a standard sonotrode frequency of 19.5 kHz).

It can be concluded that both the glass plate and metal plate frequency response data show good agreement between the optical and electrical acoustic sensors, giving confidence to the use of the FBG-based sensors in such applications. Their ease of being multiplexed has not been exploited in this work, but for the marine condition monitoring applications, this shows a significant potential.

4.6 Summary

This chapter included a detailed investigation into basic principles of FBG sensors for dynamic acoustic pressure measurement as well as experimental investigation of the FBG sensor system developed at City, University of London. Two different experimental setups, glass plate tests and metal plate tests have been evaluated and the research undertaken has shown that the FBG-based sensor evaluated shows a similar and satisfactory performance to the industry-standard PZT-based sensors for acoustic monitoring on glass and metal plates.

A cascaded FBG-based acoustic sensor system has thus been successfully developed and verified through both the glass plate tests with an aim to find key acoustic signatures. A good agreement between FBGs and their co-located PZT acoustic sensors has been reached for this particular case, showing similar arrival time and shapes of the detected waveforms. There is a potential, however, to increase the signal-to-noise ratio of FBG sensors by using a light source with higher output power or through optical based amplification.

This research is directed towards the identification of cavitation signals of material structures. To evaluate the feasibility of this optical approach, a metal piece integrated with both FBG and PZT sensors were excited by a sonotrode with the results being obtained and cross-compared. The positive results obtained from this have led to further extensive tests on a marine rudder using a similar sensor layout, which are discussed in detail in Chapter 5.

Chapter 5

Fibre Bragg Grating-based Acoustic Sensor Array for Improved Condition Monitoring of Marine Lifting Surfaces

5.1 Introduction

Cavitation erosion is a phenomena that affects a number of structures in the marine industry. The most common structures that can be affected are propellers, support brackets, marine lifting surfaces, etc. The onset of the erosion leads to poor performance, reduced efficiency or even to more severe structural damages in some extreme cases. A majority of marine structures include a metallic plate/shell and stiffeners which are all subjected to corrosion and fatigue damage, where guided waves (especially Lamb waves) with particular frequencies can travel relatively long distances with low losses, offering large area coverage [198].

The focus of this chapter is to report the work on the development and evaluation of an FBG-based acoustic sensor array for improved condition monitoring of marine lifting surfaces. To do so, the sensor system was evaluated first by being instrumented onto a glass plate and a steel plate, allowing the detection of acoustic signals generated under known, standardized conditions which was reported in Chapter 4. The aim of the work reported in this chapter is to validate this method in a more ‘real world’ application by instrumentation of a marine lifting surface with the performance of both PZT and FBG-based sensors being evaluated and simultaneously cross-compared.

In this Chapter, an array of FBG-based sensors was instrumented on to a marine lifting surface for dynamic acoustic pressure monitoring. The signals were interrogated using the optical-filter demodulation scheme, reported in Chapter 3, when the marine lifting surface was excited using ultrasound sonotrode with a standard frequency of 26 kHz. The triangulation method was used for the excitation source localisation.

The structure of this Chapter is designed as follows: it begins with the theoretical background of the triangulation method highlighting the main equations used for source localisation. It is followed by a discussion on the experimental setup used for this work, providing details of the sensors layout and the dimensions of the structure under testing. The final part of the chapter presents the experimental results obtained when the sonotrode is excited at different locations.

5.2 Theoretical background of acoustic source localization

The theoretical background of the triangulation method used in this work for the localization of the source of acoustic emission is reported in this subsection. As Tobias [199] reported and illustrated in Fig. 5.1, an array of three sensors is envisaged, and located respectively at points $S_0(0, 0)$, $S_1(x_1, y_1)$ and $S_2(x_2, y_2)$. The location of the acoustic emission source at $P(x, y)$ is thus defined as follows, assuming the distance between P and S_0 is r , P and S_1 is $r + \delta_1$, P and S_2 is δ_2 , as shown in Figure 5.1.

$$\delta_1 = PS_1 - PS_0 = \Delta t_{10} \cdot v \quad (5.1)$$

$$\delta_2 = PS_2 - PS_0 = \Delta t_{20} \cdot v \quad (5.2)$$

where, v is the velocity of acoustic wave propagation in the material (with the reasonable assumption that the material is uniform) and Δt_{10} and Δt_{20} respectively represent the arrival time differences of the signals received by sensors 1 and 0 and sensors 2 and 0 respectively.

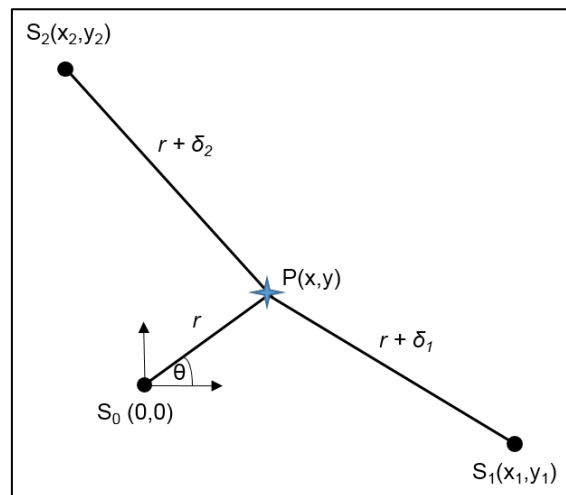


Figure 5.1 Emission signals from Source P can be detected by an arbitrary 3-sensor array at different locations with different arrival times [199].

$$x^2 + y^2 = r^2 \quad (5.3)$$

$$(x - x_1)^2 + (y - y_1)^2 = (r + \delta_1)^2 \quad (5.4)$$

$$(x - x_2)^2 + (y - y_2)^2 = (r + \delta_2)^2 \quad (5.5)$$

Using the trigonometric functions (5.1) - (5.5), the distance from the source and the ‘zero point’ can be calculated as:

$$r = \frac{A_1}{2 \cdot (x_1 \cdot \cos\theta + y_1 \cdot \sin\theta + \delta_1)} = \frac{A_2}{2 \cdot (x_2 \cdot \cos\theta + y_2 \cdot \sin\theta + \delta_2)} \quad (5.6)$$

where,

$$A_1 = x_1^2 + y_1^2 - \delta_1^2 \quad (5.7)$$

$$A_2 = x_2^2 + y_2^2 - \delta_2^2 \quad (5.8)$$

Equation (5.6) can be further expanded to,

$$(A_1 \cdot x_2 - A_2 \cdot x_1) \cdot \cos\theta + (A_1 \cdot y_2 - A_2 \cdot y_1) \cdot \sin\theta = A_2 \cdot \delta_1 - A_1 \cdot \delta_2 \quad (5.9)$$

The final equation used for the calculation of the angle θ is given as Eq. (5.10).

$$\begin{aligned} \theta &= \frac{(A_1 x_2 - A_2 x_1) \cdot \cos\theta}{\sqrt{(A_1 x_2 - A_2 x_1)^2 + (A_1 y_2 - A_2 y_1)^2}} + \frac{(A_1 y_2 - A_2 y_1) \sin\theta}{\sqrt{(A_1 x_2 - A_2 x_1)^2 + (A_1 y_2 - A_2 y_1)^2}} \\ &= \frac{A_2 \delta_1 - A_1 \delta_2}{\sqrt{(A_1 x_2 - A_2 x_1)^2 + (A_1 y_2 - A_2 y_1)^2}} \end{aligned} \quad (5.10)$$

The angle θ could thus be determined precisely from the known positions of the sensors S_1 and S_2 and the measured signal arrival time differences at those points, corresponding to the position of S_0 , Δt_{10} and Δt_{20} and the known acoustic propagation velocity. Naturally, a value of θ yielding a positive value of r in Eq. (5.6) must be determined in order to have a valid solution. Knowing the absolute time of arrival and two time differences, the location of the excitation source can then be calculated.

5.3 Experimental setup

The marine lifting surface (rudder), supplied by BAE systems, and is shown in Fig. 5.2 where the layout of the marine lifting body under investigation is emphasized. It consists of an upper surface 5.2 (a) where both types of sensors have been installed and inner surface, 5.2 (b) including the shaft.

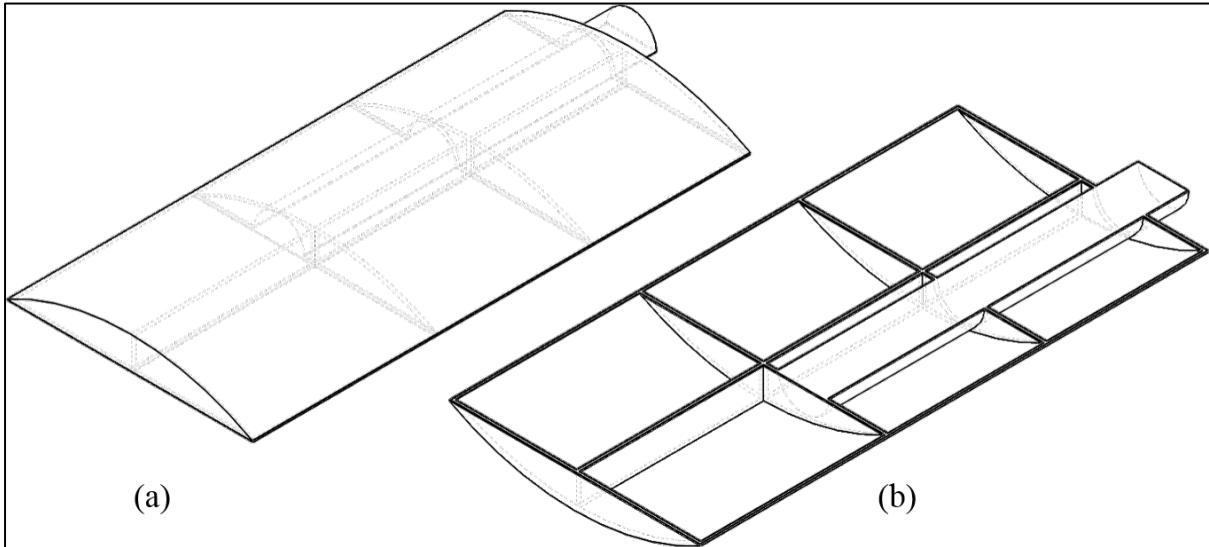


Figure 5.2 Design of the marine lifting surface under investigation with a) upper surface where sensors are to be installed, b) inner surface with the shaft

All the sensors, including 4 FBG-based acoustic sensors in an array and 4 co-located PZT acoustic sensors, were instrumented onto the upper surface of this marine lifting structure, as illustrated in Fig.5.3. It shows the overall sensor distribution and coordinates of the sensing points of interest. Both types of sensors were used to record the signal arrival times at these known sensor locations (marked as S0 to S3 in Fig 5.3). The measurements were undertaken at a room temperature, mirroring the typically steady temperature of the local marine environment. However, a correction for any temperature changes can readily be added – a further set of FBGs configured to be sensitive *only* to temperature can be used, so that the acoustic signal only can be obtained. This would be achieved through tailored mounting of FBG sensors at the positions that are not sensitive to this dynamic perturbations and still close enough to FBG-based AE sensors in order to provide a correct compensation and avoid large measurement errors.

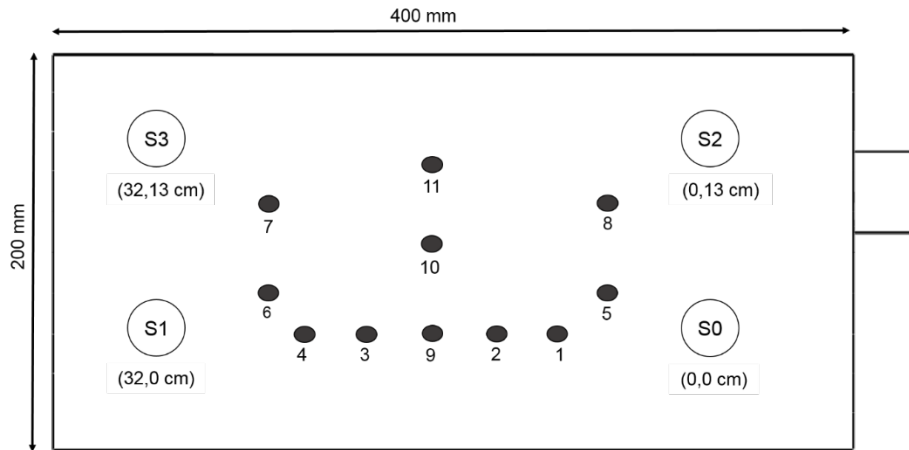


Figure 5.3 Overall distribution of positions (dark dots) where the impact was applied during the tests. FBG-based acoustic sensors and PZT sensors locations are marked S0, S1, S2 and S3.

The standardized acoustic impacts were applied using an ultrasonic sonotrode with a standard frequency of 26 kHz, at various locations. Fig. 5.3 shows 11 points where the excitation was applied sequentially – tests were repeated several times to ensure consistency. The points are represented by dark dots in Fig 5.3. and their locations in the coordinate system are summarized in Table 5.1. The speed of sound used for all calculations is the speed of sound in the steel and whose value is 5600 m/s. Fig. 5.4 shows a setup of the test-rig used for cavitation tests. The steel marine lifting surface (rudder) was placed in a water tank and the excitation sonotrode was mounted 1 mm above the upper surface. The sonotrode standard frequency used again is 26 kHz with the maximum power of 200W. The marine lifting surface was not fixed rigidly, but suspended in the water as shown in Fig. 5.4.

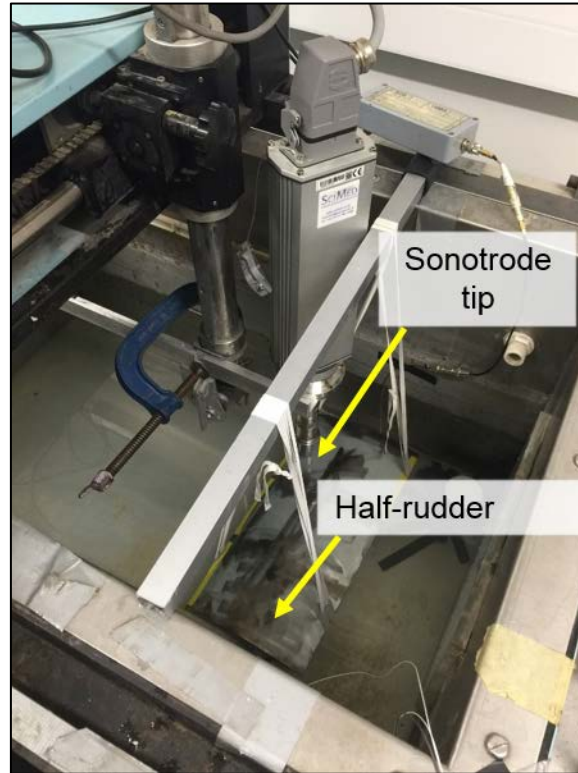


Figure 5.4 Cavitation tests of the half-rudder instrumented with both FBG and PZT acoustic sensors

5.4 Experimental results

The data collected from both types of sensors were analysed in both the time and the frequency domains, where the latter was also used for verification of the excitation frequency. In the time domain, the time of arrival of the waveform detected by sensor array at known locations was used to determine the acoustic emission source location, through applying Eq. (5.6) and Eq. (5.10). All 11 impact points were excited several times to evaluate the repeatability of the measurements and to minimize experimental uncertainty. Two points that are referred to as the middle point (Point 10) of the lifting surface and the position between S_0 and S_1 (Point 9) were analysed in more detail in this section, showing the calculation method used.

5.4.1 Impact point in the middle of lifting surface

The impact position reported in this subsection was located in the middle of the tested marine lifting surface with the coordinates (16cm, 7cm), corresponding to (x, y) . The source of excitation was placed above this point at the height of 1 mm from the marine lifting surface. Fig. 5.5 shows typical time related amplitude results obtained. The waveforms were recorded by both the FBG S_0 and the co-located PZT sensor when the excitation is located at point 10,

as shown in Fig. 5.3. The data shows exactly the same arrival time which is suspected considering that these two sensors are very closely positioned.

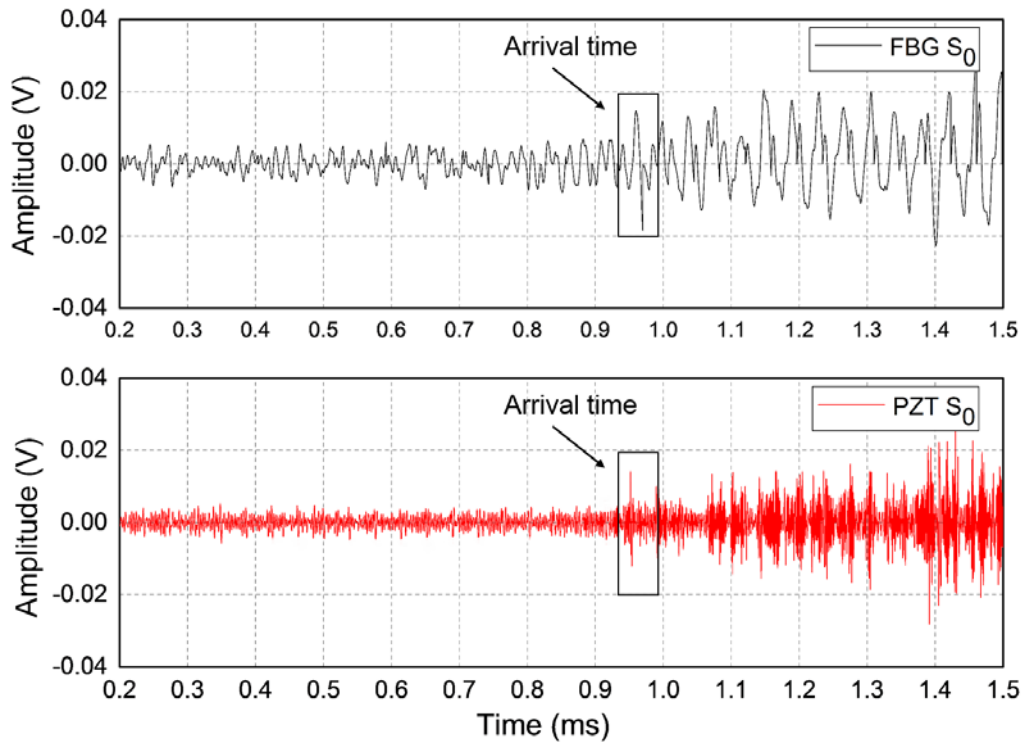


Figure 5.5 Acoustic signals acquired by both FBG-based acoustic sensor and co-located conventional PZT sensor indicating similar time of arrival (excitation point 10 (16cm, 7cm))

Further work similar to the data reported in Fig. 5.6 shows that the signals detected by all four FBG-based acoustic sensors at positions S0, S1, S2 and S3 received from the same excitation point. The four waves are shown to arrive at a similar time, as expected, (as the source is placed in the middle of the marine lifting surface). The similar arrival time was first visually observed, and then verified using a cross-correlation function applied to certain parts of the waveform – those where the signal was not affected by various reflections observed during the excitation. Various reflections that have occurred during the experiment are related to the size of the marine lifting body as well as the size of the tank used for the experiments. This similar arrival time, verified by the cross-correlation function, indicates that the signals detected at all the sensor positions, are matched in phase. S0 and S2 see the peak signal arriving slightly ahead of that at S1 and S3, indicating a slight deviation of the excitation from the centre to the right of the test sample.

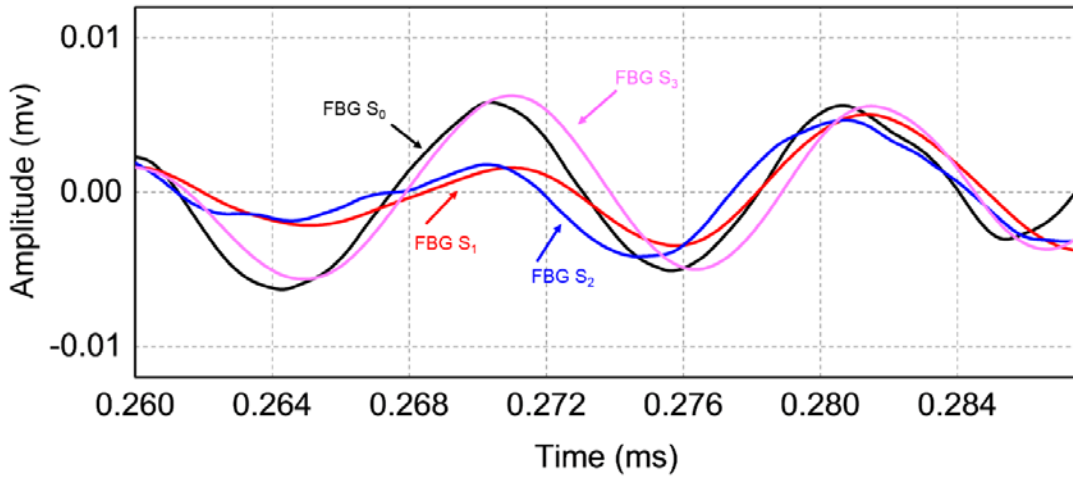


Figure 5.6 Acoustic signals acquired by the optical based acoustic sensors at all four sensor locations of the half-rudder when rudder was subject to excitation of the sonotrode at Point 10

Fig. 5.7 shows the frequency-domain data obtained from all the FBG-based acoustic sensors used and the response from co-located PZT sensors. The data verify the known ‘standard frequency’ of the sonotrode excitation, of 26 kHz.

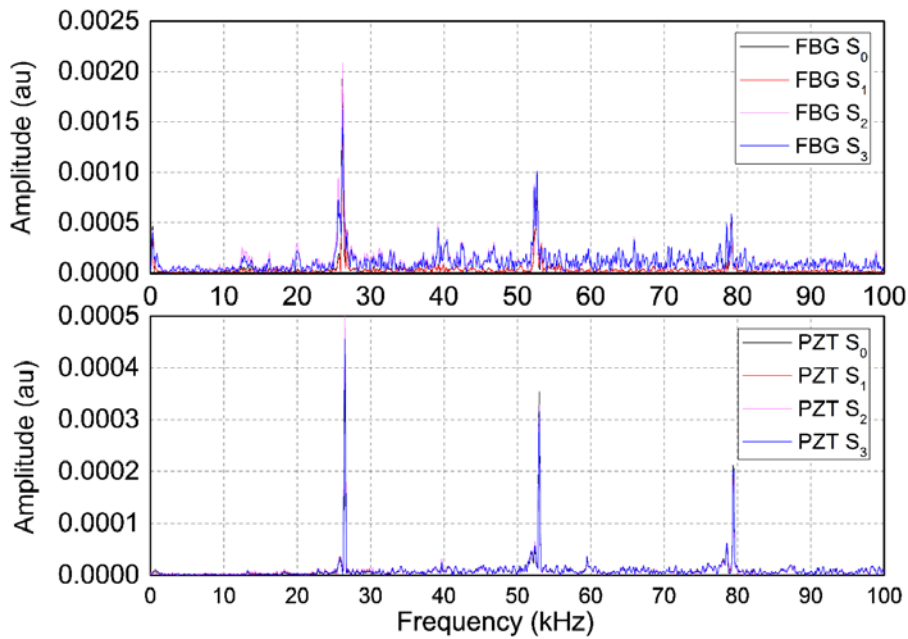


Figure 5.7 Frequency response of FBG-based acoustic sensors and PZT acoustic sensors indicating a close match of standard sonotrode frequency of 26 kHz when excited at Point 10.

Fig. 5.7 also shows that there is a close match in the frequency domain data from the data received from both types of sensors used, when the marine lifting surface was used under the sonotrode excitation.

5.4.2 Impact point between sensor locations S_0 and S_1

In this set of experiments, the sonotrode was placed between the S_0 and S_1 sensors positions which corresponds to (16cm, 0cm) coordinates. The distance between the sonotrode and marine lifting surface was kept the same as for the previous location reported.

Fig. 5.8 shows the waveforms recorded by both the FBG-based optical sensors and the co-located PZT sensors when the sonotrode excitation was placed at Point 9, which is located between S_0 and S_1 in Fig. 5.3. Both sensors have indicated the same arrival time for the signal.

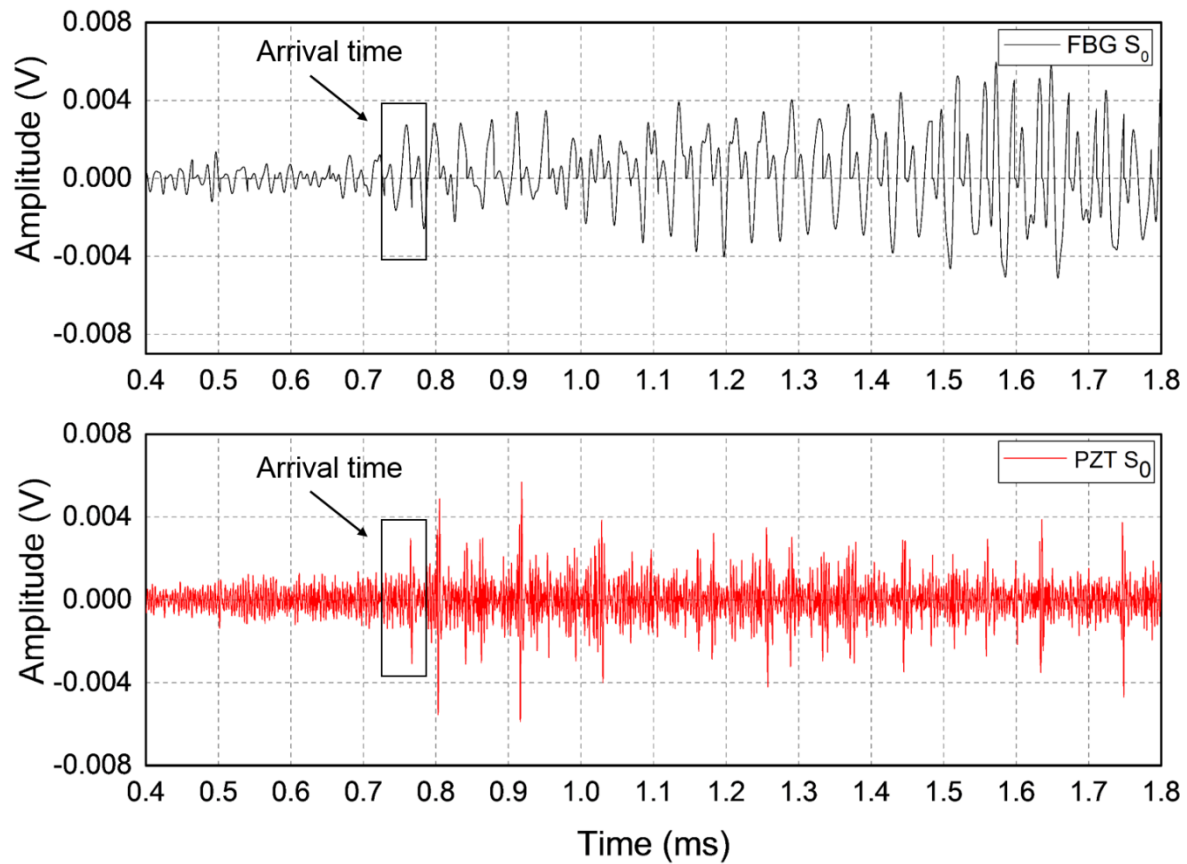


Figure 5.8 Acoustic signals acquired by both FBG-based acoustic sensor and co-located conventional PZT sensor indicating similar time of arrival (excitation point 9 (16cm, 0cm))

Figure 5.9 shows the data received by all the four FBG sensors used. Sensors 1 and 0 positions received signals first as expected, due to their closer locations to the excitation compared to Sensors 2 and 3. Again the slightly early arrival of the signal at the position of Sensor 2 compared to Sensor 3 indicates that the excitation is slightly offset to the right: this is evident by the value of Δt_{10} (measured to be $0.88\mu\text{s}$) rather than the expected zero (from the reference) and thus having been based on the assumption that that source was located exactly in the middle

of those two sensing points. This positional error was possibly caused by movement of the rudder, while being excited.

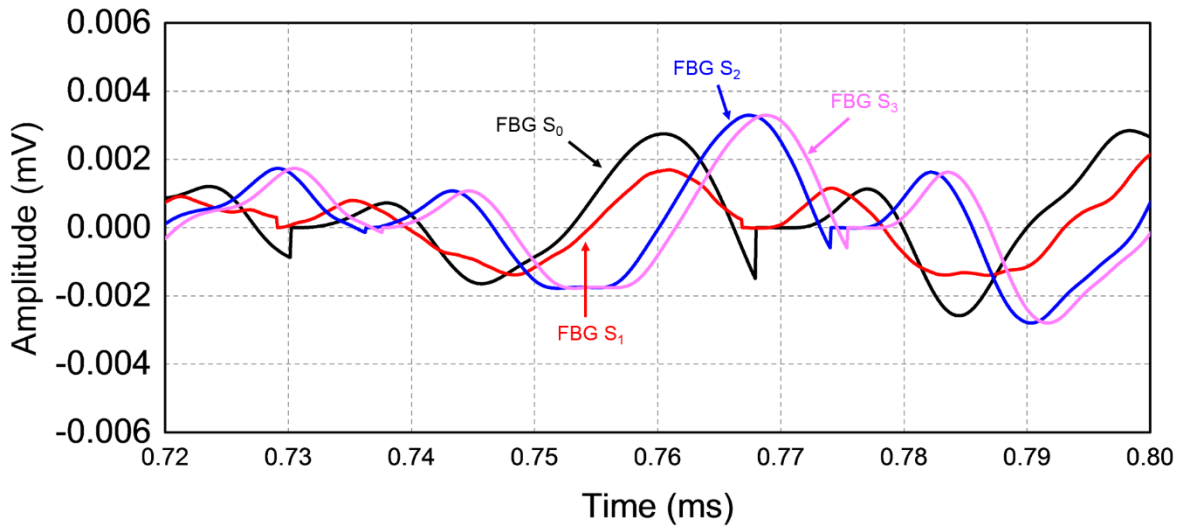


Figure 5.9 Acoustic signals acquired by the optical based acoustic sensors at all four sensor locations of the marine lifting surface when it was subject to excitation of the sonotrode at Point 9

Fig. 5.10 shows the frequency-domain data obtained from all FBG-based acoustic sensors and also from the PZT sensors when the sonotrode was mounted between the S0 and S1 sensor points. It is encouraging to see from these results that it is clearly indicating the standard frequency of the sonotrode used, which is 26 kHz.

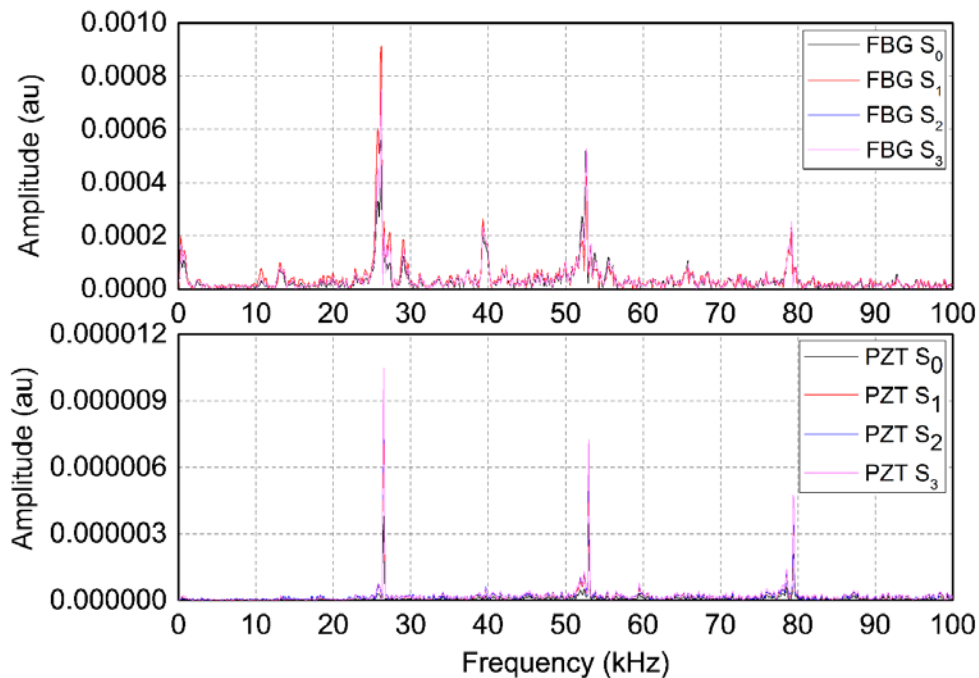


Figure 5.10 Frequency response of FBG-based acoustic sensors and co-located PZT acoustic sensors indicating capture of standard sonotrode frequency when excited at Point 9

Chapter 5: Fibre Bragg Grating-based Acoustic Sensor Array for Improved Condition Monitoring of Marine Lifting Surfaces

The data collected show that the frequency domain data captured by all four PZT acoustic sensors show a close match with the frequency-domain data captured by the FBG-based acoustic sensors, giving further confidence in the optical sensor technique. Considering the a satisfactory match in results obtained, it shows that the optical technique is well suited to this type of application.

5.5 Discussion of the results obtained

The first column in Table 5.1 shows the expected coordinates of the 11 Points of the excitation source mapped in Figure 5.3. By applying the triangulation method explained in this chapter, the source coordinates can be calculated based on the signals received by FBG-based acoustic sensors and their collocated PZT sensors. The values obtained are reported in Table 5.1.

Table 5.1 Cross Comparison between FBG and PZT Detected Source Coordinates (x, y)

Expected source coordinates [cm]	Source coordinates detected by FBGs [cm]	Source coordinates detected by PZTs [cm]
1 (10,0)	(11, 0.2)	(9.4, 0.28)
2 (13,0)	(13.4, 0.24)	(13, 0.12)
3 (19,0)	(19.7 ,0.1)	(20.8 ,0.35)
4 (22,0)	(23.1, 0.25)	(23, 0.24)
5 (8,3.2)	(9.2, 3.4)	(9, 3.1)
6 (24,3.2)	(24.2, 3.6)	(23.8, 3.4)
7 (24,9.8)	(26.4, 10.5)	(24.1, 9.6)
8 (8,9.8)	(7.4, 10.4)	(7.4, 10.1)
9 (16,0)	(15.2, 0.4)	(15.3, 0.25)
10 (16,7)	(16.8, 7.6)	(16.2, 7)
11 (16,14)	(16, 14.1)	(15.6, 14.3)

The data seen in Table 5.1 show a summary of the calculated locations obtained using equations (5.6) and (5.10) and the arrival times captured by both fibre optic and electrical sensors when the excitation is located at 11 different positions, as indicated in Fig. 5.3. The small deviation in the estimation of the location could be caused by the small differences in the set-for the two sets of experiments carried out: thus the mobility of the marine lifting surface or the slightly different positioning of the excitation source can cause such deviations.

Chapter 5: Fibre Bragg Grating-based Acoustic Sensor Array for Improved Condition Monitoring of Marine Lifting Surfaces

The simple illustration of a cross-comparison between the two types of sensors used is shown diagnostic in Fig. 5.11, where the red circles represent the known sonotrode excitation points and the blue and black crosses, respectively represent the calculated locations of the excitation source based on the data obtained from the PZT and FBG sensors. The pattern of close agreement between the results obtained with the two sets of sensors is evident from figure 5.11.

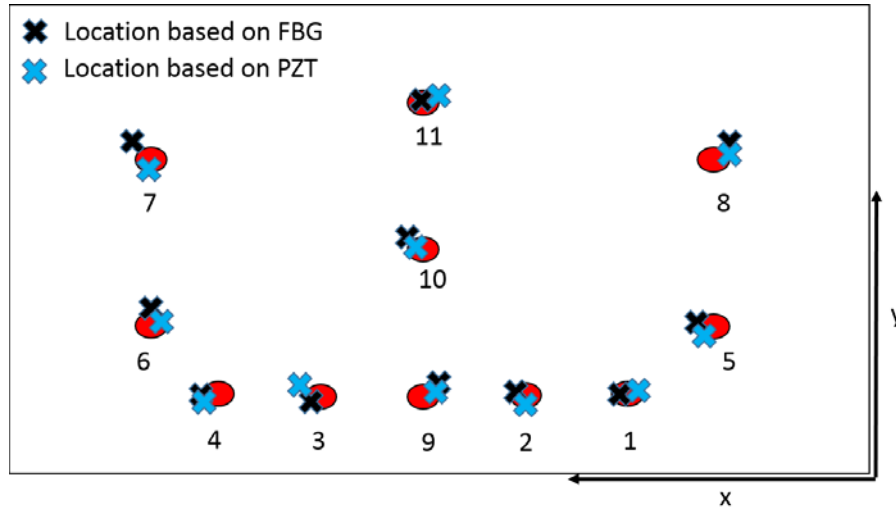


Figure 5.11 Calculated acoustic emission source locations based on the data from both FBG-based acoustic sensor (represented by ‘x’) and PZT based acoustic sensor (represented by ‘x’)

The largest deviation seen between the calculated and the known locations is observed to be at location 7. This most likely arises as it is a position which is quite close to the edge and thus the number of reflections at the edge of the rudder or the movement of the half-rudder in the water after excitation as the rudder was not fixed during the whole course of the tests could likely have caused this.

The deviation between the point of impact (assumed the ‘true location’) and the point measured by the FBG-based and the PZT-based sensors is tabulated below in Table 5.2, with the average deviation determined (assuming all deviations are ‘positive’).

Chapter 5: Fibre Bragg Grating-based Acoustic Sensor Array for Improved Condition Monitoring of Marine Lifting Surfaces

Table 5.2 Deviations measured using both FBG-based and PZT-based sensors (x, y)

Impact Point	Deviation Measured Using FBG-based sensor [cm]	Deviation Measured using FGB-based sensor [%]	Deviation Measured Using PZT-based sensor [cm]	Deviation Measured using PZT-based sensor [%]
1	(1, 0.2)	(10, 6.67)	(0.6, 0.28)	(6, 9.33)
2	(0.4, 0.24)	(3.07, 8)	(0, 0.12)	(0, 4)
3	(0.7, 0.1)	(3.68, 3.33)	(1.8, 0.35)	(9.47, 11.66)
4	(1.1, 0.25)	(5, 8.33)	(1, 0.24)	(4.54, 8)
5	(1.2, 0.2)	(15, 6.25)	(1, 0.1)	(12.5, 3.12)
6	(0.2, 0.4)	(0.83, 12.5)	(0.2, 0.2)	(0.83, 6.25)
7	(2.4, 0.7)	(10, 7.14)	(0.1, 0.2)	(0.42, 2.04)
8	(0.6, 0.6)	(7.5, 6.12)	(0.6, 0.3)	(7.5, 3.061)
9	(0.8, 0.4)	(5, 13.33)	(0.7, 0.25)	(4.37, 8.33)
10	(0.8, 0.6)	(5, 8.57)	(0.2, 0)	(1.25, 0)
11	(0, 0.1)	(0, 0.71)	(0.4, 0.3)	(2.5, 2.14)
Average Deviation	(0.854, 0.49)	(5.91, 7.36)	(0.61, 0.22)	(4.48, 5.26)

5.6 Conclusions

In this chapter, it is clearly demonstrated that a multipoint measurement fibre optic, FBG-based sensor system has been successfully developed and evaluated in this work. The work has shown a successful continuation of work using glass plate as a standardized test reported in the Chapter 4. Based on the acoustic signals received by both the optical and PZT sensors, the acoustic source location has been successfully determined using the triangulation method and a very good agreement has been reached. The small deviation seen between the results with the two methods can be attributed to small differences in the two experimental conditions causing factors such as the mobility of the lifting surface, movement of the sonotrode to give slightly different calculate results.

The work shows clearly that the frequency content of the signals captured by both types of sensors are very similar, as a common prime frequency component has been accurately detected, with that matching well the known excitation frequency from the sonotrode, within the uncertainty of the measurement. The maximum uncertainty was 12 mm which was observed at the point 5 which was very close to the edges of the half-rudder and the water tank walls. The success of this preliminary research is encouraging for the use of FBG-based sensors for this important practical application. Thus the light weight, easily multiplexed sensors, immunity to EMI are the benefits of the use of fibre optic sensors that make them applicable to this work which was a key purpose in doing the experiments explained in the text.

Chapter 6

Fibre Bragg Grating-based sensor system for condition monitoring of electrified railway pantograph

6.1 Introduction

A pantograph, or so called a current collector is mounted on the roof of the train, tram or electric bus with the main purpose to ensure an appropriate current collection from Overhead Line Equipment (OLE). It is necessary to ensure the contact between the OLE and pantograph in order to provide reliable train operation [200]. The pantograph used for the experiments in this work is manufactured by Faiveley Brecknell Willis, and it is shown in Fig. 6.1.



Figure 6.1 Pantograph designed and manufactured at Brecknell Willis

The main aim of this chapter is to report the development of a smart pantograph integrated with a FBG-based sensor array for monitoring its contact force and contact location against the overhead wire. Currently, pantographs are designed as passive and there is no feedback control. The interface between contact wire and pantograph, however, is affected by mechanical, dynamic, aerodynamic effects as the train is moving at high speeds. Thus it is of critical

importance to have the real-time information of the contact conditions of this critical infrastructure.

This chapter is structured as follows: it begins with a review of monitoring techniques reported for pantograph condition monitoring. It is followed by the discussions of the experimental setup used for measurement of contact force, contact location and temperature compensation and the results obtained from extensive experimental evaluation of the smart pantograph.

6.2 Need and techniques for remote pantograph monitoring

Considering the rapid development of the high-speed electrified railway and the speed of operation being constantly increased, there is a need to ensure that limiting factors to this are reduced to a minimum. One of the key factors limiting the speed of trains and reliable train operation is related to the quality of current delivery from catenary systems to pantograph, hence catenary-pantograph interface monitoring becomes of critical importance. The key parameter typically considered to assess the good quality of the pantograph-catenary interaction is the contact force between these two systems. In most of the cases the standard nominal force on this interface is required to be 90N and if the force is lower than that, there is a power loss and the phenomena that occurs is called ‘arcing’ [201]. This phenomena causes a contact loss and high values of wear. In AC traction, sharp transients are generated during the current zero crossings (CZCs) due to the arcing effect. The sinusoidal waveform is distorted, causing an asymmetry between the two polarities of the supply voltage and current, which drives a net DC current from the contact wire to the train [202]. Pantograph arcing also radiates electromagnetic waves in a wide band, which causes interference with different radio based communication systems. Both of these effects lead to arcing in the air gap on the catenary-pantograph interface. Ding *et al* have reported that the wear rate of carbon with arc discharge is much larger than without it [203]. On the other hand, if the contact force is higher than required, increased mechanical friction leads to severe wear of the carbon strips and resulting in a shortened lifetime of a pantograph. Considering that this interaction between the pantograph and catenary is not constrained within an acceptable range, in some extreme cases, apart from high maintenance cost serious structural damages can occur [204]. So, the pantograph-catenary interface is one of the most critical parts in electrified train operation as it can directly affect the cost of infrastructure and maintenance, as well as limit the operational speed unless monitored appropriately.

Chapter 6: Fibre Bragg Grating-based sensor system for condition monitoring of electrified railway pantograph

One of the main technical challenges arises from the very harsh working conditions, considering the speed at which trains move and the fact that high-speed trains are powered with 25 kV AC. If traditional sensors, such as load cells or strain gauges were used in this environment to measure contact force on the interface between pantograph and catenary, adequate electrical insulation is required due to the high electromagnetic interference. Considering the electrical insulation as an option, the whole measurement system becomes very complex, more expensive and due to the added mass to the pan-head, the measurement error would significantly increase and the whole system would be of no use in a real time train operation.

Another technique that has been reported for contact force measurement on the interface between pantograph and overhead line is based on image processing technology. The authors have measured the contact force as a result of displacement measurement between panhead and panhead support. In other words, the product of the spring coefficient and the spring deformation corresponds to a relative displacement between panhead and the panhead support. In order to provide this measurement, particular markers with black stripes are installed on the surface of the panhead and the panhead support as a target for an image capture camera. Images of these markers are taken by line sensor cameras with high time and spatial resolution. One line sensors camera captured images of two markers installed on the surface of the panhead and the pantograph support to evaluate spring reaction force of the panhead supporting springs and the inertial force at the centre of the panhead [205]. The other line sensor camera took images of the marker installed on the surface of the panhead to evaluate the inertial force on the side of the panhead.

Doyle *et al* [206] have reported a technique which combines lasers and computer vision technology to provide an analysis of the condition of pantographs on electrified rolling stock during the operation. The technique proposed takes three types of measurement when inspecting the pantograph; carbon strip profile, pantograph geometry and uplift displacement. In order to profile the shape of the carbon strip, three laser lines are projected across the length of the carbon. These lasers produce light at the precise wavelength and that light is captured by the precise camera matched to the wavelength of the lasers. In this case the image of the carbon strip profile is generated. The relative position of the carbon strip profile in the image is used to calculate the uplift position of the pantograph which could be used for the uplift contact force measurement. The disadvantage of this system is that it only monitors the condition of

Chapter 6: Fibre Bragg Grating-based sensor system for condition monitoring of electrified railway pantograph

the pantograph at the certain points of the railway track, rather than providing a true real time monitoring system [206].

In order to overcome the issues mentioned above, optical fibre based sensors can be used. They have shown advantages over their electrical counterparts due to their intrinsic insulating properties, small size and light weight, and the ability to be easily integrated into pantograph. The advantages of optical fibre based sensors have been reported in the Chapter 3.

Regarding optical fibre based sensing systems, two main techniques for pantograph monitoring have been reported so far, such as the fibre Bragg grating (FBG) based approach and interferometric based approach. One of the main challenges when FBG techniques is applied is how to provide an adequate temperature compensation mechanism due to the well-known cross-sensitivity of FBG sensors to both strain and temperature changes. Considering this issue, there are several research groups and institutes that have palced effort to overcome this challenge and provide an accurate measurement system for the contact force measurement on the critical pantograph-catenary interface.

The most commonly reported approach for temperature compensation, when FBG sensors are used is deploying an additional FBG sensor which has very low or zero strain sensitivity. Camolli *et al* have reported the use of two fibres, where each fibre had one FBG. The FBG used for temperature compensation is installed in orthogonal direction in comparison with strain measurement and at a position where the strain values are the lowest which is 20 cm from the strain sensors [207]. The sensors layout proposed by this research group is shown in Fig. 6.2.

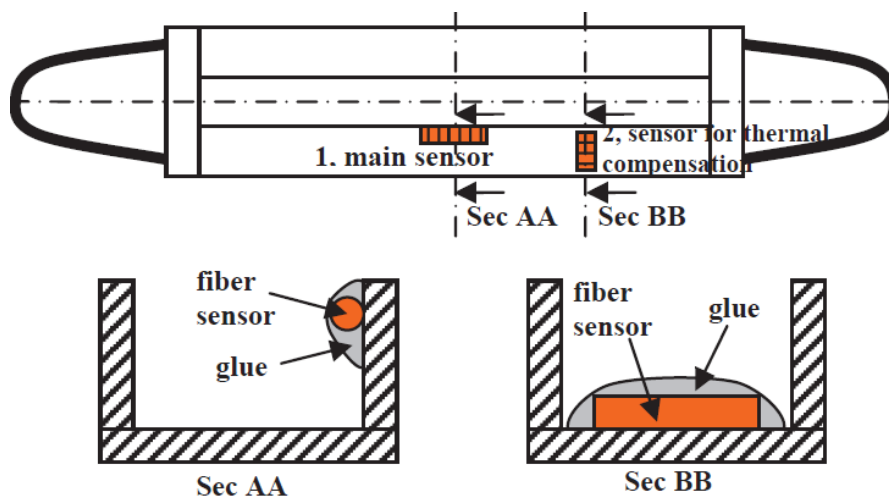


Figure 6.2 FBG sensor positioning and instrumentation methods [207].

Chapter 6: Fibre Bragg Grating-based sensor system for condition monitoring of electrified railway pantograph

In Fig. 6.2, The ‘main sensor’ refers to the sensor used for the strain measurement and the work is based on the assumption that temperature distribution is uniform along the current collector which is not necessarily the case in reality and as a consequence it might induce large errors in measurement.

Schroder *et al* [208] have reported the design where FBG sensors are embedded between carbon and aluminium part for defect monitoring on a railway catenary. This was achieved by measuring short time force changes in vertical and horizontal direction on the pantograph-catenary interface. A ‘strain-free’ sensor was used for temperature measurement and thus for temperature compensation. The results reported are obtained from laboratory tests at a constant room temperature.

Wagner *et al* [209] have reported a method using packaged FBG sensors in an aluminium box, which is not only used to protect the sensors from the harsh environment, but also to ensure a small sensor footprint. Each aluminium box contained 3 FBG sensors, where 2 of them are used for force measurement and one sensor is instrumented in a similar configuration as reported above [208]. Each current collector is instrumented with two aluminium boxes and the box with FBG sensors inside is shown in Fig. 6.3.



Figure 6.3 FBG force sensor with additional FBG for temperature compensation [209].

Considering the presence of aerodynamic force when train is moving at a high speed, having additional 4 aluminium boxes attached to the pantograph would significantly increase the mass of the system and cause undesirable error in measurement of the contact force.

Schroder *et al* have recently reported the use of anti-symmetric sensors with equal strain responses, but opposite sign of the two single strain sensors. In the case reported the force is

calculated from the difference in the readouts and the temperature is calculated from their sum [210].

In addition to the FBG-based sensor systems reported above, Boffi *et al*, have used a interferometric approach based on Mach-Zhender configuration to achieve a distributed force measurement of a pantograph [211].

All of the reported FBG techniques require either an additional fibre or and additional FBG sensors for temperature compensation in such an environment in which pantograph operates. Given the higher temperature sensitivity of a FBG sensor, which is one order of magnitude higher than that of its strain sensitivity, the main challenge of this research is to remove the temperature effect in an effective way, yet keeping the whole system as simple as possible.

6.3 FBG-based pantograph condition monitoring system

FBG sensors that have been used in this work and the main part of the sensing system were reported in more detail in Chapter 3. The schematic diagram of the FBG array used in this work is shown in Fig. 6.4. Each pan-head of the current collector is instrumented with 9 FBG sensors in an array. The sensor data were captured using a Micron Optics sm130 interrogator and processed using an algorithm carefully designed and developed at City, University of London, with an aim to remove completely the temperature effect. The details of the sensor layout and the algorithm developed for temperature compensation have been included in a patent filed in early 2017 [212].

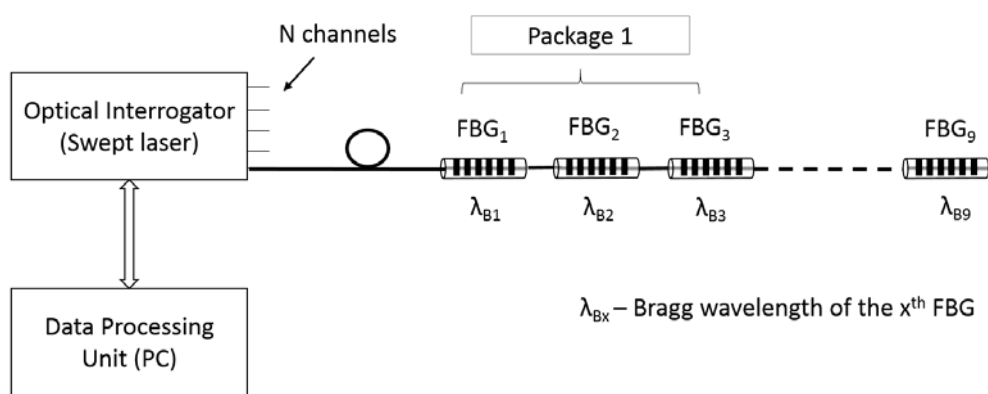


Figure 6.4 Demonstration of an FBG array used for pantograph instrumentation and interrogation setup

9 FBG sensors are grouped into three FBG packages creating the same footprints which are installed at the bottom of the pan-head using epoxy resin. The packages are installed at three locations, in the central region, and at the equal distance on the right and left side from the

centre. The three packages are used for measurement of both contact force and contact location and temperature compensation.

6.4 Temperature compensated contact force measurement

In order to verify the functionality of proposed system and correct contact force measurement on the pantograph-catenary interface, a tailored experimental setup is designed. There are many ways that heating could be provided to the pantograph pan-head using various heating sources. One of the methods used to vary the temperature applied on the pantograph pan-head is to change the current directly applied on the pantograph strips. This experiment was undertaken jointly with colleagues at Faiveley Brecknell Willis and the experimental setup is shown in Fig. 6.5.

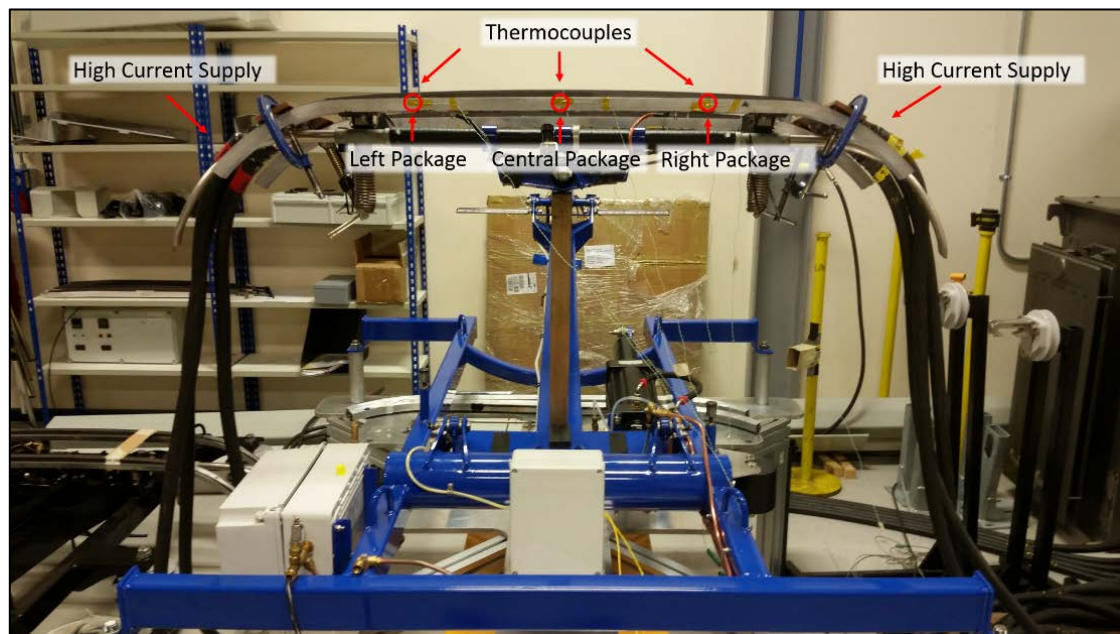


Figure 6.5 Pantograph connected to DC current supply with current change from 0 to 1500A and then from 1550A to 0A, when contact force is zero

As shown in Fig. 6.5, the current supply was connected to both sides of the pantograph, allowing for a step change of current from 0 to 1500A and then return to 0. By applying high current to the pantograph, the temperature changes were induced in the range from 25°C to 55°C over a period of 9 minutes. The temperature changes have been recorded by three thermocouples, which were co-located with 3 FBG packages as shown in Figure 6.4. Once the temperature reached 55°C, the industrial fans have been used to speed up the cooling process. It is important to mention that there was no contact force applied to the pantograph during the experiment.

Chapter 6: Fibre Bragg Grating-based sensor system for condition monitoring of electrified railway pantograph

Figure 6.6 shows the current applied and the temperature measured using thermocouple co-located with the FBG package in the central region of the pantograph. The current supply is switched off when the temperature measured by the thermocouple reached 55°C and a fan was used to accelerate the cooling process.

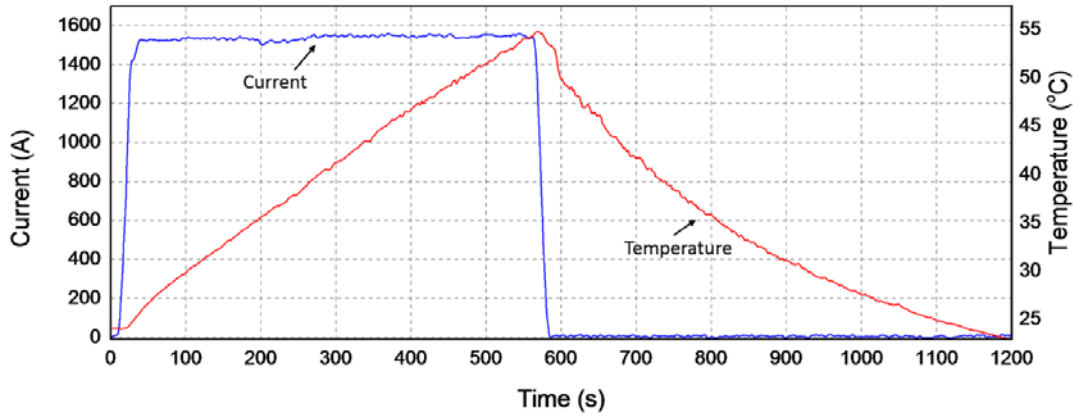
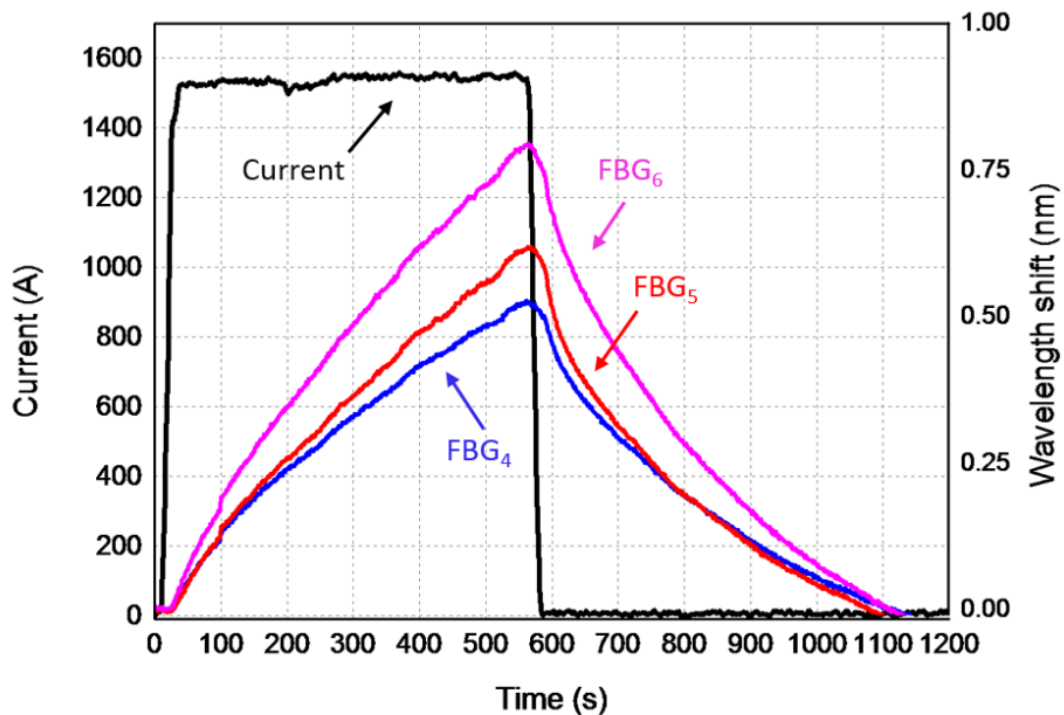


Figure 6.6 Temperature change recorded by the central thermocouple and current value applied to the pantograph during the experimental tests

As well as the data recorded by the thermocouple placed in a central region of the pantograph, the wavelength shifts recorded by three FBGs from a central package, FBG₄, FBG₅ and FBG₆, and this is shown in Fig. 6.7. The wavelength shifts are recorded when a step change of current is applied to a pantograph from 0 to 1500A and then from 1500A to 0. The wavelength shift of each FBG within the same package experiences the change in applied strain (from contact force which is zero in this test) and in temperature.



Chapter 6: Fibre Bragg Grating-based sensor system for condition monitoring of electrified railway pantograph

Figure 6.7 Wavelength shifts recorded from FBGs 4, 5 and 6 in the central package recorded during the experimental tests

It is clear that the wavelength shifts of all the gratings in this test were not caused by the applied force (zero in this scenario), but by temperature variation induced by the applied current. Using the algorithm developed based on the correlation between packages, it is evident that the temperature effect has been fully removed (red curve), as shown in Figure 6.8.

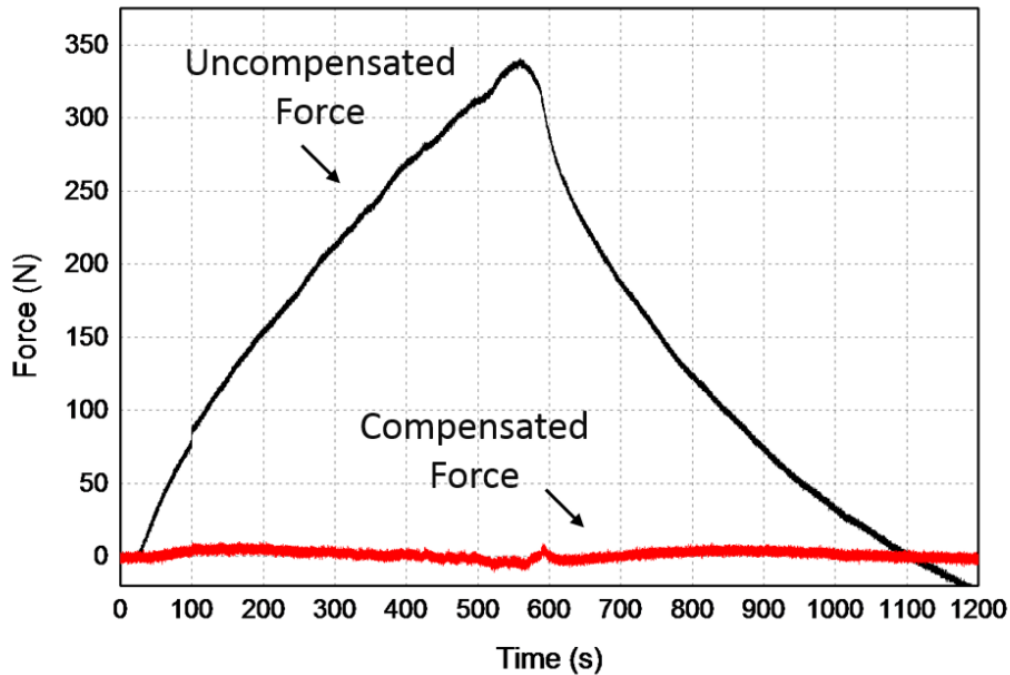


Figure 6.8 Contact force measured by FBG packages before and after temperature compensation algorithm

The same approach is applied on the other two FBG packages. Further to the above temperature-compensated contact force measurement using each FBG package, the contact location of the OLE against pantograph can be obtained by calculating the ratio of the contact forces measured simultaneously by the three FBG packages integrated into the pantograph at three different locations.

Considering the functionality of the algorithm and successful completion of the experiments in the laboratory environment, further tests were completed on the real train where contact force and contact location were measured. The following figure shows the train on which the instrumented pantograph was installed.



Figure 6.9 Test train trials in collaboration with the Rail Alliance

The number of tests are completed measuring both contact force and contact location between pantograph and overhead line. The contact force measured is shown in Fig. 6.10.

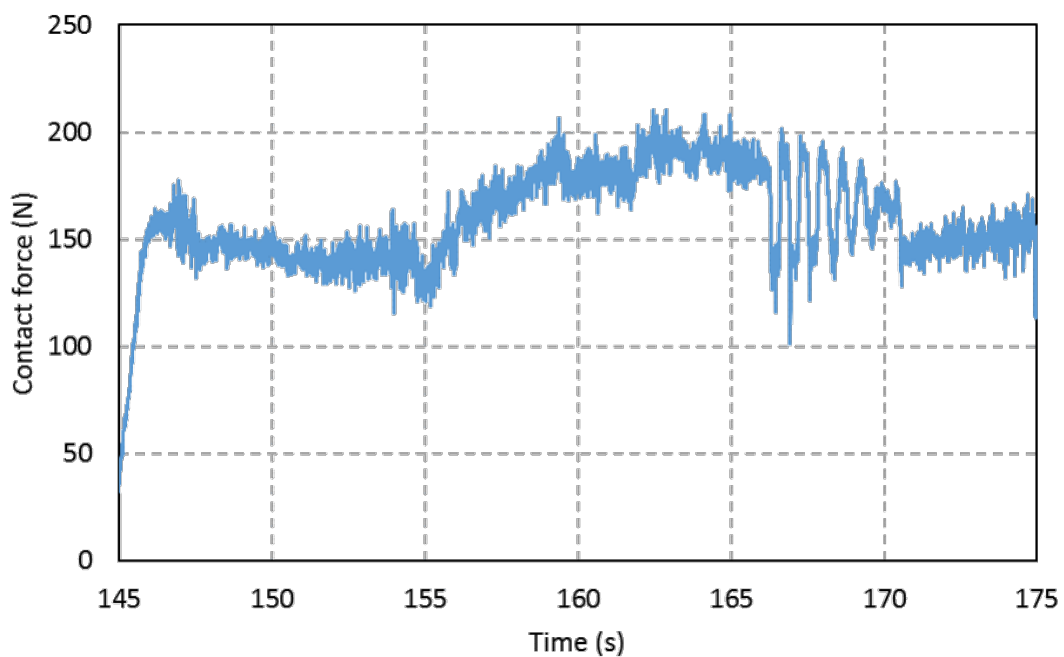


Figure 6.10 Contact force measured by developed FBG-sensor system while train was moving

The corresponding contact location data is shown in Fig. 6.11 and it is measured with the respect to the centre of the pan-head, where can be observed that overhead line mainly sweeps in the range of 40 cm on the pan-head.

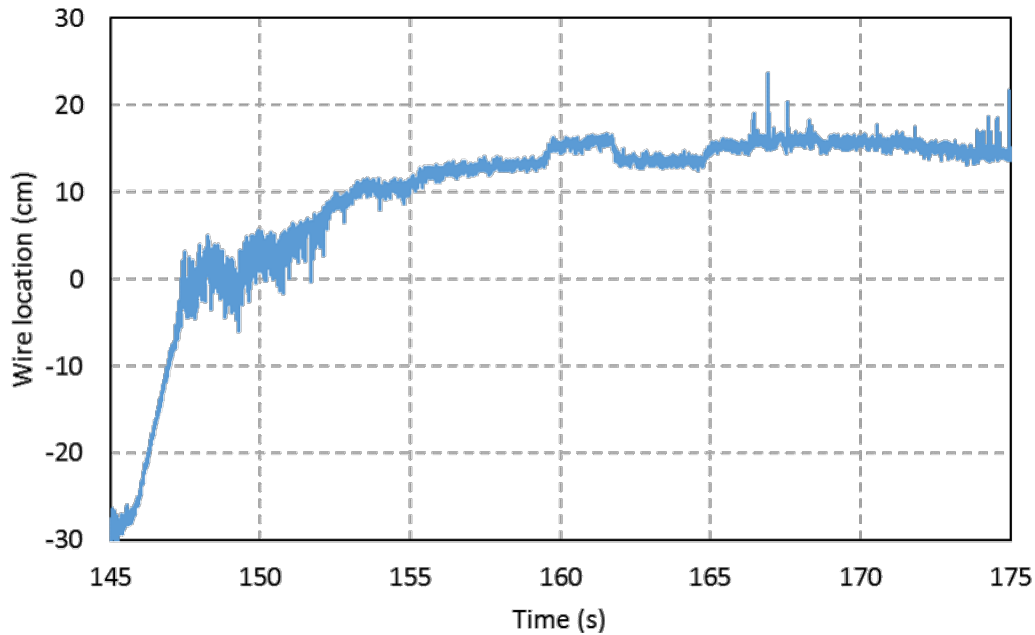


Figure 6.11 Contact location measured while train is running

6.5 Summary

The work reported in this chapter has clearly demonstrated a novel sensor design through integration of FBG sensor packaged into a railway current collector for its remote condition monitoring which is becoming critical for the train operation. The sensor system and the FBG packages are designed with the main goal to remove temperature effect in the strain/force measurement and under the circumstances that the temperature effect is more dominant.

The positive outcomes obtained from an industrial laboratory tests, by driving the pantograph using high currents, have confirmed the effectiveness of the method developed and successfully applied for the temperature compensation. In order to verify the effectiveness of the whole system in a real time situation, more vehicle tests will be undertaken in the near future to provide an extensive evaluation of the smart pantograph developed.

Chapter 7

Conclusions and Future Work

7.1 Conclusions of the work carried out

In this research, the main focus has been on the development of a set of novel FBG-based sensor systems that were designed for potential applications in NDT methods, for a range of topical industrial applications where there are advantages from the use of an optical method of measurement to overcome measurement problems with conventional sensors. To give confidence in these new sensors, their performance and characteristics have been cross-compared with those of conventional sensors, both in the laboratory and on some occasions in the industrial environment, in order to demonstrate their effectiveness and gave potential users the data on which they can base a decision on using these new sensors.

Looking at specific work done and reported in the thesis, the FBG-based system developed for marine applications has been validated by cross-comparison with conventional PZT sensors, looking at acoustic emission detection on a marine rudder. In addition to that, an FBG-based sensor array, integrated into a working railway pantograph has shown to be able to achieve accurate contact force measurement with effective temperature compensation having been successfully achieved – this overcoming a long-standing problem of integrating sensors in such a pantograph and making direct measurements. The work has reported a number of key achievements both to industry through reports and in work published in the open international literature, and these can be summarized as:

- A comprehensive review of both conventional NDT methods and fibre Bragg grating-based sensors has been given. It covers the background, sensing principles and applications where these methods have been applied. The analysis of that prior published work has formed a sound basis for the intensive research then carried out to develop new methods and create specific acoustic sensors for monitoring marine lifting surfaces (the marine rudder) and for accurate force/location sensors for railway pantographs, for the first time with this intrinsically-safe approach.
- The successful development of FBG-based acoustic sensor array for acoustic emission detection. Their performance, in comparison with conventional PZT sensors, has been

extensively evaluated by subjecting the testing object (glass, metal and marine lifting surface) to various acoustic excitations. A good agreement between the various methods used has been reached, showing the promise of such sensors for acoustic detection by industry.

- The triangulation method has been successfully deployed to analyse the acoustic signals captured by FBGs in order to identify the location of the acoustic source in the above marine application. Again this method has shown real promise for future identification of faults/cracks in marine structures. In addition, the use of FBG array has shown the advantage over conventional technology of achieving simultaneous multi-point detection using a single length of fibre, which enables the whole measurement system to be compact (and indeed well suited to operation in water) and thus suitable for retrofitting or being embedded into structures for remote monitoring.
- The successful development of a smart pantograph by integration of three FBG array packages into the structure for the accurate and direct measurement of contact force and contact location. The measurement approach and the sensor efficacy has been successfully validated at Faiveley Brecknell Willis, in tests carried out by industry by applying varying electrical current to the pantograph to vary its temperature yet keeping the contact force to be zero. The algorithm developed to link to the experimental work, specifically for temperature compensation, has been deployed and the experimental validation has been successful. This approach, developed after considerable experimentation, has proven that the changing temperature seen in normal operation of a pantograph is no longer a challenge for practical use in this particular application – where the effect on the sensor due to temperature changes is eliminated through careful instrumentation and algorithm development, carried out in association with and to meet the demands of industry.
- The positive research outcomes achieved have been widely disseminated to the community, via three peer-reviewed journal papers and five international conference papers. In addition, a new patent that contains the key information of the smart pantograph instrumentation and temperature compensation algorithms was filed in January 2017.

7.2 Future work – potential wider applications of the technologies developed

The extensive work done has shown both the effectiveness of the sensor schemes developed and the direction for future work which can exploit further the use of optical techniques, based on optical fibre sensors, to meet the demands of industry for better sensing. Thus this work has opened up a wide vista of potential applications in a number of areas of technology, but limiting this to the topics discussed in this thesis, the suggestions for the future work are based on the specific work reported in this thesis, the results obtained and the need for better NDT methods for structural health monitoring, for various industrial applications. Thus areas where future work in this field seem likely to offer real benefit include:

- On-going work to refine the design and layout of the sensors on a full scale marine lifting surface which is much larger in size than the model tested as part of this work. The work done suggests that this should be relatively easy to do, but the scale of the marine surface may therefore need a greater number of sensors to be interrogated at any one time.
- Improvement of the signal to noise ratio (SNR): this is seen as one of the main challenges due to the comparatively low sensitivity of such sensors to very weak surface wave propagation in the structure. Several options for this are suggested:
 - Optical amplification using an erbium doped fibre amplifier (EDFA) to increase the optical signal in the sensor system
 - Optimization of the bonding between the sensors and the target structure, allowing for the maximum capture of the acoustic wave and longer term testing to see if problems arise in any particular environments or if better glues/adhesives can be used.
 - The development of a simulation model, taking into account several key factors, such as excitation source frequency, thickness of an adhesive layer and bonding length to allow for the better and more advanced design of sensor systems for such applications. This will enable the system optimization both in terms of the sensitivity and of the sensing range from kHz to MHz and thus aim for better performance.
- In addition to the static force measurement discussed in the thesis, inertia and aerodynamic contact forces are also required to be measured, in particular for high speed rail applications. Therefore work on optical fibre accelerometers and flowmeters

is required to be developed to facilitate such measurements and improve on conventional measurements, to overcome problems for difficult environments.

7.3 References

- [1] Fahr, Abbas, (2014). Aeronautical applications of non-destructive testing. ISBN: 9781605951201. *DEStech Publicaions*
- [2] Mix, E. P., (2005) Introduction to Nondestructive Testing, A Training Guide :Emissions, A. (n.d.). Acoustic emissions. 2, 15–64.
- [3] Lim, M. K., & Cao, H. (2013). Combining multiple NDT methods to improve testing effectiveness. *Construction and Building Materials*, 38, 1310–1315.
- [4] J. F. Franc and J. M. Michel. (2004). Fundamentals of Cavitation, 76(0), 6221.
- [5] Glisic, B., Inaudi, D., & Casanova, N. (2010). SHM process as perceived through 350 projects. *Proceedings of SPIE The International Society for Optical Engineering*, 7648, 76480–76488.
- [6] Lopez-Higuera, J. M., Rodriguez Cobo, L., Quintela Incera, A., & Cobo, A. (2011). Fiber Optic Sensors in Structural Health Monitoring. *Journal of Lightwave Technology*, 29(4), 587–608.
- [7] Shiotani, T. (2006). Evaluation of long-term stability for rock slope by means of acoustic emission technique. *NDT & E International*, 39(3), 217–228.
- [8] Utagawa, M., Seto, M., & Katsuyama, K. (1997). Estimation of initial stress by deformation rate analysis (DRA). *International Journal of Rock Mechanics and Mining Sciences & Geomechanics Abstracts*, 34(3-4), 501.
- [9] Behnia, A., Chai, H. K., & Shiotani, T. (2014). Advanced structural health monitoring of concrete structures with the aid of acoustic emission. *Construction and Building Materials*, 65, 282–302.
- [10] Wild, G., & Hinckley, S. (2011). Acousto-Ultrasonic Optical Fiber Sensors : Overview and State-of-the-Art Acousto-Ultrasonic Optical Fiber Sensors : Overview and State-of-the-Art, 8(2008), 1184–1193.
- [11] Liu, Z. (2003). Evaluation of Reinforced Concrete Beams Using Cyclic Load Test, Acoustic Emission and Acousto-Ultrasonics.
- [12] Essay, S. H. (2011). General Information About Piezoelectric Sensors. *Piezoceramic Sensors, Chapter 1*.
- [13] Lowe, M. J. S., Alleyne, D. N., & Cawley, P. (1998). Defect detection in pipes using guided waves. *Ultrasonics*, 36(1-5), 147–154.
- [14] Kundu, T., Maji, a., Ghosh, T., & Maslov, K. (1998). Detection of kissing bonds by Lamb waves. *Ultrasonics*, 35(8), 573–580.
- [15] Core, C. (2016). *Waves in Plates*, Cambridge Core Publishing, Chapter 6.
- [16] Moll, J., & Fritzen, C. P. (2012). Guided waves for autonomous online identification of structural defects under ambient temperature variations. *Journal of Sound and Vibration*, 331(20), 4587–4597.
- [17] Wagner, R., Goncalves, O., Demma, A., & Lowe, M. (2013). Guided wave testing performance studies: comparison with ultrasonic and magnetic flux leakage pigs. *Insight*,

References

55(4), 187–196.

[18] Demma, A., Cawley, P., Lowe, M., Roosenbrand, A. G., & Pavlakovic, B. (2004). The reflection of guided waves from notches in pipes: a guide for interpreting corrosion measurements. *NDT & E International*, 37(3), 167–180.

[19] Gutiérrez-Hernández, H. E., Rendón, P. L., & Marchiano, R. (2016). Theoretical study of the generation of screw dislocations for Rayleigh and Lamb waves in isotropic solids. *Wave Motion*, 62, 55–62.

[20] Rose, J. L. (2004). Ultrasonic guided waves in structural health monitoring. *Key Engineering Materials*, 270-273, 14–21.

[21] De Billy, M., Adler, L., & Quentin, G. (1983). Measurements of backscattered leaky Lamb waves in plates. *J. Acoust. Soc. Am.*, 75(3), 998–1001.

[22] Leduc, D., Hladky, A.-C., Morvan, B., Izbicki, J.-L., & Pareige, P. (2005). Propagation of Lamb waves in a plate with a periodic grating: Interpretation by phonon. *The Journal of the Acoustical Society of America*, 118(4), 2234.

[23] Zheng-guang, Y., & Ping, Y. E. (2010). Design of Electromagnetic Acoustic Transducer for Wheel Flaw Detection. *Mechanic Automation and Control Engineering* .

[24] [Hirao, M., Ogi, H.,(2016). EMATs for Science and Industry : Noncontacting Ultrasonic Measurements. *Springer, Classical Continuum Physics*.

[25] Cheng, Y., Deng, Y., Cao, J., Xiong, X., Bai, L., & Li, Z. (2013). Multi-wave and hybrid imaging techniques: a new direction for nondestructive testing and structural health monitoring. *Sensors*, 13.

[26] Suchkov, G. M. (2000). The Main Advantage of Electromagnetic-Acoustic Testing Technique. *Acoustic Methods*, 36(10), 760–762.

[27] Finkel, P., & Godinez, V. (2004). Electromagnetic stimulation of the ultrasonic signal for nondestructive detection of ferromagnetic inclusions and flaws. *IEEE Transactions on Magnetics*, 40(4 II), 2179–2181.

[28] Vitaly, I.; Alexander, V. (2008). Development of Instruments for NDT of Rail-Tracks with Use of Contactless Electromagnetic Acoustic Emission Transducers (EMATs). *17th World Conference on Nondestructive Testing*.

[29] Yi, Z., Kaican, W., Lei, K., Guofu, Z., & Shujuan, W. (2010). Rail flaw detection system based on electromagnetic acoustic technique. *Proceedings of the 2010 5th IEEE Conference on Industrial Electronics and Applications, ICIEA 2010*, 211–215.

[30] Fei Yan, Royer, R. L., & Rose, J. L. (2010). Ultrasonic Guided Wave Imaging Techniques in Structural Health Monitoring. *Journal of Intelligent Material Systems and Structures*, 21(3), 377–384.

[31] Kak, A., & Slaney, M. (1988). Principles of Computerized Tomographic Imaging. *Engineering*, 344.

[32] Wright, W., Hutchins, D., Jansen, D., & Schindel, D. (1997). Air Coupled Lamb Wave Tomography. *IEEE Transactions and Ultrasonics*, 44(1), 53 -59.

[33] McKeon, J. C. P., & Hinders, M. K. (1999). Parallel projection and crosshole Lamb wave contact scanning tomography. *The Journal of the Acoustical Society of America*, 106(5), 2568.

References

- [34] Malyarenko, E. V., & Hinders, M. K. (2000). Fan beam and double crosshole Lamb wave tomography for mapping flaws in aging aircraft structures. *The Journal of the Acoustical Society of America*, 108(4), 1631–1639.
- [35] Monnier, T. (2006). Lamb Waves-based Impact Damage Monitoring of a Stiffened Aircraft Panel using Piezoelectric Transducers. *Journal of Intelligent Material Systems and Structures*, 17(5), 411–421.
- [36] Breon, L. J., Rose, J. L., & Xu, C. (2008). Guided Wave Thickness Measurement Tomography for Structural Health Monitoring in Critical Zones of Pipelines. *17th World Conference on Nondestructive Testing*.
- [37] Van Velsor, J. K., Gao, H., & Rose, J. L. (2007). Guided-wave tomographic imaging of defects in pipe using a probabilistic reconstruction algorithm. *Insight: Non-Destructive Testing and Condition Monitoring*, 49(9), 532–537.
- [38] Wilcox, P. D. (2003). Omni-directional guided wave transducer arrays for the rapid inspection of large areas of plate structures. *IEEE Transactions on Ultrasonics, Ferroelectrics, and Frequency Control*, 50(6), 699–709.
- [39] Giurgiutiu, V. (2005). Tuned Lamb Wave Excitation and Detection with Piezoelectric Wafer Active Sensors for Structural Health Monitoring. *Journal of Intelligent Material Systems and Structures*, 16(4), 291–305.
- [40] Fromme, P., Wilcox, P. D., Lowe, M. J. S., & Cawley, P. (2006a). On the development and testing of a guided ultrasonic wave array for structural integrity monitoring. *IEEE Transactions on Ultrasonics, Ferroelectrics, and Frequency Control*, 53(4), 777–784.
- [41] Gonzalez, C., Reyna, R., & Chitty, J. (2012). Ultrasonic Thermal Imaging. *Nondestructive Testing*, (April), 1–3.
- [42] Sakagami, T., Kuroki, K., & Kubo, S. (2009). Detection of Stress Corrosion Cracking by Sonic-IR Technique. *Proceedings of the 4th annual meeting of Japan Society of Maintenance*.
- [43] Favro, L. D., Thomas, R. L., Han, X., Ouyang, Z., Newaz, G., & Gentile, D. (2001). Sonic infrared imaging of fatigue cracks. *International Journal of Fatigue*, 23, 471–476.
- [44] Xu, W., Shen, J., & Zhang, C. (2008). Ultrasonic infrared thermal wave nondestructive evaluation for crack detection of several aerospace materials. *Proceedings of SPIE*, 6835(2007), 1–8.
- [45] Mandelis, A. (2002). Photothermal Diagnostic Technologies. *Opt. Photon. News*, 13(6), 32–37.
- [46] Tolev, J., & Mandelis, A. (2010). Laser photothermal non-destructive inspection method for hairline crack detection in unsintered automotive parts: A statistical approach. *NDT and E International*, 43(4), 283–296.
- [47] Cheng, L., & Tian, G. Y. (2012). Pulsed electromagnetic NDE for defect detection and characterisation in composites. *2012 IEEE I2MTC - International Instrumentation and Measurement Technology Conference, Proceedings*, 1902–1907.
- [48] Weekes, B., Cawley, P., Almond, D. P., & Li, T. (2010). The effect of crack opening on thermosonics and laser-spot thermography. *AIP Conference Proceedings*, 1211(1).
- [49] Burrows, S. E., Rashed, A., Almond, D. P., & Dixon, S. (2007). Combined laser spot

References

- imaging thermography and ultrasonic measurements for crack detection. *Ndte*, 22(2-3), 217–227.
- [50] Zakrzewski, J., Chigarev, N., Tournat, V., & Gusev, V. (2010). Combined photoacoustic-acoustic technique for crack imaging. *International Journal of Thermophysics*, 31(1), 199–207.
- [51] Abraham, O., Popovics, J. S., Cottineau, L.-M., & Durand, O. (2011). Laser ultrasonics for civil engineering : some applications in development for concrete non destructive testing. *Journal of Physics: Conference Series*, 278(1), 12014.
- [52] Gryzagoridis, J., & Findeis, D. (2006). ESPI of Aerospace Composites Using Digital Shearography.
- [53] Viotti, M. R., Albertazzi, J. A., & Kaufmann, G. H. (2005). Measurement of residual stresses using local heating and a radial in-plane speckle interferometer. *Optical Engineering*, 44(9), 93606–93609.
- [54] Tsopeles, N., & Siakavellas, N. J. (2006). Electromagnetic-thermal NDT in thin conducting plates. *NDT and E International*, 39(5), 391–399.
- [55] He, Y., Tian, G., Cheng, L., Zhang, H., & Jackson, P. (2011). Parameters influence in steel corrosion evaluation using PEC thermography. *The 17th International Conference on Automation and Computing*, 255–260.
- [56] Kumar, C. N. K., Krishnamurthy, C. V., Maxfield, B. W., & Balasubramaniam, K. (2008). Tone burst eddy-current thermography (tbet). *AIP Conference Proceedings*, 975(1).
- [57] Noethen, M., Wolter, K. J., & Meyendorf, N. (2010). Surface crack detection in ferritic and austenitic steel components using inductive heated thermography. *ISSE 2010 - 33rd International Spring Seminar on Electronics Technology: Polymer Electronics and Nanotechnologies: Towards System Integration - Conference Proceedings*, 249–254.
- [58] Wu, J., Zhou, D., Wang, J., Guo, X., You, L., An, W., & Zhang, H. (2014). Surface crack detection for carbon fiber reinforced plastic (CFRP) materials using pulsed eddy current testing. *2014 IEEE Far East Forum on Nondestructive Evaluation/Testing*, 11(12), 181–185.
- [59] Estes, A. C., & Frangopol, D. M. (2003). Updating Bridge Reliability Based on Bridge Management Systems Visual Inspection Results. *Journal of Bridge Engineering*, 8(6), 374–382.
- [60] Jahanshahi, M. R., Kelly, J. S., Masri, S. F., & Sukhatme, G. S. (2009). A survey and evaluation of promising approaches for automatic image-based defect detection of bridge structures. *Structure and Infrastructure Engineering*, 5(6), 455–486.
- [61] Lee, B. J., Shin, D. H., Seo, J. W., Jung, J. D., & Lee, J. Y. (2011). Intelligent Bridge Inspection Using Remote Controlled. *2011 Proceedings of the 28th ISARC, Seoul, Korea*, 1426–1431.
- [62] Moller, P. (2008). CALTRANS Bridge Inspection Aerial Robot Report No. CA08-0182.
- [63] Shen, H.-K., Chen, P.-H., & Chang, L.-M. (2013). Automated steel bridge coating rust defect recognition method based on color and texture feature. *Automation in Construction*, 31, 338–356.
- [64] S K Ho et al. (1990). A vision system for automated crack detection in welds. *Measurement Science and Technology*, 1(3), 287.

References

- [65] Gonzales. (2014). Digital image processing using MATLAB. *Igarss 2014*, (1), 1–5.
- [66] Gola, B. (2014). Penetration tests of historical metal structures. *Welding International*, 28(3), 169–173.
- [67] Kogan, L. K., Nichipuruk, A. P., & Gavrilova, L. D. (2006). Effect of the carbon content on the magnetic and electric properties of thermally treated carbon steels and the possibilities of testing the quality of tempering of articles produced from them via the eddy-current method. *Russian Journal of Nondestructive Testing*, 42(9), 616–629.
- [68] Mercier, D., Lesage, J., Decoopman, X., & Chicot, D. (2006). Eddy currents and hardness testing for evaluation of steel decarburizing. *NDT & E International*, 39(8), 652–660.
- [69] Rajkumar, K. V., Rao, B. P. C., Sasi, B., Kumar, A., Jayakumar, T., Raj, B., & Ray, K. K. (2007). Characterization of aging behaviour in M250 grade maraging steel using eddy current non-destructive methodology. *Materials Science and Engineering A*, 464(1-2), 233–240.
- [70] Kersey, A. D. (1996). A Review of Recent Developments in Fiber Optic Sensor Technology. *Optical Fiber Technology*, 2 (3), 291 - 317.
- [71] Grattan, K. T. V., & Sun, T. (2000). Fiber optic sensor technology: An overview. *Sensors and Actuators, A: Physical*, 82(1), 40–61.
- [72] Culshaw, B. (2000). Fiber optics in sensing and measurement. *IEEE Journal on Selected Topics in Quantum Electronics*, 6(6), 1014–1021.
- [73] Yio, S., Ruffin, P. B., Yu, F. T. S., & Yin, S. (2008). Fiber Optic Sensors, *Internataional Journal of Electrical, Computer, Energetic, Electronic and Communication Engineering*. 2(6), 1107–1117.
- [74] Yeo, T. L., Sun, T., & Grattan, K. T. V. (2008). Fibre-optic sensor technologies for humidity and moisture measurement. *Sensors and Actuators, A: Physical*, 144(2), 280–295.
- [75] Majumder, M., Gangopadhyay, T. K., Chakraborty, A. K., Dasgupta, K., & Bhattacharya, D. K. (2008). Fibre Bragg gratings in structural health monitoring-Present status and applications. *Sensors and Actuators, A: Physical*, 147(1), 150–164.
- [76] Jackson, D. A., & Jones, J. D. C. (1986). Extrinsic fibre-optic sensors for remote measurement: Part two. *Optics and Laser Technology*, 18(6), 299–307.
- [77] Ning, Y. N., Grattan, K. T. V, Wang, W. M., & Palmer, A. W. (1991). A Systematic Classification and Identification of Optical Fiber Sensors. *Sensor Actuator A Phys*, 29, 21–36.
- [78] Barrias, A., Casas, J. R., & Villalba, S. (2016). A Review of Distributed Optical Fiber Sensors for Civil Engineering Applications. *Sensors*, 16(748), 1–35.
- [79] Glisic, B., & Inaudi, D. (2012). Development of method for in-service crack detection based on distributed fiber optic sensors. *Structural Health Monitoring*, 11(2), 161–171.
- [80] Zinan Wang. (2015). Separation and Determination of the Disturbing Signals in Phase-Sensitive Optical Time Domain. *Journal of Lightwave Technology*, 33(15), 3156–3162.
- [81] Boyd, R. W. (2008). The Nonlinear Optical Susceptibility. *Nonlinear Optics (3rd Edition)*. Elsevier.
- [82] Lumens, P. G. E. (2014). Fibre-optic sensing for application in oil and gas wells.
- [83] Tsujikawa, K., Tajima, K., & Zhou, J. (2005). Intrinsic loss of optical fibers. *Optical Fiber*

References

Technology, 11(4), 319–331.

[84] Froggatt, M., & Moore, J. (1998). High-spatial-resolution distributed strain measurement in optical fiber with Rayleigh scatter. *Appl. Opt.*, 37(10), 1735–1740.

[85] Leung, C. K. Y., Wan, K. T., Inaudi, D., Bao, X., Habel, W., Zhou, Z., ... Imai, M. (2015). Review: optical fiber sensors for civil engineering applications. *Materials and Structures*, 48(4), 871–906.

[86] Hoult, N. a., Ekim, O., & Regier, R. (2014). Damage/Deterioration Detection for Steel Structures Using Distributed Fiber Optic Strain Sensors. *Journal of Engineering Mechanics*, 140 (1), 04014097.

[87] Marc Quiertant, , Florent Baby, , F., Aghiad Khadour, Paris, F., Pierre Marchand, , F., Philippe Rivillon, Jean-Claude Renaud, (2013). Deformation monitoring of reinforcement bars with a distributed fiber optic sensor for the shm of reinforced concrete structures, *Sustainable Growth*, 1063–1073.

[88] Henault, J. M., Quiertant, M., Delepine-Lesoille, S., Salin, J., Moreau, G., Taillade, F., & Benzarti, K. (2012). Quantitative strain measurement and crack detection in RC structures using a truly distributed fiber optic sensing system. *Construction and Building Materials*, 37, 916–923.

[89] Gifford, D. K., Kreger, S. T., Sang, A. K., Froggatt, M. E., Duncan, R. G., Wolfe, M. S., & Soller, B. J. (2007). Swept-wavelength interferometric interrogation of fiber Rayleigh scatter for distributed sensing applications. *Proc. SPIE*, 6770.

[90] Soller, B. J., Gifford, D. K., Wolfe, M. S., Froggatt, M. E., Yu, M. H., & Wysocki, P. F. (2006). Measurement of Localized Heating in Fiber Optic Components with Millimeter Spatial Resolution. In *Optical Fiber Communication Conference and Exposition and The National Fiber Optic Engineers Conference*, 03/05/2006 – 03/10/2006. Anaheim, CA, USA.

[91] Villalba, S., & Casas, J. R. (2013). Application of optical fiber distributed sensing to health monitoring of concrete structures. *Mechanical Systems and Signal Processing*, 39(1-2), 441–451.

[92] Regier, R., & Hoult, N. a. (2014). Distributed Strain Behavior of a Reinforced Concrete Bridge: Case Study. *Journal of Bridge Engineering*, 19(12), 05014007.

[93] Dan Frangopo and Yiannis Tsompankis. (2014). Maintenance and Safety of Aging Infrastructure: Structures and Infrastructures. *Vol. 10, ISBN: 9780415659420*.

[94] Bao, X., Zhang, C., Li, W., Eisa, M., El-Gamal, S., & Benmokrane, B. (2008). Monitoring the distributed impact wave on a concrete slab due to the traffic based on polarization dependence on stimulated Brillouin scattering. *Smart Materials and Structures*, 17(1), 15003.

[95] Zhou, D.-P., Qin, Z., Li, W., Chen, L., & Bao, X. (2012). Distributed vibration sensing with time-resolved optical frequency-domain reflectometry. *Opt. Express*, 20(12), 13138–13145.

[96] Lomonosov, A. M., Grigoriev, P. V, & Hess, P. (2009). Sizing of partially closed surface-breaking microcracks with broadband Rayleigh waves. *Journal of Applied Physics*, 108 (8) 1–8.

[97] Masoudi, A., Belal, M., & Newson, T. P. (2013). A distributed optical fibre dynamic strain sensor based on phase-OTDR. *Measurement Science and Technology*, 24(8), 85204.

References

- [98] Schlesinger, J., K. (2007). Optical Fibers Research Advances.
- [99] Dakin, J.P., Pratt, D.J., Bibby, G.W. (1985). Distributed anti- Stokes ratio thermometry, *Conference Papers - OFS*, 2–3.
- [100] Dakin, J.P., Pratt, D.J., Bibby, G.W. (2015). Distributed optical fiber Raman temperaturesensor using a semiconductor light source and detector, *Electronic Letters*, 100(3), 295–299.
- [101] Feced, R., Farhadiroushan, M., Handerek, V. a, & Rogers, A. J. (1997). A high spatial resolution distributed optical fiber sensor for high-temperature measurements. *Review of Scientific Instruments*, 68(10), 3772–3776.
- [102] Thorncraft, D. A., Scaets, M. G., Poole, S. B., Thomcraft, D. A., Sceats, M. G., & Poole, S. B. (1992). An Ultra High Resolution Distributed Temperature Sensor. *Optical Fiber Sensors Conference, 1992. 8th*, TH14.
- [103] Kurashima, T., Horiguchi, T., & Tateda, M. (1990). Distributed-temperature sensing using stimulated Brillouin scattering in optical silica fibers. *Opt. Lett.*, 15(18), 1038–1040.
- [104] Silixia: Commercial enterprise <https://silixa.com/>
- [105] Motil, A., Bergman, A., & Tur, M. (2016). State of the art of Brillouin fiber-optic distributed sensing. *Optics and Laser Technology*, 78, 81–103.
- [106] Shimizu, K., Horiguchi, T., Koyamada, Y., & Kurashima, T. (1994). Coherent Self-Heterodyne Brillouin OTDR for Measurement of Brillouin Frequency Shift Distribution in Optical Fibers. *Journal of Lightwave Technology*, 12(5), 730–736.
- [107] Bao, X., & Chen, L. (2012). Recent Progress in Distributed Fiber Optic Sensors. *Sensors*, 12(7), 8601.
- [108] Shi, B., Sui, H., Liu, J., & Zhang, D. (2006). The BOTDR-based distributed monitoring system for slope engineering. *Proceedings of 10th IAEG International Congress*, (683), 1–5.
- [109] Zhu, H.-H., Shi, B., Zhang, J., Yan, J.-F., & Zhang, C.-C. (2014). Distributed fiber optic monitoring and stability analysis of a model slope under surcharge loading. *Journal of Mountain Science*, 11(4), 979–989.
- [110] Glisic, B., & Yao, Y. (2012). Fiber optic method for health assessment of pipelines subjected to earthquake-induced ground movement. *Structural Health Monitoring-an International Journal*, 11(6), 696–711.
- [111] Matta, F., Bastianini, F., Galati, N., Casadei, P., & Nanni, A. (2008). Distributed Strain Measurement in Steel Bridge with Fiber Optic Sensors: Validation through Diagnostic Load Test. *Journal of Performance of Constructed Facilities*, 22(4), 264–273.
- [112] Thévenaz, L., Facchini, M., Fellay, A., Robert, P., Inaudi, D., & Dardel, B. (1999). Monitoring of large structure using distributed Brillouin fibre sensing. *International Conference on Optical Fiber Sensors*, 345–348.
- [113] Bernini, R., Minardo, A., & Zeni, L. (2009). Dynamic strain measurement in optical fibers by stimulated Brillouin scattering. *Opt. Lett.*, 34(17), 2613–2615.
- [114] Bucaro, J. A. (1979). Optical Fiber Acoustic Sensors. *Fiber Optics: Advances in Research and Development*, 33, 641–655.

References

- [115] Cole, J. H., Johnson, R. L., & Bhuta, P. G. (1977). Fiber-optic detection of sound. *America*, 90278, 1136–1138.
- [116] Pedrotti, F.L., Pedrotti, L.M., Pedrotti, L.S. (2007). Introduction to Optics. *Pearson International*. ISBN-10: 0131499335.
- [117] Rodríguez, L., Quintela, A., Cobo, A., & López-Higuera, J. M. (2010). Currents and Trends on Fiber Sensing Technologies for Structural Health Monitoring. *The 2nd Mediterranean Photonics Conference*, 29th November to 2nd December, Israel.
- [118] Cibula, E., & Donlagic, D. (2004). All-fiber Fabry-Perot strain sensor. *Proc. SPIE 5502*. Second European Workshop on Optical Fibre Sensors.
- [119] Islam, R., Ali, M., Lai, M., Lim, K., Ahmad, H. (2014). Chronology of Fabry-Perot Interferometer Fibre-Optic Sensors and Their Applications: A Review. *Sensors*. Vol(14), pages. 7451-7488.
- [120] Ran, Z., Rao, Y., Zhang, J., Liu, Z., & Xu, B. (2009). A Miniature Fiber-Optic Refractive-Index Sensor Based on Laser-Machined Fabry – Perot Interferometer Tip. *Journal of Lightwave Technology*, 27(23), 5426–5429.
- [121] Wan, X., & Taylor, H. F. (2002). Intrinsic fiber Fabry--Perot temperature sensor with fiber Bragg grating mirrors. *Opt. Lett.*, 27(16), 1388–1390.
- [122] Zhang, Y., Chen, X., Member, S., Wang, Y., Cooper, K. L., Wang, A., & Member, S. (2007). Microgap Multicavity Fabry – Pérot Biosensor. *Journal of Lightwave Technology*, 25(7), 1797–1804.
- [123] Zhao, J., Huang, X., He, W., & Chen, J. (2010). High-Resolution and Temperature-Insensitive Fiber Optic Refractive Index Sensor Based on Fresnel Reflection Modulated by Fabry – Perot Interference. *Journal of Lightwave Technology*, 28(19), 2799–2803.
- [124] Zhao, Y., & Ansari, F. (2001). Intrinsic Single-Mode Fiber-Optic Pressure Sensor. *IEEE Photonics Technology Letters*, 13(11), 1212–1214.
- [125] Wang, L., Fang, N., Wu, C., Qin, H., Huang, Z. (2014). A Fibre Optic PD Sensor Using Balanced Sagnac Interferometer and an EDFA-Based DOP Tunable Fibre Ring Laser. *Sensors*.
- [126] Grattan., K., T., V., Meggitt., B., T. (1988). Optical Fiber Sensor Technology: Fundamentals.
- [127] Hill, K. O. (1978). Photosensitivity in optical fibre waveguides: Application to reflection filter fabrication. *Applied Physics Letters*, 32, 647 - 657.
- [128] Meltz, G., Morey, W. W., & Glenn, W. H. (1989). Formation of Bragg gratings in optical fibers by a transverse holographic method. *Opt. Lett.*, 14(15), 823–825.
- [129] Campbell, R. (1993). Enhanced UV photosensitivity in boron codoped germanosilicate fibres. *Electronics Letters*, 29(1), 45–47(2).
- [130] Othonos, A., Kalli, K., Pureur, D., & Mugnier, A. (2006). Fibre Bragg Gratings. *Springer, Optical Sciences*, ISSN 3540317694.
- [131] P.J.Lemaire. (1993). High pressure H₂ loading as a technique for achieving ultrahigh UV photosensitivity and thermal sensitivity in GeO₂ doped optical fibres. *Electronics Letters*, 29(13), 1191–1193(2).

References

- [132] Malo, B., Hill, K., Bilodeau, F., Johnson, D. C., & Albert, J. (1993). Bilodeau, D. C., Point - by- Point fabrication of micro - Bragg gratings in photosensitive fibre using single excimer pulse refractive index modification techniques. *Electronics Letters*, 29(18), 1668–1669.
- [133] Hill, K., Bilodeau, F., Johnson, D. C., & Albert, J. (2001). Bragg gratings fabricated in monomode by UV exposure through a phase mask photosensitive optical fiber. *Applied Physics Letters*, 62, 1035–1038.
- [134] Mihailov, S. J., Smelser, C. W., Lu, P., Walker, R. B., Grobncic, D., Ding, H., Unruh, J. (2003). Fiber Bragg gratings made with a phase mask and 800-nm femtosecond radiation. *Opt. Lett.*, 28(12), 995–997.
- [135] Grobncic, D., Mihailov, S., Ramos, R., Grobncic, D., Mihailov, S. J., Smelser, C. W., & Ramos, R. T. (2008). Ultrafast IR Laser Writing of Strong Bragg Gratings Through the Coating of High Ge- Doped Optical Fibers Ultrafast IR Laser Writing of Strong Bragg Gratings Through the Coating of High Ge-Doped Optical Fibers, *IEEE Photonics Technology Letters*, 20 (12), 973 -975.
- [136] Grobncic, D., Mihailov, S. J., & Smelser, C. W. (2006). Femtosecond IR Laser Inscription of Bragg Gratings in Single- and Multimode Fluoride Fibers, *IEEE Sensors Journal*, 18(24), 2686–2688.
- [137] Wikszak, E., Thomas, J., Burghoff, J., Ortaç, B., Limpert, J., Nolte, S., Tünnermann, A. (2006). Erbium fiber laser based on intracore femtosecond-written fiber Bragg grating. *Opt. Lett.*, 31(16), 2390–2392.
- [138] Grobncic, D., Ding, H., Mihailov, S. J., & Smelser, C. W. (2005). Retro-reflective evanescent field sensors based on Bragg gratings made in biconical tapered fiber with femtosecond IR radiation. *Proc. SPIE* 5855.
- [139] Grobncic, D., Mihailov, S. J., Smelser, C. W., & Ding, H. (2004). Sapphire Fiber Bragg Grating Sensor Made Using Femtosecond Laser Radiation for Ultrahigh Temperature Applications, *IEEE Sensors Journal*, 16(11), 2505–2507.
- [140] Kelleher, P., & Nikogosyan, D. N. (2010). Optical Fiber Technology Inscription of narrow-band fibre Bragg gratings with 264 nm femtosecond pulses. *Optical Fiber Technology*, 16(4), 212–216.
- [141] Jensen, J. B., Plougmann, N., Deyerl, H.-J., Varming, P., Hübner, J., & Kristensen, M. (2002). Polarization control method for ultraviolet writing of advanced Bragg gratings. *Opt. Lett.*, 27(12), 1004–1006.
- [142] Ieuwland, R. E. N., Ylander, R. O. R., & Arlsson, P. E. R. K. (2016). NORIA : flexible automation in Fiber Bragg manufacturing. Available online (http://www.northlabphotonics.com/wp-content/uploads/2016/01/NORIA_white_paper_final-Feb2016.pdf)
- [143] Albert, J., Fokine, M., & Margulis, W. (2002). Grating formation in pure silica-core fibers. *Opt. Lett.*, 27(10), 809–811.
- [144] Xiong, L., Hofmann, P., Schülzgen, A., Peyghambarian, N., & Albert, J. (2014). Photosensitivity and thermal stability of UV-induced fiber Bragg gratings in phosphate glass fibers. *Opt. Mater. Express*, 4(7), 1427–1435.
- [145] Canning, J., Sceats, M. G., Inglis, H. G., & Hill, P. (1995). Transient and permanent

References

- gratings in phosphosilicate optical fibers produced by the flash condensation technique. *Opt. Lett.*, 20(21), 2189–2191.
- [146] Marshall, G., Ams, M., and M. J. W. (2006). Point by point femtosecond laser inscription of fibre and waveguide. *Proceeding of the 2nd Pacific International Conference on Application of Lasers and Optics*, 360–362.
- [147] Li, Y., Yang, M., Wang, D. N., Lu, J., Sun, T., & Grattan, K. T. V. (2009). Fiber Bragg gratings with enhanced thermal stability by residual stress relaxation. *Optical Letters* 17(22), 19785–19790.
- [148] Canning, J., Stevenson, M., Bandyopadhyay, S., & Cook, K. (2008). Extreme Silica Optical Fibre Gratings. *Sensors*, 8 (10), 6448–6452.
- [149] Warren – Smith, S., Nguyen, L., Lang, C., et al. (2016). Temperature sensing up to 1300 °C using suspended-core micro structured optical fibre. *Optics Express*, 24 (4), 3714 – 3719.
- [150] Mihailov, S. J. (2012). Fiber Bragg Grating Sensors for Harsh Environments. *Sensors*, 12(2), 1898–1918.
- [151] Kashyap, R. (2010). Chapter 10 - Principles of Optical Fiber Grating Sensors. *Fiber Bragg Gratings (Second Edition)*, 441–502.
- [152] Lam, D.K.V., Garside, B. K. (1981). Characterization of Single Mode Optical Fiber Filters. *Applied Optics*, 20 (3), 440 - 445.
- [153] Grattan, K. T. V, & Engineering, I. (n.d.). Optical Fibre Sensors and Measurement Systems, 0–5.
- [154] Carlos, L., Valente, G., Braga, A. M. B., Sant, A., Ribeiro, A., Regazzi, R. D., Willsch, R. (2003). Combined Time and Wavelength Multiplexing Technique of Optical Fiber Grating Sensor Arrays Using Commercial OTDR Equipment, *IEEE Sensors Journal*, 3(1), 31–35.
- [155] Childs, P. (2005). An FBG Sensing System Utilizing Both WDM and a Novel Harmonic Division Scheme, 23(1), 348–354.
- [156] Ou, Y. (2017). Large WDM FBG Sensor Network Based on Frequency Shifted Interferometry. *IEEE Photonics Technology Letters* 29(6), 535–538.
- [157] Chan, P., Jin, W., Demokan, S. (2000). Frequency division mltiplexing of FBG sensors Using FMCW approach. *Proceeding SPIE 4073*, 305.
- [158] Werzinger, S., Bergdolt, S., Engelbrecht, R., Thiel, T., & Schmauss, B. (2016). Quasi-Distributed Fiber Bragg Grating Sensing Using Stepped Incoherent Optical Frequency Domain Reflectometry. *Journal of Lightwave Technology*, 34(22), 5270–5277.
- [159] Chan, H. M., Parker, A. R., Piazza, A., & Richards, W. L. (2015). Fiber-Optic Sensing System : Overview , Development and Deployment in Flight at NASA, 2, 71–73.
- [160] Li, L., He, H., & Lin, Y. (2009). Study on The Spatial Division Multiplexing Technique of Fiber Bragg Grating Sensors. *Photonics and Optoelectronics*, 2 (3), 1–3.
- [161] Kerrouche, A., Boyle, W. J. O., Gebremichael, Y., Sun, T., Grattan, K. T. V, Täljsten, B., & Bennitz, A. (2008). Field tests of fibre Bragg grating sensors incorporated into CFRP for railway bridge strengthening condition monitoring. *Sensors and Actuators A: Physical*, 148(1), 68–74.

References

- [162] Rodrigues, C., Félix, C., Lage, A., & Figueiras, J. (2010). Development of a long-term monitoring system based on FBG sensors applied to concrete bridges. *Engineering Structures*, 32(8), 1993–2002.
- [163] Bosia, F., Giaccari, P., Botsis, J., & Varum, H. (2008). Weldable fibre Bragg grating sensors for steel bridge monitoring. *Measurement Science and Technology*, 19 (12).
- [164] Derkevorkian, A., & Masri, S. F. (2013). Strain-Based Deformation Shape-Estimation Algorithm for Control and Monitoring Applications. *AIAA Journal*, 51(9), 2231 - 2240.
- [165] Montanini, R., Recupero, A., De Domenico, F., Freni, Fabrizio. (2016). Strain Sharing Assessment in Woven Fiber Grating Sensors. *Sensors*, 16 (10), 1564.
- [166] Sevillano, E., Sun, R., Perera, R., Arteaga, A., Diego, A. De, & Cisneros, D. (2016). Comparison of PZT and FBG sensing technologies for debonding detection on reinforced concrete beams strengthened with external CFRP strips subjected to bending loads. *Materials and Construction*, 66(322), 75 - 88.
- [167] Sante, R. Di. (2015). Fibre Optic Sensors for Structural Health Monitoring of Aircraft Composite Structures: Recent Advances and Applications. *Sensors*, 15 (8), 18666–18713.
- [168] Wing, C. A. (2016). Large Scale Applications Using FBG Sensors : Determination of In-Flight Loads and Shape of a Composite Aircraft. *Aerospace*, 3 (3), 227 - 234.
- [169] Mao, J., Xu, F., Gao, Q., Liu, S., Jin, W., Xu, Y. (2016). Corrosion Cracking. *Sensors*, 16 (7), 1093.
- [170] Deng, F., Huang, Y., Azrami, F., Wang, Y. (2017). Metallic Coatings Using Fiber Bragg Grating Sensors. *Coatings*, 7 (3), 35.
- [171] Ren, L., Jiang, T., Li, H., & Yi, T. (2017). The study of pipeline corrosion monitoring using fiber optic sensing technique. *The 2016 Structures Congress*.
- [172] Tan, C. H., Shee, Y. G., Yap, B. K., & Adikan, F. R. M. (2016). Sensors and Actuators A : Physical Fiber Bragg grating based sensing system : Early corrosion detection for structural health monitoring. *Sensors & Actuators: A. Physical*, 246, 123–128.
- [173] Li, W., Xu, C., Chun, S., Ho, M., Wang, B., & Song, G. (2017). Monitoring Concrete Deterioration Due to Emission and FBG Strain Measurements. *Sensors*, 17 (3), 1–12.
- [174] Zhao, X., Gong, P., Qiao, G., Lu, J., Lv, X., & Ou, J. (2011). Brillouin Corrosion Expansion Sensors for Steel Reinforced Concrete Structures Using a Fiber Optic Coil Winding Method. *Sensors*, 11(11), 10798–10819.
- [175] Mao, J., Chen, J., Cui, L., Jin, W., Xu, C., & He, Y. (2015). Monitoring the Corrosion Process of Reinforced Concrete Using BOTDA and FBG Sensors. *Sensors*, 15(4), 8866–8883.
- [176] McCague, C., Fabian, M., Karimi, M., Bravo, M., Jaroszewicz, L. R., Mergo, P. Grattan, K. T. V. (2014). Novel sensor design using photonic crystal fibres for monitoring the onset of corrosion in reinforced concrete structures. *Journal of Lightwave Technology*, 32, 891–896.
- [178] Qiao, X., Shao, Z., Bao, W., & Rong, Q. (2017). Fiber Bragg Grating Sensors for the Oil Industry. *Sensors*, 17 (429).
- [179] Mao, J., Chen, J., Cui, L., Jin, W., Xu, C., & He, Y. (2015b). Monitoring the Corrosion Process of Reinforced Concrete Using BOTDA and FBG Sensors. *Sensors*, 18 (4), 8866–8883.

References

- [180] Feng, D., Qiao, X., Yang, H., & Rong, Q. (2015). A Fiber Bragg Grating Accelerometer Based on a Hybridization of Cantilever Beam, *IEEE Sensors Journal*, 15(3), 1532–1537.
- [181] Liu, Q., Qiao, X., Jia, Z., Fu, H., Gao, H., & Yu, D. (2014). Large Frequency Range and High Sensitivity Fiber Bragg Grating Accelerometer Based on Double Diaphragms. *IEEE Sensors Journal*, 14(5), 1499–1504.
- [182] Zhang, Y., Qiao, X., Liu, Q., Yu, D., Gao, H., Shao, M., & Wang, X. (2015). Optical Fiber Technology Study on a fiber Bragg grating accelerometer based on compliant cylinder. *Optical Fiber Technology*, 26, 229–233.
- [183] Guo, J., Xue, S., Zhao, Q., & Yang, C. (2014). Ultrasonic imaging of seismic physical models using a phase-shifted fiber Bragg grating, *Optics Express*, 22(16), 2942–2944.
- [184] Tsuda, H., Kumakura, K., & Ogihara, S. (2010). Ultrasonic sensitivity of strain-insensitive fiber Bragg grating sensors and evaluation of ultrasound-induced strain. *Sensors*, 10(12), 11248–11258.
- [185] Wee, J., Hackney, D., Bradford, P., & Peters, K. (2017). Mechanisms of signal coupling to optical fiber for FBG sensor detection of Lamb waves. *Proceeding of SPIE 10323*, 1–4.
- [186] Tsuda, H., Lee, J.-R., Guan, Y., & Takatsubo, J. (2007). Investigation of fatigue crack in stainless steel using a mobile fiber Bragg grating ultrasonic sensor. *Optical Fiber Technology*, 13(3), 209–214.
- [187] Moccia, M., Pisco, M., Cutolo, A., Galdi, V., Bevilacqua, P., & Cusano, A. (2011). Opto-acoustic behavior of coated fiber Bragg gratings. *Optics Express*, 19(20), 581–585.
- [188] Takeda, N., Okabe, Y., Kuwahara, J., Kojima, S., & Ogisu, T. (2005). Development of smart composite structures with small-diameter fiber Bragg grating sensors for damage detection: Quantitative evaluation of delamination length in CFRP laminates using Lamb wave sensing. *Composites Science and Technology*, 65(15-16 SPEC. ISS.), 2575–2587.
- [189] Xia, M., Jiang, M., Sui, Q., & Jia, L. (2015). Optik Theoretical and experimental analysis of interaction from acoustic emission on fiber Bragg grating. *Optik - International Journal for Light and Electron Optics*, 126(11-12), 1150–1155.
- [190] Lin, B., Bao, J., Yu, L., & Giurgiutiu, V. (2016). Acoustic emission detection with fiber optical sensors for dry cask storage health monitoring. *Proceeding of SPIE 9803*.
- [191] Yu, F., Okabe, Y., Wu, Q., & Shigeta, N. (2016). Fiber-optic sensor-based remote acoustic emission measurement of composites. *Smart Materials and Structures*, 25(10), 105033.
- [192] Wild, G., & Hinckley, S. (2010). Optical Fibre Bragg Gratings for Acoustic Sensors. *Proceedings of 20th International Congress on Acoustics, ICA*.
- [193] Cusano, A., Cutolo, A., Nasser, J., Giordano, M., & Calabrò, A. (2004). Dynamic strain measurements by fibre Bragg grating sensor, *Sensors and Actuators A: Physical*, 110 (1-3), 276–281.
- [194] Perez, I. M., Cui, H., & Udd, E. (2001). Acoustic Emission Detection Using Fiber Bragg Gratings. *Proceeding of SPIE 4328*, 209–215.
- [195] Ambrosino, C., Diodati, G., Laudati, A., Breglio, G., Giordano, M., Cutolo, A., & Cusano, A. (2008). Fiber Bragg Grating Sensors and Piezoelectric Actuators in Co-Located

References

- Configuration for Active Vibration Control Applications. *Smart Sensors and Sensing Technology* (pp. 167–181).
- [196] Webb, D. J., Surowiec, J., Sweeney, M., Jackson, D. A., Gavrilov, L. R., Hand, J. W., Bennion, I. (1996). Miniature fiber optic ultrasonic probe. *Proc. SPIE*.
- [197] Takahashi, N., Hirose, A., & Takahashi, S. (1997). Underwater Acoustic Sensor with Fiber Bragg Grating. *Optical Review*, 4(6), 691–694.
- [198] Carlton, J. (2012). Marine Propellers and Propulsion. *Technology and Engineering*.
- [199] Tobias, A. (1976). Acoustic-emission source location in two dimensions by an array of three sensors. *Non-destructive testing*.
- [200] Beagles, A., Fletcher, D., Peffers, M., Mak, P., Lowe, Caroline. (2016). Validation of a new model for railway overhead line dynamics. *Proceedings of the Institution of Civil Engineers Transport*, 169 (5), 339-349.
- [201] Yang, H. J., Chen, G. X., Zhang, S. D., & Zhang, W. H. (2012). Effect of the vibration on friction and wear behavior between the carbon strip and copper contact wire pair. *Journal of Engineering Tribology*, 226 (8), 1–7.
- [202] Midya, S., Member, S., Bormann, D., & Schütte, T. (2009). Pantograph Arcing in Electrified Railways — Mechanism and Influence of Various Parameters — Part II : With AC Traction Power Supply, 24(4), 1940–1950.
- [203] Ding, T., Chen, G.X., Li, Y., He, Qiu., Xuan, Wen. (2012). Friction and Wear Behavior of Pantograph Strips Sliding Against Copper Contact Wire with Electric Current. *AASRI Procedia*, 2, 288–292.
- [204] Liu, Z. (2015). Numerical study on multi-pantograph railway operation at high speed.
- [205] Ikeda, M. (2014). Measurement of the Contact Force of the Pantograph by Image Processing technology. *QR of RTRI*, 55 (2).
- [206] Doyle, S., Bastucescu, C., Vale, T. (2016). Pantograph Condition Monitoring System for Automated Maintenance Inspections and Prevention of Overhead Wiring Team Downs. *Inspection and Condition Monitoring Systems. Conference of Railway Excellence, Australia 2016*.
- [207] Comolli, L., Bucca, G., Boccione, M., Collina, A., Engineering, M., Milano, P., & Masa, V. La. (2010). First results from in-line strain measurements with FBG sensors on the pantograph collector of underground trains, 7726, 1–9.
- [208] Schröder, K., Ecke, W., Kautz, M., Willett, S., Tchertoriski, A., & Ag, B. L. S. (2007). Fiber optical sensor network embedded in a current collector for defect monitoring on railway catenary, 6585, 1–8.
- [209] Wagner, R., Maicz, D., Viel, W., Saliger, F., Saliger, C., Horak, R., & Noack, T. (2014). A fibre optic sensor instrumented pantograph as part of a continuous structural health monitoring system for railway overhead lines. *Inria*, 17 (6) 151–158.
- [210] Schröder, K., Rothhardt, M., Ecke, W., Richter, U., Sonntag, A., & Technology, P. (2017). Fibre optic sensing system for monitoring of current collectors and overhead contact lines of railways. *Journal of Sensors and Systems*, 6, 77–85.
- [211] Boffi, P., Bratovich, R., Persia, F., Barberis, A., Martinelli, M., Basso, A., Boccione,

References

M. (2006). Fiber Sensor for Collector Strain Monitoring in the Pantograph-Catenary Interaction. *Optical Fiber Sensors*, TuE45.

[212] Patent application: Optical Monitoring System. Applicant: City, University of London. Application number: GB1700573.7

List of publications by the author

Patent:

1. GB1700573.7 - Optical Monitoring System (2017).

Journal papers:

1. **Vidakovic Miodrag**, McCague Colum, Armakolas Ioannis, Sun Tong, Carlton Stephen John, Grattan K. T. Kenneth, “Fibre Bragg Grating-Based Cascaded Acoustic Sensors for Potential Marine Structural Condition Monitoring”, *Journal of Lightwave Technology*, Vol. 34, Issue 19 (2016), 4473 – 4478.
2. **Vidakovic Miodrag**, Armakolas Ioannis, Sun Tong, Carlton Stephen John, Grattan T. V. Kenneth, “Fibre Bragg Grating-Based Sensors Array for Improved Condition Monitoring of Marine Lifting Surfaces”, *Journal of Lightwave Technology*, Vol. 34, Issue 18 (2016), 4336 – 4342.
3. Armakolas Ioannis, Carlton John, **Vidakovic Miodrag**, Sun Tong, Grattan T. V. Kenneth, “The acoustic signatures of cavitation erosion on grade DH36 steel”, *Journal of Physics: Conference Series*, Vol. 656, 012109 (2015)

Conferences:

1. Chen Ye, **Vidakovic Miodrag**, Fabian Matthias, Swift Martin, Brun Lee, Sun Tong, Grattan T.V. Kenneth, “A temperature compensated fibre Bragg grating (FBG)-based sensor system for condition monitoring of electrified railway pantograph”, 25th International Conference on Optical Fibre Sensors, South Korea (2017). SPIE, Vol. 10323, 103236T.
2. Sun Tong, Fabian Matthias, Chen Ye, **Vidakovic Miodrag**, Javdani Saed, Grattan T. V. Kenneth, Carlton John, Gerada Chris, Brun Lee, “Optical fibre sensing: a solution for industry”, 25th International Conference on Optical Fibre Sensors, South Korea (2017). SPIE, Vol. 10323, 103231H.
3. Armakolas Ioannis, Carlton John, **Vidakovic Miodrag**, Sun Tong, Grattan T. V. Kenneth, “Cavitation erosion fracture mechanisms and their detection in ship operation”, 5th International Symposium on Marine Propulsion, SMP’17, Finland, 2017.

List of publications by the author

4. **Vidakovic Miodrag**, Armakolas Ioannis, Sun Tong, Carlton John, Grattan T. V. Kenneth, “Identification of cavitation signatures using both optical and PZT acoustic sensors”, 24th International Conference on Optical Fibre Sensors, Brazil (2015). SPIE, Vol. 9634, 963456.

5. **Vidakovic Miodrag**, McCague Colum, Meredith Phillip, Mitchell Tom, Brantut Nicolas, Sun Tong, Grattan T. V. Kenneth, “Development of High Sensitivity Acoustic Emission Sensors Based on Fibre Bragg Gratings for Structural Condition Monitoring, 3rd International Academic Conference for Graduates, NUAA, Nanjing, 2015.